

DOCTORAL THESIS

Pulsed Laser Deposition of Zn(O,Se) Layers for Optoelectronic Applications

Akram Abdalla Mohammed Ibrahim

TALLINN UNIVERSITY OF TECHNOLOGY
DOCTORAL THESIS
57/2021

Pulsed Laser Deposition of Zn(O,Se) Layers for Optoelectronic Applications

AKRAM ABDALLA MOHAMMED IBRAHIM



TALLINN UNIVERSITY OF TECHNOLOGY

School of Engineering

Department of Materials and Environmental Technology

This dissertation was accepted for the defence of the degree 03/11/2021

Supervisor:

Dr. Sergei Bereznev, Associate Professor
Department of Materials and Environmental Technology
Tallinn University of Technology
Tallinn, Estonia

Opponents:

Dr. Smagul Zh. Karazhanov, Senior Researcher
Department for Solar Energy
Institute for Energy Technology
Kjeller, Norway

Dr. Raivo Jaaniso, Associate Professor
Institute of Physics
University of Tartu
Tartu, Estonia

Defence of the thesis: 10/12/2021 at 13:00, Seminar room U06-442

Declaration:

Hereby I declare that this doctoral thesis, my original investigation and achievement, submitted for the doctoral degree at Tallinn University of Technology has not been submitted for doctoral or equivalent academic degree.

Akram Abdalla Mohammed Ibrahim

signature



European Union
European Regional
Development Fund



Investing
in your future

Copyright: Akram Abdalla Mohammed Ibrahim, 2021

ISSN 2585-6898 (publication)

ISBN 978-9949-83-759-5 (publication)

ISSN 2585-6901 (PDF)

ISBN 978-9949-83-760-1 (PDF)

Printed by Koopia Niini & Rauam

TALLINNA TEHNIKAÜLIKOOL
DOKTORITÖÖ
57/2021

Impulsslaser-sadestatud Zn(O,Se) kiled optoelektronseteks rakendusteks

AKRAM ABDALLA MOHAMMED IBRAHIM



Contents

List of Publications	7
Author's Contribution to the Publications	8
Introduction	9
Abbreviations and Symbols.....	11
1 Literature Review	13
1.1 Roles and Properties of the Buffer Layer in the TFSCs.....	13
1.2 Main Properties of Zn(O,Se).....	15
1.2.1 Zn(O,Se) Buffer Layer in TFSCs	16
1.3 Deposition Methods for Zn(O,Se) Layers	17
1.3.1 Molecular Beam Epitaxy	17
1.3.2 Radio Frequency Sputtering.....	17
1.3.3 Pulsed Laser Deposition	18
1.4 Principle and Development of PLD.....	19
1.4.1 PLD Setup	22
1.5 Summary of the Literature Review and Aims of the Study	22
2 Experimental Part.....	24
2.1 Deposition of Zn(O,Se) Layers	24
2.1.1 Preparation of the Substrates	24
2.1.2 Preparation of the PLD Targets	24
2.1.3 Zn(O,Se) Deposition	24
2.2 Fabrication of the Solar Cells	24
2.3 Characterization of Zn(O,Se) Layers and Solar Cells.....	25
3 Results and Discussion	26
3.1 Effect of the Substrate Temperature on the Properties of the Zn(O,Se) Layers.....	26
3.1.1 Structural, Morphological and Compositional Analysis	26
3.1.2 Optical Properties	32
3.1.3 Electrical Properties	33
3.2 Effect of the Laser Fluences on the Properties of the Zn(O,Se) Layers.....	35
3.2.1 Structural, Morphological and Compositional Analysis	35
3.2.2 Optical Properties	37
3.2.3 Electrical Properties	37
3.3 Application of Zn(O,Se) as a Buffer Layer with CIGSe Solar Cells.....	38
3.3.1 Optical and Elemental Analysis of Amorphous Zn(O,Se) Layers	38
3.3.2 XPS Depth Profile Analysis of the CIGSe/Zn(O,Se) Interface.....	39
3.3.3 HR-SEM Analysis of CIGSe/Zn(O,Se) Devices.....	40
3.3.4 Effect of the Zn(O,Se) Thickness on the Solar Cell Performance.....	40
Conclusions	45
References	46
Acknowledgments.....	56
Abstract.....	57
Lühikokkuvõte.....	59
Appendix 1	61

Appendix 2	89
Curriculum vitae.....	91
Elulookirjeldus.....	93

List of Publications

The list of author's publications, on the basis of which the thesis has been prepared:

- I **Akram Abdalla**, Sergei Bereznev, Nicolae Spalatu, Olga Volobujeva, Natalja Sleptsuk and Mati Danilson. Pulsed laser deposition of Zn(O,Se) layers in nitrogen background Pressure. *Scientific Reports*. 2019, 9: 17443.
- II **Akram Abdalla**, Erki Kärber, Valdek Mikli, Sergei Bereznev. The effect of laser fluences on the structural and optoelectronic properties of Zn(O,Se) films. *Materials Science in Semiconductor Processing*. 2021, 121, 105429.
- III **Akram Abdalla**, Mati Danilson, Souhaib Oueslati, Maris Pilvet and Sergei Bereznev. Amorphous Zn(O,Se) buffer layer for Cu(In,Ga)Se₂ thin film solar cells. *Materials Science in Semiconductor Processing*. 2021, 132, 105862.

Author's Contribution to the Publications

Contribution to the papers in this thesis are:

- I Planning and performing the experimental work and data processing, with a major role in manuscript writing.
- II Planning and performing the experimental work and data processing, with a major role in manuscript writing.
- III Planning of experimental work, deposition of Zn(O,Se) layers, processed all data with a major role in manuscript writing.

Introduction

The development of sustainable energy resources is vitally important to satisfy the high demand for energy due to the fast growth of the population, industrial revolution, etc. [1,2]. Currently, fossil fuels, i.e., coal, natural gas, and oil, are the source of more than 80% of the needed energy. However, these are limited resources of energy and are harmful to the environment and to humans [3]. On the other hand, hydropower, wind, biomass, geothermal, hydrogen, and solar energy are current and prospective renewable energy sources competing to substitute for fossil fuels and decrease CO₂ emissions. Among them, solar energy is one of the most promising renewable energy sources because the sun provides more energy to the earth in one hour than the entire world needs in one year [4]. Furthermore, energy from the sun can be generated either by converting the sun into electricity through the photovoltaic (PV) effect or direct collection in the form of heat (solar thermal technology). The compound annual growth rate (CAGR) of photovoltaics over the last 15 years was above 40%, which makes PVs one of the fastest growing industries at the present time [5]. Furthermore, thin film solar cells (TFSCs) are one of the most promising modules of PV technology, which will be discussed in detail below [6].

TFSCs are the second generation of solar cells, and they can be fabricated on both rigid and flexible substrates, such as glass, metals, plastics, etc. Also, it is possible to integrate TFSCs into the building component due to their relative lightweight and flexible structure. TFSCs consume an extremely low amount of materials compared to the 1st generation wafer-type solar cells based on crystalline silicon while converting a comparable amount of solar energy to electricity. The 2nd generation terrestrial PV panels that are commercially available include mainly amorphous silicon (a-Si), copper indium gallium chalcogenides Cu(In,Ga)Se₂ (CIGSe), Cu(In,Ga)S₂ (CIGS), and cadmium telluride CdTe. The raw materials used to fabricate amorphous silicon are the most earth-abundant and widely available; however, a-Si has some disadvantages, such as relatively rapid degradation and poor absorption capability [7]. Thus, p-type semiconductors with a high absorption coefficient and direct band gap (E_g), such as CIGSe, CdTe, and Cu₂ZnSnS₄ (CZTS), are promising alternative absorbers for a-Si in TFSCs due to the long-term stability and excellent optoelectronic properties. The complete structure of TFSCs may also include a thin layer of n-type semiconductor defined as a buffer layer (e.g., CdS, ZnS, In₂Se₃, etc.) with the functional role of improving the p-n junction of the TFSCs [8,9,10].

It is well known that a thin film CdS mainly prepared by chemical bath deposition (CBD) is the standard buffer layer used with CIGSe, CdTe, and CZTS solar cells [8,11–13]. In principle, CdS fulfills the main requirements of buffer layers; it forms a suitable conduction band alignment at the absorber/buffer interface. Also, the CdS buffer layer protects the absorber layers during the subsequent deposition [14–16]. However, recently, many efforts have been devoted to replacing the CdS with other materials due to some drawbacks, such as the predicted environmental hazards produced by the application of CBD–CdS in device production lines as reported here [8,17], the marketing problems of the devices containing Cd, which will result from the restriction of Cd in electronic devices as a legal policy of different states [18], the technological issues of using a non-vacuum CBD method to produce CdS while the rest of the production line uses vacuum techniques, and interfering light absorption with the absorbers in the wavelength range of 350–550 nm due to the relatively low band gap of CdS around 2.45 eV [8]. As a result, numerous materials have been examined as an alternative

Cd-free buffer layer, such as zinc and indium based materials [9,10,19–24]. Some of these materials have somewhat overcome the drawbacks of CdS. For example, a less-toxic Zn(O,S) was used as a buffer layer with Cu(In,Ga)(Se,S)₂ absorbers, which resulted in the highest recorded photoconversion efficiency (η) of 23.35% [25–30]. Also, the spectral response was enhanced in the blue region of the wavelength spectrum [24]. Herein, as a continuation in the same trend of replacing conventional CdS, we propose to apply Zn(O,Se) as an alternative buffer layer in TFSCs. Zn(O,Se) is a potential material for the replacement of the CdS buffer layer in solar cells and other optoelectronic devices because it possesses suitable electrical properties, optical transparency in the visible region, and consists of relatively eco-friendly elements [31].

The current thesis aimed to prepare and study Zn(O,Se) as a wide band gap, less-toxic alternative buffer layer for conventional CdS in optoelectronic devices. Thus, we deposited Zn(O,Se) layers onto soda-lime glass (SLG) substrates by pulsed laser deposition (PLD). Various deposition conditions were studied, such as the effect of the substrate temperature (T_s) (Paper I) and the effect of the laser fluences (Paper II) on the structural, optical, and electrical properties of the Zn(O,Se) layers. In addition, Zn(O,Se) has been applied as a buffer layer in complete solar cells with a CIGSe absorber, and the characteristics of the solar cells of these devices were investigated (Paper III).

This dissertation consists of the introduction part and three different chapters. Chapter 1 represents a literature review exploring the main requirements of the buffer layers, properties of the Zn(O,Se), different deposition methods for the Zn(O,Se) layers, and the principle, development history, and setup description of the PLD. Chapter 2 briefly explores the experimental techniques used to prepare and characterize the Zn(O,Se) layers and the complete solar cell structures fabricated in this thesis. Chapter 3 is separated into 3 different parts and represents the results and discussion about the effect of the T_s and the effect of the laser fluences on the properties of the Zn(O,Se) layers followed by the application of Zn(O,Se) as a buffer layer with a CIGSe absorber in complete solar cells.

Abbreviations and Symbols

a-Si	Amorphous Silicon
AZO	Aluminum doped Zinc Oxide
CBD	Chemical Bath Deposition
CBO	Conduction Band Offset
CW	Continuous Wave
DPSS	Diode-Pumping Solid-State
EDX	Energy Dispersive X-Ray Spectroscopy
E_g	Optical Band Gap
EQE	External Quantum Efficiency
FF	Fill Factor
FTO	Fluorine doped Tin Oxide
FWHM	Full Width at Half Maximum
HR-SEM	High-Resolution Scanning Electron Microscopy
IR	Infrared
ITO	Indium Tin Oxide
J_0	Saturation Current Density
J-V	Current density-Voltage
J_{sc}	Short Circuit Current Density
K.E	Kinetic Energy
LO	Longitudinal Optical
m-AP	Modified Auger Parameters
MBE	Molecular Beam Epitaxy
n	Ideality Factor
Nd:YAG	Neodymium: Yttrium Aluminum Garnet
PEC	Photoelectrochemical
PL	Photoluminescence
PLD	Pulsed Laser Deposition
PV	Photovoltaic
PVD	Physical Vapor Deposition
RBS	Rutherford Backscattering
RF	Radio Frequency
R_s	Series Resistance
R_{SH}	Shunt Resistance
RT	Room Temperature
sccm	Standard Cubic Centimeter
SLG	Soda-Lime Glass
TFSCs	Thin Film Solar Cells
T_s	Substrate Temperature
UV-Vis	Ultraviolet-Visible
V_o	Oxygen Vacancy

V_{oc}	Open Circuit Voltage
V_{Se}	Selenium Vacancy
V_{Zn}	Zinc Vacancy
XPS	X-Ray Photoelectron Spectroscopy
XRF	X-Ray Fluorescence
Yb:YAG	Ytterbium: Yttrium Aluminium Garnet
Zn(O,Se)	Zinc Oxyselenide
η	Photoconversion Efficiency
ΔG	Change in Gibbs Free Energy

1 Literature Review

1.1 Roles and Properties of the Buffer Layer in the TFSCs

Conventional TFSCs are multilayer structures consisting of a substrate (glass, metal, etc.), p-type absorber layer (CIGSe, CZTS, CdTe, etc.), n-type buffer layer (CdS, ZnMgO, In₂S₃, etc.), back contact (Mo, Ni, graphite, etc.), and transparent front contact (AZO, ITO, FTO, etc.). It can be fabricated in different configurations as a superstrate or substrate. Fig 1.1a shows the typical substrate configuration stack of the functional layers in a complete cell structure (substrate/back contact/absorber layer/buffer layer/front contact). The superstrate configuration stack (substrate/front contact/buffer layer/absorber layer/back contact) is represented in Fig 1.1b. In both configurations, the light comes from the front contact side [32,33]. The p–n junction occurs between the p-type absorber and the n-type buffer layer. The incident photons induce the formation of electron–hole pairs. The current is collected via electric contacts, and one of the contacts needs to be transparent to allow sunlight to be absorbed by the device [33,34].

The buffer layer is one of the important components of the TFSCs structure, which is placed between the absorber layer and front contact. Despite the fact that the p–n junction can be formed between the p-type absorber layer and front contact, the quality of the junction will be significantly improved by implementing an intermediate buffer layer. Buffer layers have several significant functions, such as providing optimal optoelectronic properties at the absorber/window layer interface and aiding in electron–hole separation, thus, decreasing the interfacial charge recombination [5]. Points to be considered when developing a buffer layer are: (i) be an n-type semiconductor; (ii) form a proper conduction band (E_{CB}) line–up between the window layer (*i*-ZnO) and the absorber layer; (iii) have low optical absorption in the visible range (i.e., relatively wide E_g); (iv) have a minimal defect density at the absorber/buffer interface; (v) have the Fermi level (E_F) positioned close to the absorber conduction band at the absorber/buffer interface (energetically shallow donor–type interface defects), i.e., complete inversion of

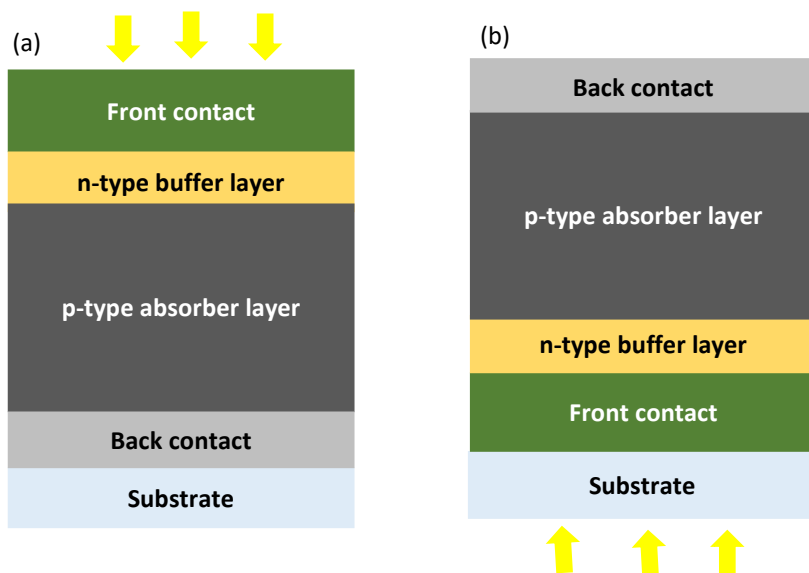


Figure 1.1. Schematic drawing of TFSCs structures designed in (a) substrate and (b) superstrate configurations. Yellow arrows indicate the illumination side [32].

the absorber surface [35,36]. Furthermore, other technological points to consider for developing the buffer layer at an industrial scale are: (i) technological applicability (proper large area deposition unit), (ii) production cost, and (iii) long-term stability and reproducibility.

The CBD–CdS fulfills the main parts of the abovementioned requirements, which made CdS the standard buffer layer in TFSCs [35]. Thus, the advantage of CdS over other materials is lattice matching with the absorber, as revealed in the literature [37]. In particular, for the chalcopyrite absorber, it was speculated that a combination of CBD–CdS forms valuable stable donor–type defects in Cu–deficient surfaces of the chalcopyrite absorber in a well–defined Fermi level position at the interface and a suitable concentration of Cd [35]. However, the real challenge in the development of an alternative buffer layer is establishing a similar effective defect chemistry as in the case of CdS, which will form a proper Fermi level position at the interface with the absorber and generate a suitable charge density [34]. The chalcopyrite absorber can be prepared as a copper–rich or copper–poor absorber [38]. Despite the high photoconversion efficiency that can be reached with CBD–CdS and the chalcopyrite absorber, many alternative buffer materials have been developed and investigated with chalcopyrite and other absorbers, such as indium and zinc based materials [26–31,39–43]. These buffers overcome the drawbacks of CBD–CdS in terms of toxicity, parasitic absorption in the short wavelength region, and deposition involving vacuum/dry techniques. The solar cell parameters of the chalcopyrite absorber with some of these buffer layers are compared with the standard CBD–CdS buffer layer in Table 1.1. Among these buffer layers, Zn(O,Se) has not been widely investigated as a buffer layer in TFSCs, and only one report is available on Zn(O,Se) prepared by sputtering with a very low photoconversion efficiency of the complete solar cells [44]. Therefore, the study of the Zn(O,Se) layers deposited by PLD with the application as a buffer layer in complete solar cell structures seems to be an innovative idea.

Table 1.1. Comparison of solar cell parameters of some alternative buffer layers with CBD–CdS buffer layer for CIGSe and ACIGSe absorbers.

Buffer layer	Absorber layer	V_{oc} (mV)	J_{sc} (mA/cm ²)	FF (%)	η (%)	Refs
Zn _{1-x} Mg _x O	CIGSe	693	35.90	72.00	17.90	41
Zn _{1-x} Sn _x O	CIGSe	689	35.07	75.30	18.20	39
Sn _{1-x} Ga _x O	ACIGSe	721	34.70	68.30	17.10	40
ZnSe _{1-x} O _x	ACIGSe	521	14.60	29.60	2.30	44
ZnSe _{1-x} O _x	CIGSe	482	2.20	26.20	0.30	44
ZnO _{1-x} S _x	CIGSSe	734	39.58	80.40	23.35	25–30
InO _{1-x} S _x	CIGSe	650	26.70	69.00	11.97	45,46
In ₂ S ₃	CIGSe	665	31.50	78.00	16.34	42
CdS	CIGSe	744	38.77	79.50	22.90	43,47–49

1.2 Main Properties of Zn(O,Se)

The ternary Zn(O,Se) alloy belongs to the group of II–VI semiconductors [31, 50]. The Zn(O,Se) layer can be used in the development of various applications, such as photoelectrochemical (PEC) water splitting [5,31,50] and photovoltaics [51]. Zn(O,Se) recently emerged as a promising material that can potentially replace the CdS buffer layer in solar cells due to its suitable electrical properties, wide tunable band gap, and low toxicity.

The ZnO_{1-x}Se_x layer was deposited with varying x values from 0 to 0.12 using the PLD technique [31,50]. The XRD pattern showed only the (002) diffraction peak, thus, suggesting that the ZnO_{1-x}Se_x layer was a single phase grown in the c-axis preferred orientation. This suggestion was further proven by a transmission electron microscopy investigation [31,50]. As the Se content increased, the (002) diffraction peak of the ZnO_{1-x}Se_x layer shifted progressively to lower 2θ values. This is in excellent agreement with the expansion of the lattice parameter due to incorporation of more selenium atoms in the oxygen sublattice. The substitutional Se (x) content in the layer and the lattice parameters of wurtzite ZnO (c = 0.52 nm) and ZnSe (c = 0.653 nm) were calculated using Vegard's law [31,50]. The (002) XRD diffraction peak of the ZnO_{1-x}Se_x layer corresponds to a Se content of 0–22%; this selenium content was measured by Rutherford backscattering (RBS) [31,50]. However, it was reported that only half of the RBS estimated selenium ratios were incorporated into the substitutional sites, which suggests that part of the selenium atoms precipitates in a small form and/or resides in the grain boundaries [31,50]. Also, the ZnO_{1-x}Se_x layers deposited at 300–550°C by PLD. The XRD pattern showed only the 001 diffraction peak, which reveals the growth of ZnO_{1-x}Se_x layers in the 0001 (c-plane) preferred direction. By increasing the T_s above 450°C, the ZnO_{1-x}Se_x peak separated into two peaks due to the phase separation to the ZnO_{1-x}Se_x phase and a small amount of the pure ZnO phase [52,53].

The optical properties of the ZnO_{1-x}Se_x layers with a thickness of ≥ 1 μm showed > 80% transparency of this alloy in the visible region of the spectrum. The Fermi level of the Zn(O,Se) layer was found to shift from 0.1 eV at the bottom of the conduction band edge (for carrier density = 10¹⁷ cm⁻³) to 0.5 eV above the conduction band edge (for carrier density = 3 × 10²⁰ cm⁻³) [54]. Also, the absorption edge of the Zn(O,Se) layer was redshifted relative to the ZnO layer with increasing Se content. This shift in the absorption edge shows the existence of the band gap bowing in the ZnO_{1-x}Se_x layer. Thus, the bowing parameters were found to be 7.0–12.7 eV [31,50,55,56]. This change in the band gap bowing parameters tunes the band gap of ZnO_{1-x}Se_x widely from 2.76 to 3.29 eV.

Furthermore, the Hall effect measurements showed n-type conductivity of the ZnO_{1-x}Se_x layers. The electron concentration of the Zn(O,Se) layers with an Se ratio of 6 at% varied from 1 × 10¹⁷ to 7 × 10¹⁹ cm⁻³, while the carrier mobility changed in the extremely narrow range from 13 to 20 cm²/Vs [31,50,51,57]. The resistivity of the ZnO_{1-x}Se_x layers was relatively constant at roughly 5.5 × 10⁻³ Ω·cm [51,57]. Thus, these flexible and tunable electrical and optical properties of Zn(O,Se) make it a suitable candidate as a buffer layer in TFSCs, in particular using PLD technique. To the best of our knowledge, there is no report exist for the fabrication of Zn(O,Se) buffer layers in TFSCs using PLD method.

1.2.1 Zn(O,Se) Buffer Layer in TFSCs

The $\text{ZnSe}_{1-x}\text{O}_x$ (ZnSe rich) with 1% oxygen incorporated was used as a buffer layer with CIGSe and Ag alloyed CIGSe (ACIGSe) solar cells [44]. In this study, the radio frequency (RF) magnetron reactive sputtering technique was applied to grow $\text{ZnSe}_{1-x}\text{O}_x$ layers onto the SLG/Mo/CIGSe substrate. Thus, ZnSe was applied as the cathode target. Oxygen and argon were selected as the sputtering working gases. The total gas flow was kept at 30 standard cubic centimeters (sccm). The O_2 content of the sputtering gas mixture ($[\text{O}\%] = [\text{O}_2]/[\text{O}_2]+[\text{Ar}]$) was varied to change the oxygen content of the $\text{ZnSe}_{1-x}\text{O}_x$ layers. A number of samples were sputtered as a function of varying oxygen content from 0% to 1.4% with a step size of 0.1% for a comprehensive investigation. The sputtering power density was 1.48 W/cm^2 , and the sputtering pressure was constant at 10 mTorr. No intentional substrate heating was used in this case. The $\text{ZnSe}_{1-x}\text{O}_x$ layers sputtered in a 1% oxygen gas mixture was selected for use as an alternate buffer layer with CIGSe solar cells, and the solar cell parameters were $V_{\text{OC}} = 482 \text{ mV}$, $J_{\text{SC}} = 2.20 \text{ mA/cm}^2$, $\text{FF} = 26.20\%$, and $\eta = 0.30\%$ as shown in Table 1.1 and Fig 1.2. The CIGSe/ $\text{ZnSe}_{1-x}\text{O}_x$ cells showed a very low device performance, which is attributed to the large spike barrier at the buffer/absorber interface that impedes the electron transport and collection. By integrating the O_2 into zinc selenide during the reactive sputtering in a 1% oxygen gas mixture, the band gap of the $\text{ZnSe}_{1-x}\text{O}_x$ layers was decreased due to the downward shift of the conduction band. Hence, the conduction band offset (CBO) between the $\text{ZnSe}_{1-x}\text{O}_x$ buffer layer and the CIGSe absorber was expected to decrease. However, this was not the case due to the difficulty in altering the zinc selenide band structure by the oxygen incorporation approach. When the CIGSe absorber was alloyed with Ag in a ratio of $[\text{Ag}]/[\text{Ag}]+[\text{Cu}] = 0.3$, this ratio widens the CIGSe absorber band gap by 0.1 eV [58]. Consequently, an interesting improved result was obtained as $V_{\text{OC}} = 521 \text{ mV}$, $J_{\text{SC}} = 14.60 \text{ mA/cm}^2$, $\text{FF} = 29.60\%$, and $\eta = 2.30\%$ [44]. Thus, these improved results were because of a better CBO alignment of the ACIGSe absorber and the $\text{ZnSe}_{1-x}\text{O}_x$ buffer [44].

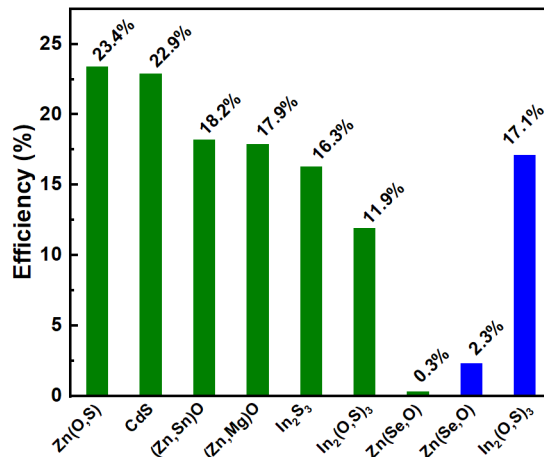


Figure 1.2. Efficiencies comparison of different Cd-free buffer layers produced by different methods with the best cell containing CBD-CdS for the CIGSe and ACIGSe (in blue color) based solar cells [25–30,39–43,47–49].

1.3 Deposition Methods for Zn(O,Se) Layers

The main reported deposition techniques available for the preparation of Zn(O,Se) layers are molecular beam epitaxy (MBE), radio frequency sputtering, and pulsed laser deposition. An overview of each deposition method will be discussed in the following sections.

1.3.1 Molecular Beam Epitaxy

MBE is a subclass of the physical vapor deposition (PVD) technique. It is an epitaxial technique to grow a thin film of single crystals. The MBE approach was developed by Alfred Y. Cho [54,59] and J. R. Arthur at Bell Telephone Laboratories in the late 1960s. MBE is commonly used for manufacturing semiconductor devices, including a transistors, quantum dots, semiconductor lasers, and also used to produce organic semiconductors. The process of MBE takes place in a high vacuum or ultra-high vacuum chamber (10^{-8} – 10^{-12} Torr). The target elements are heated or electron-beam evaporated until they begin to slowly sublime. Then, the gaseous elements condense on the wafer (substrate), where they may react with each other. The term "beam" means that vacuum chamber gases or evaporated atoms do not interact with each other until they reach the substrate because the atoms have long mean free paths. The advantages of the MBE technique are the growth of complex structures with the precise control of the alloy composition, thickness, and doping level. Furthermore, the MBE is highly clean and compatible with a wide range of in-situ analytical techniques [60]. The drawback is that assembling and operation are expensive.

As reported, ZnO_{1-x}Se_x layers were prepared by MBE at 250–350°C [55]. The elemental Zn (7N), Se (6N), and O₂ gas (6N) were used as source materials. The RF power of the oxygen radical source during growth was 300 W. The zinc flux was 1×10^{-6} Torr, and the flow rate of the oxygen was 0.3 sccm. The Se flux changed from 5×10^{-8} to 6×10^{-7} Torr to control the Se composition x from 0 to 0.01. The XRD result showed no phase splitting, and during the ZnO_{1-x}Se_x growth, the RHEED pattern was streaky, demonstrating a smooth ZnO_{1-x}Se_x surface and two-dimensional growth [35]. PL spectra of the ZnO_{1-x}Se_x showed donor bound exciton peaks for x less than 0.0006. The spectral structure was similar to ZnO, but the peak energies and PL intensity were dissimilar. The band edge emissions of the ZnO_{1-x}Se_x were redshifted from that of ZnO, demonstrating the existence of band gap bowing. The bowing parameter was 12.7 ± 1.6 eV. That reflects with a small change in the Se composition, the band gap of the ZnO_{1-x}Se_x will change remarkably, which will lead to a small lattice mismatch relative to ZnO [55]. Therefore, MBE is good for Zn(O,Se) deposition, but it is expensive in terms of operation and assembling.

1.3.2 Radio Frequency Sputtering

RF-sputtering is one of the PVD techniques used to deposit thin films. RF-sputtering is an appropriate technique for the fabrication of dielectric micro-cavities, and it is a versatile technique to prepare different layers with controlled refractive index and thicknesses [61]. Usually, in a sputtering system, the process takes place in a vacuum chamber when high energy ions (usually argon ions) from the plasma of a gaseous discharge bombard a target that is the cathode of the discharge. Target atoms are ejected and condense onto a substrate (the anode), forming the films [62]. The positive aspects of this technique are that the charge-up effects are avoided and arcing is decreased due to the use of an alternating current RF source of frequency, it is an

efficient technique because it can work at low pressures (1 to 15 mTorr) while maintaining a plasma, etc. [63]. However, the negative aspects are that: (i) most of the incident energy on the target becomes heat energy, (ii) it is hard to grow uniformly on complex structures, e.g., turbine blades, and (iii) it is difficult to produce high performance thick coatings due to higher internal residual stress levels [63].

RF-sputtering of $\text{ZnO}_{1-x}\text{Se}_x$ was performed using a sputter power of 300 W at 340°C and a ceramic ZnSe target with Ar and O_2 as working and reactive gases, respectively [56]. The Se content (x) was varied from 0 to 1. Raman measurements of $\text{ZnO}_{1-x}\text{Se}_x$ showed the frequencies of the longitudinal optical (LO) phonon modes of ZnO at 578 cm^{-1} and of ZnSe at 250 cm^{-1} [56]. A two-mode behavior of the LO phonon modes has been noticed in the Raman spectra of $\text{ZnO}_{1-x}\text{Se}_x$ when the Se content (x) changed from 0.06 to 0.94. In Se-rich samples, the ZnSe is dominated by a LO like mode, while in the O-rich samples, a ZnO like LO phonon is dominant. Samples with $x = 0.11$ and 0.08 exhibit broad bands in the vicinity of the LO phonons of the binary alloys. The redshift of the ZnO like LO phonon with decreasing Se content is less pronounced because no Zn(O,Se) samples exist so far with a reasonable concentration of oxygen and selenium. However, the two-mode behavior of the LO phonons of the $\text{ZnO}_{1-x}\text{Se}_x$ system is obviously noticeable. The results of the band gap value as a function of Se content indicate a sizeable downshift in energy, which represents a larger bowing. The bowing parameter is around 7.0 eV. Thus, $\text{ZnO}_{1-x}\text{Se}_x$ layers could be deposited only in a narrow composition range close to the binary constituents of ZnO and ZnSe due to the limited solubility of Se and O in ZnO and ZnSe, respectively [56].

1.3.3 Pulsed Laser Deposition

PLD is a subclass of PVD techniques and is commonly used to deposit complex-oxide heterostructures, super-lattices, and well-controlled interfaces [52]. PLD is one of the most promising methods for the stoichiometric deposition of high quality, uniform, and adherent layers [52]. Usually, the PLD process is performed in a high or ultra-high vacuum chamber, and a high-power pulsed laser beam is focused onto the target surface of the material that is to be deposited. Thus, the material is vaporized and forms a plasma plume that expands and condenses onto a substrate surface. The PLD technique was used to deposit the $\text{ZnO}_{1-x}\text{Se}_x$ layer as a function of substrate temperature and selenium-to-oxygen ratio [31,50,51,53,57]. Thus, the results of these studies are discussed in detail below.

Firstly, Mayer et al. [31,50] deposited a $\text{ZnO}_{1-x}\text{Se}_x$ layer by PLD at $200\text{--}500^\circ\text{C}$ using a ZnO/ZnSe premixed pressed powder target, and x ratios ranged from 0 to 0.12. The laser beam generated from a KrF excimer laser ($\lambda = 248\text{ nm}$) had a laser energy ranging from 88 to 280 mJ, a laser spot size of approximately 1 mm^2 , and a pulse frequency of 5 Hz. The pressure inside the vacuum chamber ranged from 10^{-3} Torr to 10^{-6} Torr [31]. The obtained $\text{ZnO}_{1-x}\text{Se}_x$ film was a single phase with the c -axis (002) preferred orientation, and the (002) diffraction peak of $\text{ZnO}_{1-x}\text{Se}_x$ steadily shifted to lower 2θ as the Se content increased. In addition, at $x > 0$, a steady increase in the absorption coefficient was observed, which started at a much lower energy of roughly 2 eV. Thus, this shift in the onset and shape of the absorption edge reflects the complex nature of the band edges of the $\text{ZnO}_{1-x}\text{Se}_x$ alloy [31,50]. The electron concentration ranged from $1 \times 10^{17}\text{ cm}^{-3}$ to $5 \times 10^{19}\text{ cm}^{-3}$ as a function of Se content [31,50]. Furthermore, the flat band potential decreased by roughly 0.1 V when ZnSe and ZnO are alloyed. However, when the $\text{ZnO}_{1-x}\text{Se}_x$ layer was grown on the top of the Si solar cell, the flat band potential was significantly shifted down by 0.5 V. Also, these layers were used as a working electrode

in PEC water splitting under white light irradiation of 2 suns. Thus, the $\text{ZnO}_{1-x}\text{Se}_x$ alloy shifted the onset to a lower potential due to its band gap reduction. However, the $\text{ZnO}_{1-x}\text{Se}_x/\text{Si}$ produced an enhanced photocurrent and shifted the reaction onset to a lower voltage [50].

Secondly, the same group in other studies [53,51,57] grew a $\text{ZnO}_{1-x}\text{Se}_x$ layer by PLD at 300–550°C using a 92 at% ZnO and 8 at% ZnSe premixed pressed powder target onto a polished c-plane sapphire substrate. The laser beam generated from a KrF excimer laser ($\lambda = 248 \text{ nm}$) had a laser fluence of 4.4 J cm^{-2} , a laser spot size of approximately 0.03 cm^2 , and a pulse frequency of 5 Hz. The pressure inside the vacuum chamber was $6.2 \times 10^{-6} \text{ Torr}$ [51,57]. The change in T_s at a constant laser fluence of 4.4 J cm^{-2} affects the structure and chemistry of the deposited $\text{ZnO}_{1-x}\text{Se}_x$ layer in three aspects: phase homogeneity, composition (x), and crystallinity. The XRD pattern showed only the 001 diffraction peak for all $\text{ZnO}_{1-x}\text{Se}_x$ layers, which reveals the growth of the $\text{ZnO}_{1-x}\text{Se}_x$ layers in the 0001 (c-plane) preferred direction. Moreover, as T_s increased, the crystallinity of the $\text{ZnO}_{1-x}\text{Se}_x$ layer increased, but the Se content decreased. Furthermore, with increasing T_s above 450°C, the $\text{ZnO}_{1-x}\text{Se}_x$ peak separated into two peaks due to the phase separation. Thus, as T_s increased, more energy exists for atom migration, and as a result, the layers dissociated to the $\text{ZnO}_{1-x}\text{Se}_x$ phase and a small quantity of the ZnO pure phase. Furthermore, no ZnSe phase was formed. At 400°C or below, the $\text{ZnO}_{1-x}\text{Se}_x$ transferred stoichiometrically from the target to the substrate. However, with increasing T_s , the content of Se incorporated into the ZnO matrix decreased. Thus, this may be because the Se is easily desorbed during deposition at higher T_s , as it has a high vapor pressure. In the $\text{ZnO}_{1-x}\text{Se}_x$ layers, the optical absorption takes place due to the transition from the Se-derived band to the conduction band edge [51,57]. Hence, for the layers deposited at 300–400°C, the absorption edge was constant at a low energy of 2.2 eV due to a relatively stable Se content. However, as T_s increased above 400°C, the absorption edge shifted to higher energy. For the electrical properties, the resistivity was relatively constant at roughly $5.5 \times 10^{-3} \Omega\text{-cm}$ for the $\text{ZnO}_{1-x}\text{Se}_x$ layer grown at 300–400°C. However, a significant increase in the resistivity occurred for layers grown above 400°C due to the phase inhomogeneities. The T_s value had an insignificant effect on the carrier mobility and concentration, i.e., the mobilities changed from 13 to 20 cm^2/Vs , while the concentrations varied in the extremely narrow range from 6×10^{19} to $7 \times 10^{19} \text{ cm}^{-3}$ [51,57].

1.4 Principle and Development of PLD

As early as 1965 [64], the application of pulsed lasers to ablate a solid target with the stoichiometric transfer of a material to the substrate was reported in the literature. This was similar to the earlier flash evaporation technique where the dielectrics and semiconductors films were grown using a ruby laser. Thus, BaTiO_3 and SrTiO_3 films were grown by pulsed laser evaporation from their powders in 1969 [65]. Stoichiometric intermetallic materials such as low critical temperature (low- T_c) superconducting films of ReBe_{22} and Ni_3Mn were grown by a pulsed laser beam in 1975 [66]. For the first time, Zaitsev–Zotov and co-workers demonstrated the superconductivity in pulsed laser evaporated $\text{BaPb}_{1-x}\text{Bi}_x\text{O}_3$ films followed by heat treatment in 1983 [67]. The successful application of the in-situ growth of the epitaxial high-temperature superconductor films at Bell Communications Research in 1987 was the real breakthrough of the PLD [68]. Since then, PLD has been frequently applied to grow complex oxides and those high-temperature superconductors, including materials that are not possible to prepare via an equilibrium route.

Lasers used in PLD are classified as gas lasers, solid–state lasers (e.g., ruby laser), fiber lasers, semiconductor lasers, and liquid lasers depending on their media as well as their nominal characteristics and parameters, as presented in Table 1.2 [69]. Some of these lasers will be discussed here in detail. The gas lasers generate coherent irradiation by applying a voltage across a ceramic or a glass tube that is filled with the gain medium (gas mixture or low–pressure gas). The voltage creates an electric field within the tube, which produces an electrical current. These electrons react with the gas atoms, thereby migrating them to top energy states that will be the upper laser state [69]. The upper laser level declines naturally and very slowly to the ground state compared to the lower laser level, thus forming a population inversion among both laser levels.

As several gaseous media are available, the working wavelength ranges differ from the visible range for argon ion and HeNe lasers, mid IR range for CO₂ lasers, and UV range for excimer lasers [69]. Gas lasers have a different usage such as in diode–pumped solid–state (DPSS) lasers, laser processing, medical eye surgery, and laser diodes. The excimer laser is an ultraviolet laser based on compounds of halogens (F, Cl), noble gases (Kr, Xe) as its laser medium, such as KrF, XeF, XeCl, etc. [70]. The UV–excimer laser has characteristics of generating sufficient active oxygen for in-situ growth, oscillating at a remarkably high efficiency for lasers in the UV range, and allowing relatively compact hardware and very uniform cross–section of the beam, in other words, a uniform energy distribution [70,71]. The excimer lasers are used in different fields, such as surface reforming of resins like Teflon, etc., labeling materials that cannot be labeled by CO₂ lasers or YAG lasers, semiconductor lithography (e.g., light source) manufactured by Gigaphoton, aberration processing of macromolecular films, in medicine (vision correction surgery such as laser assisted in situ keratomileusis), and in PLD. They are also used in fields of scientific research, both as primary sources and, particularly the XeCl laser, as pump sources for tunable dye lasers [71,72,73,74].

Solid–state lasers are defined as a laser in which its gain medium contains an active ion species implanted as impurities in the host material (glass or crystal), which is optically transparent. Solid–state lasers attain their population inversion via optical pumping, which can be achieved by a flashlamp or direct pumping from another laser source like a DPSS system or a laser diode [69]. The host material for a solid–state gain medium must have both unique suitable macroscopic mechanical, optical, and thermal properties and microscopic lattice properties. The host material can be a ceramic, glass, crystal, and organic matter, but crystals and glasses are the most common among others [69]. Examples of the most popular solid–state lasers are Nd:YAG and Yb:YAG. The Nd:YAG laser with a wavelength of 1060 nm can be used to deposit layers using the second harmonic at 532 nm or the third harmonic at 355 nm. The Nd:YAG laser as a solid–state type has some operational advantages over the UV–excimers type: it is safer and easier to handle because it does not involve highly hazardous gases [70]. However, it has a non–uniform cross–section of beam energy distribution and a significant decreased energy at the third harmonic (UV range).

Table 1.2. Characteristics and parameters of the common lasers.

Laser types	Lasers	Wavelength (nm)	CW/pulsed
Gas (UV–excimer)	ArF, KrF, XeF, XeCl	193, 248, 353, 308	ns range
Gas (mid IR range)	CO ₂	10600	CW/ μ s range
Solid–state	Yb:YAG, Nd:YAG	1030, 1060	CW/ps range
Fiber	Yd:glass, ND:glass	1030, 1060	CW/fs range

A fiber laser is referred to as a laser where the optical fiber is itself the gain medium, which is possible to be distinguished from having another type of laser or gain medium simply being integrated to an optical fiber [69]. Hence, a fiber laser is formed when a solid-state gain medium is fabricated into an optical fiber and a resonator is integrated. Glass is a host material, and the laser active ions are classically doped into the core of the optical fiber. The most popular fiber lasers are Yd:glass and Nd:glass. Fiber lasers can work in either CW or pulsed mode, and it is possible for them to function over much of the near IR and mid IR spectral region. They can form high quality output beams and can attain high output powers. Thus, these properties allow fiber lasers to be used for different purposes, such as laser surgery, seeding of other more powerful lasers, optical fiber communications, and range-finding [69].

The growth process of the materials from the plasma plume in PLD is different than the growth process in thermal evaporation [75]. In the PLD technique, the excimer laser beams ablate materials rapidly from a solid target to form a high energy plasma plume, which then condenses onto a substrate. The deposition process of the PLD can be explained by four steps [76]:

- Target ablation leading to plasma plume formation.
- Expansion of the plasma and the possible reactions in the plasma.
- Deposition of the ablated materials on the substrate.
- Film growth on the substrate surface.

In the laser ablation process, first, the photons are transferred into electronic excitations. Thus, if the strength of the electric field of an electromagnetic wave is higher than the threshold value of the material, dielectric breakdown will take place via electron excitation above the work function level, leading to a pure ablation process [77]. As ablation occurs, the plasma plume starts to expand into the vacuum and the angular distribution will follow a cosine power law, as indicated in equation (1.1) [78]. In the multicomponent target, various elements may have various angular dependencies [76,79]. After the laser beam has been extinguished and no new particles are emitted from the target, the expansion process is adiabatic. When the volume of the plume increases, the temperature of the plasma is reduced, and the thermal energy is converted into kinetic energy of the particles. During the expansion process, particles collide with each other, and multiple collisions of the particles in the plasma plume dissipate the kinetic energy of the particles. The ablated particles reach the substrate and start to nucleate and condensate on the substrate surface when the kinetic energy of the particles slow down sufficiently [80]. However, desorption of the particles and surface diffusion may take place, but in most cases, strong adhesion is established. Different mechanisms can be involved in the film growth, such as Frank-van der Merwe type monolayer growth, Stranski-Krastanov type monolayer growth followed by island formation, or Volmer-Weber type nucleation and island formation.

$$t(\beta) = t_{max} \cos^{p+3}(\beta) \quad (1.1)$$

where t is the film thickness, β is the angle measured from the target surface normal measured at the center of the laser spot, p is an integer, and t_{max} is the maximum film thickness.

PLD has developed significantly with time, and the deposition process stands on those four basic steps. PLD is used mainly to deposit complex oxides that are difficult to obtain via the equilibrium route with stoichiometric transfer of the materials, i.e., this method seems to be suitable for Zn(O,Se) layer deposition.

1.4.1 PLD Setup

The PLD setup contains the laser, the deposition chamber, vacuum pumps, necessary optics, the substrate, and target holders [81]. The target and substrate are placed in the same line but separated by a distance of centimeters, as illustrated in Fig 1.3 [82], and the chamber is evacuated into a high vacuum. Afterward, the chamber can be filled with either an inert or reactive background gas. The laser beam is focused onto the surface of the target, and the short high energy pulses will evaporate and ionize materials from the target and form a plasma plume. The formed plasma plume expands and reaches the substrate with enough kinetic energy for strong adhesion of the growing films [80].

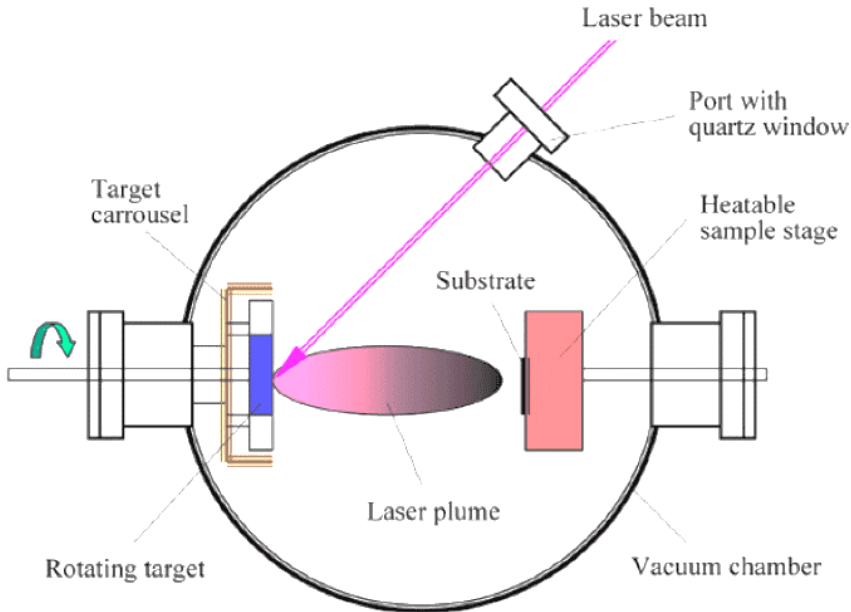


Figure 1.3. Schematic illustration of the pulsed laser deposition chamber [82].

1.5 Summary of the Literature Review and Aims of the Study

The studies reported in the literature on the properties of Zn(O,Se) layers, different preparation methods, and principle of the PLD can be summarized as follows:

- Zn(O,Se) is a promising group II–VI semiconductor in the field of materials science and technology due to its appropriate properties, such as tunable wide band gap, low toxicity, and suitable electrical properties.
- A two mode behavior of the $\text{ZnO}_{1-x}\text{Se}_x$ layer with a small change in Se content indicates the limited solubility of Se in ZnO and O in ZnSe, which means the limitations of ternary Zn(O,Se) formation. Thus, a careful investigation is required to set the optimal Se/O ratios for the specific application and to optimize other deposition parameters.
- A significant redshift in the onset and shape of the absorption edges of $\text{ZnO}_{1-x}\text{Se}_x$ layers with increasing Se content indicates the complex nature of the absorption edges, which result in the band gap bowing. The bowing parameters are approximately in the range of 7.0–12.7 eV. A further systematic study including computational methods is required for a better understanding of the structural and optoelectronic properties of the Zn(O,Se) layer.

- All reported preparation methods for the Zn(O,Se) layer are subclasses of physical vapor deposition techniques, including PLD, MBE, and RF-sputtering. Among them, PLD is one of the most promising techniques to deposit complex-oxide heterostructures, super-lattices, and well-controlled interfaces in high quality, uniform, well-adherent layers to the substrate and stoichiometric transfer of the materials.
- One of the most important potential applications of Zn(O,Se) layers is in optoelectronics, e.g., in the fabrication of solar cells. Zn(O,Se) is considered an n-type buffer layer for p-type absorbers, such as CdTe, CIGSe, and CZTS, in superstrate or substrate configurations.
- The buffer layer improves the quality of the p-n junction between the p-type absorber and the front contact. Also, the buffer layer can reduce interfacial charge recombination by accelerating electron-hole pairs separation.
- The application of the Zn(O,Se) as a buffer layer in TFSCs has not been widely investigated, and only one report is available about using ZnSe_{1-x}O_x (ZnSe rich) as an n-type buffer layer in TFSCs, with a very low solar cell efficiency. Thus, a deep investigation into the structural and optoelectronic properties of Zn(O,Se) layers and an improvement in the overall solar cells performance based on the n-type Zn(O,Se) buffer layer and p-type absorbers of TFSCs are required as part of the development of TFSCs.

Based on the literature review, this doctoral thesis has the following aims:

1. To deposit and develop a wide band gap Zn(O,Se) layer using PLD technique. Also, to apply the Zn(O,Se) as an alternative buffer layer for the conventional toxic CdS buffer layer.
2. To investigate systematically the effect of the substrate temperature on the structural, electrical, and optical properties of the Zn(O,Se) layers.
3. To investigate the effect of the laser fluences on the structural and optoelectronic properties of the Zn(O,Se) layers.
4. To fabricate and study the complete solar cell structures based on the Zn(O,Se) buffer layer and CIGSe absorber, and compare its solar cells parameters with the solar cell parameters of the reference cells based on CdS buffer layer.

2 Experimental Part

In this section, an overview of all experimental procedures performed during this work are presented. However, a detailed report on the step-by-step deposition of the Zn(O,Se) layers, fabrication of thin film solar cells, and their complete characterization has been represented in the publications listed in Appendix 1 as papers I, II, and III.

2.1 Deposition of Zn(O,Se) Layers

2.1.1 Preparation of the Substrates

Soda–lime glass substrates of $3.6 \times 3.6 \text{ cm}^2$ in size were prepared and ultrasonically cleaned for 15 min in a 20% solution of Decon 90 and deionized (DI) water, respectively, at 50°C . The substrates were dried under filtered air flow and then exposed to the Nova Scan Digital UV–Ozone cleaning system for 15 min.

2.1.2 Preparation of the PLD Targets

Commercial ZnO, ZnSe, and (ZnO:ZnSe) targets of 25.4 mm diameter and 6 mm thickness for PLD were prepared by hot–pressing of the fine powders of ZnO, ZnSe, and premixed fine powders of ZnO = 75 at% and ZnSe = 25 at% (99.99% purity, Testbourne Ltd).

2.1.3 Zn(O,Se) Deposition

The deposition was completed by using a Neocera Pioneer 120 PLD system equipped with a UV excimer laser, $\lambda = 248 \text{ nm}$ generated from KrF (Coherent Compex Pro 102 F). The laser beam was focused on approximately 5 mm^2 spots on the surface of the Zn(O,Se) target. The distance between the target and substrate was 9 cm. The deposition was done in a high vacuum and nitrogen back–pressure. In the case of high vacuum deposition, the pressure inside the deposition chamber was around $3 \times 10^{-6} \text{ Torr}$, and in the case of the nitrogen back–pressure deposition, the deposition chamber was filled with the 50 mTorr of nitrogen pressure at a constant nitrogen flow rate of 9 sccm. For comparison, ZnO and ZnSe layers were also deposited as a reference by PLD at 500°C in a high vacuum and under nitrogen back–pressure. The substrate was rotated during the deposition process for uniform distribution of the ablated materials onto the substrate surface. The target was rotated and rastered to avoid local heating and uniform consumption of the target materials. Different studies were performed as follows:

- (a) The study of the T_s effect on the properties of the Zn(O,Se) layers (paper I): The Zn(O,Se) layers were deposited by PLD in nitrogen back–pressure. The T_s was varied from room temperature (RT) to 600°C , while other deposition parameters were constant: 80 min deposition time, 200 mJ pulse energy, 10 Hz laser pulse repetition rate, 50 mTorr of nitrogen back–pressure, 9 sccm nitrogen flow rate.
- (b) The study of the laser fluence effect on the properties of the Zn(O,Se) layers (paper II): The Zn(O,Se) layers were deposited in a high vacuum at laser fluences of 4, 5, and 6 J cm^{-2} , while other deposition parameters were constant: 80 min deposition time, 500°C substrate temperature, 10 Hz laser pulse repetition rate.

2.2 Fabrication of the Solar Cells

Glass/Mo/CIGSe/ZnOSe/i-ZnO/ZnO:Al solar cells were fabricated in the substrate configuration (paper III) as follows: Firstly, the Mo layer was sputtered onto SLG substrates of $2 \times 2 \text{ cm}^2$ size as a back contact followed by the co–evaporation of the $\text{Cu}_{0.89}\text{In}_{0.77}\text{Ga}_{0.23}\text{Se}_{1.10}$ absorber layer using a three–stage process at the T_s of approximately

550°C according to the Ångström Solar Center procedure at Uppsala University [39,83]. Then, an amorphous ZnO_{0.73}Se_{0.27} (a-Zn(O,Se)) buffer layer was deposited onto the CIGSe absorber and SLG substrates by PLD at RT–500°C in high vacuum, with the following layer thicknesses of 300, 200, and 100 nm. Next, a RF–sputtering technique was used to deposit the *i*-ZnO and ZnO:Al top electrode sequentially from an undoped and a 1.5 at% Al–doped ceramic ZnO target. Each of the three samples was sectioned into small cells with an active area of approximately 0.06 cm² by mechanical scribing. Finally, the prepared complete solar cells were characterized, as shown in Table 2.1.

2.3 Characterization of Zn(O,Se) Layers and Solar Cells

The structural, optical, and electrical properties of the prepared Zn(O,Se) layers were characterized. Also, the solar cell characteristics of the CIGSe/Zn(O,Se) devices were characterized and investigated by different techniques, as listed in Table 2.1.

Table 2.1. Analytical techniques used to characterize the Zn(O,Se) layers and CIGSe/Zn(O,Se) solar cells.

Properties	Characterization techniques	Apparatus	Refs
Crystal structure, phase composition, and crystallite sizes	XRD	Rigaku Ultima IV	I, II
Phase composition	Raman	Horiba's LabRam HR800	I
Surface and cross-sectional morphology, layers thickness	HR-SEM	HR-SEM ZEISS ULTRA-55, ZEISS MERLIN	I, II, III
Elemental composition	EDX, XRF	Bruker EDX–XFlash6/30 detector and Bruker ESPRIT system 1.82. Spectro X–Lab 2000	I, II, III
Chemical state, surface chemical composition	XPS	Kratos Axis Ultra DLD	I, III
Optical properties, band gap	UV–Vis spectroscopy	Shimadzu UV–1800	I, II, III
Electrical properties	Hall effect measurements joined with Van Der Pauw method	MMR's variable temperature Hall effect measurements system	I, II
Solar cell parameters	<i>J</i> – <i>V</i> characteristics	Keithley 2400 source meter, Autolab PGSTAT 30, Newport class AAA solar simulator	III
Quantum efficiency	EQE	Monochromator (Carl Zeiss SPM-2, <i>f</i> = 40 cm)	III

3 Results and Discussion

The following sections 3.1–3.3 report the results of a systematic study of the structural, optical, and electrical properties of the Zn(O,Se) layers as a function of PLD deposition conditions. Also, the properties of the fabricated CIGSe/Zn(O,Se) solar cells were reported. These results have been published in papers I, II, and III as shown in Appendix 1.

3.1 Effect of the Substrate Temperature on the Properties of the Zn(O,Se) Layers

Zn(O,Se) layers were deposited onto SLG substrates by PLD at 50 mTorr of nitrogen back–pressure according to the experimental procedure presented in section 2.1.3a. To investigate the effect of the T_s on the structural and optoelectronic properties of Zn(O,Se) layers, the T_s was varied from RT to 600°C. The obtained results were discussed and presented in paper I.

3.1.1 Structural, Morphological and Compositional Analysis

The structural, compositional, and morphological properties of the Zn(O,Se) layers deposited in nitrogen back–pressure were analyzed by XRD, Raman, SEM, EDX, and XPS techniques. All Zn(O,Se) layers deposited from RT to 400°C were amorphous according to the XRD results as shown in Fig 3.1a. Also, Fig 3.1b shows the XRD patterns of the Zn(O,Se) layers deposited at 500–600°C combined with the XRD patterns of the reference ZnSe and ZnO phases deposited at 500°C for comparison. The ZnSe layer showed an XRD peak at 27.47°, which is well–indexed to the (111) plane of the ZnSe cubic phase [84,85], while the ZnO layer showed an XRD peak at 34.53°. This peak is assigned to the (002) plane of the ZnO wurtzite structure, as reported in the literature [86–92].

Zn(O,Se) layers grown at 500°C showed a single XRD peak at 30.94° together with a residual amorphous hump. Thus, that peak appearing at 30.94° corresponds to the (002) plane for $ZnO_{1-x}Se_x$ in which the x values varied from 0 to 0.12, as reported in the literature [31]. Therefore, a polycrystalline Zn(O,Se) phase mixed with an amorphous phase is formed at 500°C. With increasing T_s to 550°C, the XRD diffractogram showed two distinct peaks at 27.70° and 34.09°. These peaks do not correspond to the reference ZnSe and ZnO phases, as their diffractions appeared at different 2θ values; in other words, two different solid solutions had formed. By considering the solubility of the selenium in ZnO and oxygen in ZnSe, the XRD peak located at 27.70° and 34.09° can be attributed to the formation of $ZnSe_{1-y}O_y$ and $ZnO_{1-z}Se_z$ solid solutions, where y and $z \ll 1$ indicates the limited solubility of selenium and oxygen in ZnO and ZnSe, respectively. With further increase in the T_s to 600°C, a shift in both peaks towards 2θ values of the reference ZnO and ZnSe phases is observed. This is an indication of a further decrease in the Se and O solubility in ZnO and ZnSe, respectively. In other words, the formation of ZnSe rich and ZnO rich mixture phases takes place. The corresponding crystallite sizes of the Zn(O,Se) layers (for the peaks located in the 2θ at 30.94–34.09° range in radians) were calculated via the Scherrer form [93]. Thus, the crystallite sizes increased from 12.60 to 20.50 nm with increasing T_s from 500 to 600°C as mentioned in Table 3.3.

Further structural investigation of the Zn(O,Se) layers was done by Raman spectroscopy at RT. The Zn(O,Se) layers grown at 100–600°C showed a weak band of Raman scattering located at 127 cm^{-1} as shown in Fig 3.2a,b which corresponds to the Zn(O,Se) phase. Moreover, the Zn(O,Se) layers deposited at T_s ranging from 100 to 500°C illustrated two strong broad bands at 220 cm^{-1} and 550 cm^{-1} , as shown in Fig 3.2a,b which

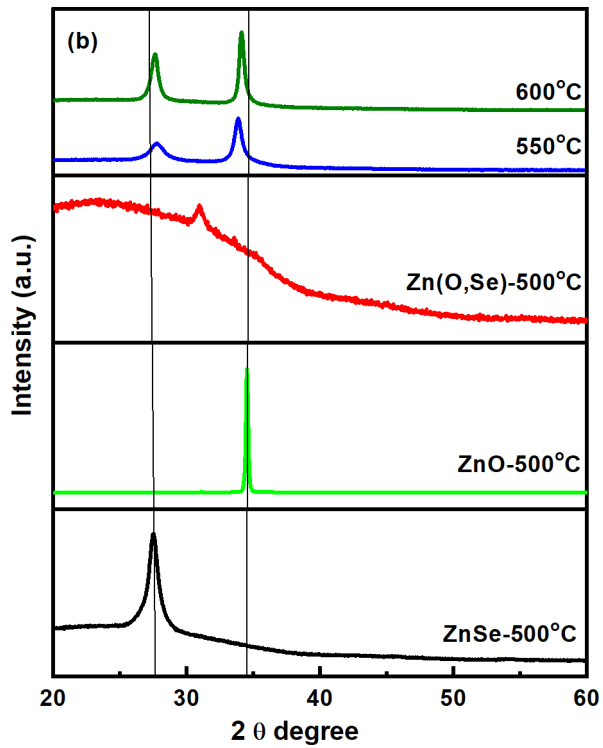
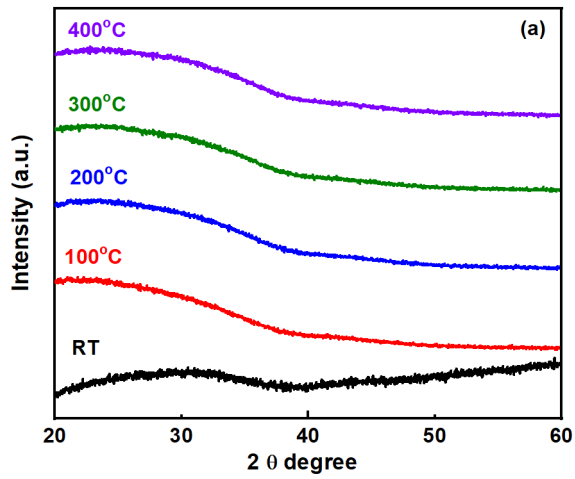


Figure 3.1. XRD patterns of the Zn(O,Se) layers deposited onto SLG substrate at (a) RT–400°C, and (b) 500–600°C with XRD pattern of ZnSe and ZnO phases deposited at 500°C.

Table 3.1. The modified Auger parameters of the Zn(O,Se) layers deposited at 500–600°C under nitrogen back–pressure.

T_s (°C)	positions	positions	$L_3M_{45}M_{45}$	$L_3M_{45}M_{45}$	m-AP	m-AP
	(eV) Zn 2p	(eV) Se 3d	K.E (eV) Zn 2p	K.E (eV) Se 3d	α' (eV) Zn 2p	α' (eV) Se 3d
500	1021.23	53.74	989.27	1306.58	2010.50	1360.32
550	1021.24	53.60	989.38	1306.78	2010.63	1360.38
600	1021.20	53.63	989.41	1306.86	2010.61	1360.50

XPS measurement errors are: for binding energy ± 0.02 eV, for quantification $\pm 10\%$

also correspond to the Zn(O,Se) formation. However, a noticeable shift to 248 cm^{-1} and ($565/575\text{ cm}^{-1}$) in both band positions can be seen for Zn(O,Se) layers grown at 550 and 600°C as in Fig 3.2b. These Raman bands are extremely close to the LO phonon modes of ZnSe [56, 94–97] and the LO phonon E_1 symmetry mode of ZnO [56,98–100] respectively. Thus, these shifts in both Raman bands explain that the ternary Zn(O,Se) polycrystalline phase obtained at 500°C shifted towards the formation of $ZnSe_{1-y}O_y$ and $ZnO_{1-z}Se_z$ solid solutions as a result of the limited solubility of Se in ZnO and O in ZnSe at a T_s of 550–600°C. Also, the shift is attributed to the presence of oxygen and selenium vacancies at those T_s [101]. Besides those Raman bands, extra weak bands located at 275 cm^{-1} started appearing at T_s from 550°C. This additional Raman scattering is attributed to the intrinsic host lattice defects, like selenium and oxygen vacancies or Zn interstitials, which become activated at a high T_s of 550 and 600°C [101].

High resolution XPS was also used to identify the possible phases of each species in the Zn(O,Se) layers deposited at 500–600°C. Figs 3.3a–d shows the XPS spectra of wide survey, Zn 2p, O 1s, and Se 3d of Zn(O,Se) layers deposited at 500°C. Fig 3.3a presents the wide survey binding energy of Zn(O,Se) layers, which contain only C, Zn, O, and Se. No impurities were detected. The binding energy of the adventitious C 1s peak at 284.6 eV was used for charge corrections. Fig 3.3b illustrates the Zn 2p XPS core–level spectra. Only one set of doublets was used to fit the Zn 2p spectra. None of the fitting parameters, FWHM, area, nor doublet separation, were fixed. The spectrum represents peaks at 1021.23 eV and 1044.55 eV related to Zn $2p_{3/2}$ and Zn $2p_{1/2}$, respectively. The spin–orbit splitting of 23.32 eV between the peaks is in good agreement with the value for the Zn^{2+} oxidation state [102–105]. Two peaks of various forms of oxygen were fitted for O 1s, as in Fig 3.3c. The first oxygen peak is located at the lower binding energy of 529.86 eV and

Table 3.2. Binding energies and modified Auger parameters (m-AP) of Zn(O,Se) layers deposited at 500°C under nitrogen back–pressure and comparison with the literature data for ZnO and ZnSe.

Samples	$Zn2p_3/Se3d_5$	$L_3M_{45}M_{45}$	m-AP	Refs
	peak position (eV)	Kinetic energy (eV)	α' (eV)	
ZnO	1022.10	987.70	2009.80	106
ZnO	1021.60	988.80	2010.40	107
ZnSe	1022.00	989.50	2011.50	106
Zn(O,Se), Zn2p	1021.23	989.30	2010.50	paper I
SeO ₂	58.80	1301.60	1360.40	106
Zn(O,Se), Se3d	53.74	1306.58	1360.32	paper I

XPS measurement errors are: for Binding energy ± 0.02 eV, for quantification $\pm 10\%$

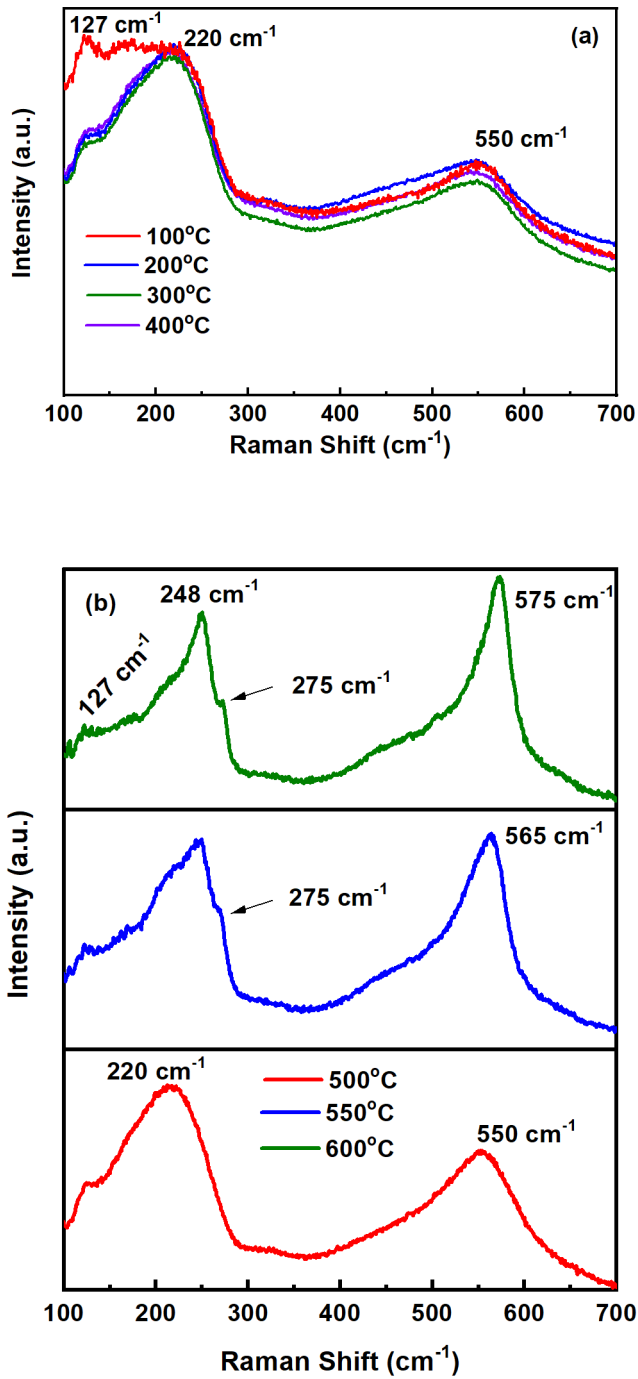


Figure 3.2. Raman spectra of the Zn(O,Se) layers deposited onto SLG substrate at (a) 100–400°C and (b) 500–600°C.

corresponds to oxygen ions in the Zn-O bonding of the Zn(O,Se) layers [102–105]. The second peak positioned at 531.29 eV is referred to the OH group absorbed onto the surface of the Zn(O,Se) layers [103]. Fig 3.3d shows the Se 3d XPS spectra with two sets of doublets; each doublet includes two peaks because of the spin–orbit splitting of the Se 3d level. The essential peak appeared at 53.74 eV binding energy and the other at 54.53 eV, which belong to Se 3d_{5/2} and Se 3d_{3/2} of the Zn-Se bonding, respectively [106]. The trend is similar for Zn(O,Se) layers grown at 550 and 600°C except for minor shifts in the binding energies, as in Table 3.1 and Figs S.1,S.2 of appendix 2, due to the formation of different solid solutions of ZnSe_{1-y}O_y and ZnO_{1-z}Se_z. The modified Auger parameters (m-AP, α') for the Zn(O,Se) layers deposited at 500°C were calculated from the experimental binding energies of the Zn 2p_{3/2} and Se 3d_{5/2} photoelectron peaks and kinetic energies of Zn L₃M₄₅M₄₅ and Se L₃M₄₅M₄₅ Auger peak values [107–109]. Hence, the Zn 2p_{3/2} and Se 3d_{5/2} peak positions, kinetic energies of Zn/Se L₃M₄₅M₄₅ Auger peak values, and modified Auger parameters of the reference ZnO, ZnSe, and SeO₂ phases were compared to the corresponding calculated parameters of the Zn(O,Se) layers [107–109], as indicated in Table 3.2. By considering the Wanger plot [108,109] and careful analysis of the compared data, we found that the estimated three parameters of the Zn(O,Se) layers are dissimilar from those values of the reference phases, which means that various compounds have been formed, i.e., polycrystalline ternary Zn(O,Se) layers have been deposited at 500°C. Furthermore, the modified Auger parameters, core-level peak positions, and Auger peak kinetic energies of the Zn(O,Se) layers deposited at 550–600°C are dissimilar from that of Zn(O,Se) layers grown at 500°C as listed in Table 3.1. Thus, that is further evidence for the formation of different solid solutions of ZnSe_{1-y}O_y and ZnO_{1-z}Se_z, as shown by the Raman and XRD results.

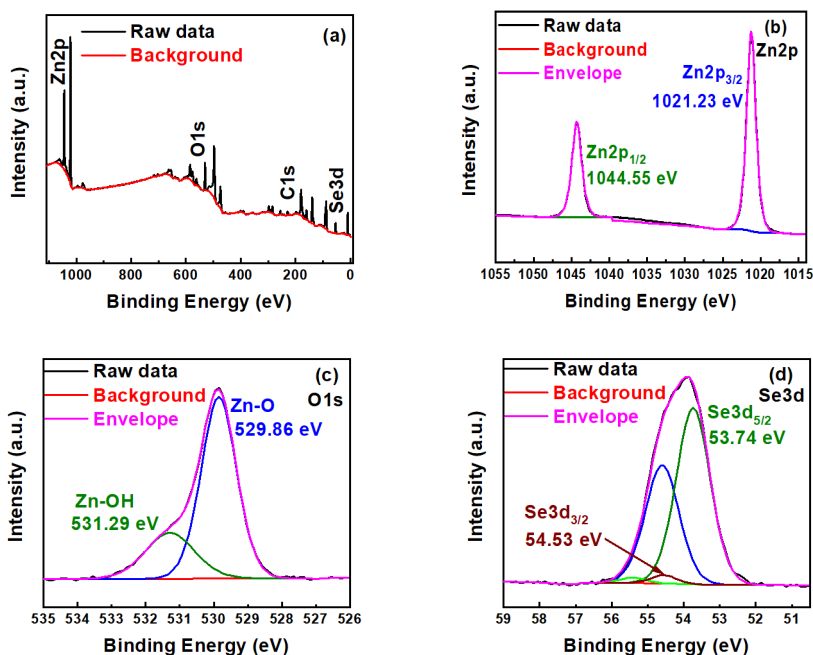


Figure 3.3. XPS spectra of Zn(O,Se) layers deposited onto SLG substrate at 500°C (a) wide survey, (b) Zn 2p, (c) O 1s, and (d) Se 3d.

Furthermore, the HR-SEM micrographs show the formation of the uniform, compact and well-adherent Zn(O,Se) layers on the SLG substrate surface in the whole range of the T_s as shown in Figs 3.4. Moreover, the grain size of the Zn(O,Se) layers increased as the T_s increased from RT to 500°C, with an average grain size in the range of 15–86 nm. However, at the T_s of 550–600°C, the grain size showed a decreasing trend. Furthermore, the cross-sectional views and Table 3.3 show that the thickness of the grown layers was reduced from 733 to 459 nm as the T_s changed from RT to 600°C. Thus, this phenomenon is connected with the formation of highly ordered, denser, and more compact polycrystalline layers with an increase in the T_s [110].

Table 3.3 shows the elemental ratios of the Zn(O,Se) layers grown at RT–600°C as measured by EDX. For all T_s ranges, the Zn(O,Se) layers showed a relatively stable elemental Zn content. However, a negligible fluctuation in the oxygen and selenium content was observed with increasing T_s . Thus, this can be associated with the effect of nitrogen back-pressure, which decreases the mean free path and kinetic energy of the ablated particles. As a result, stable ratios of the elements are maintained, in particular for Se.

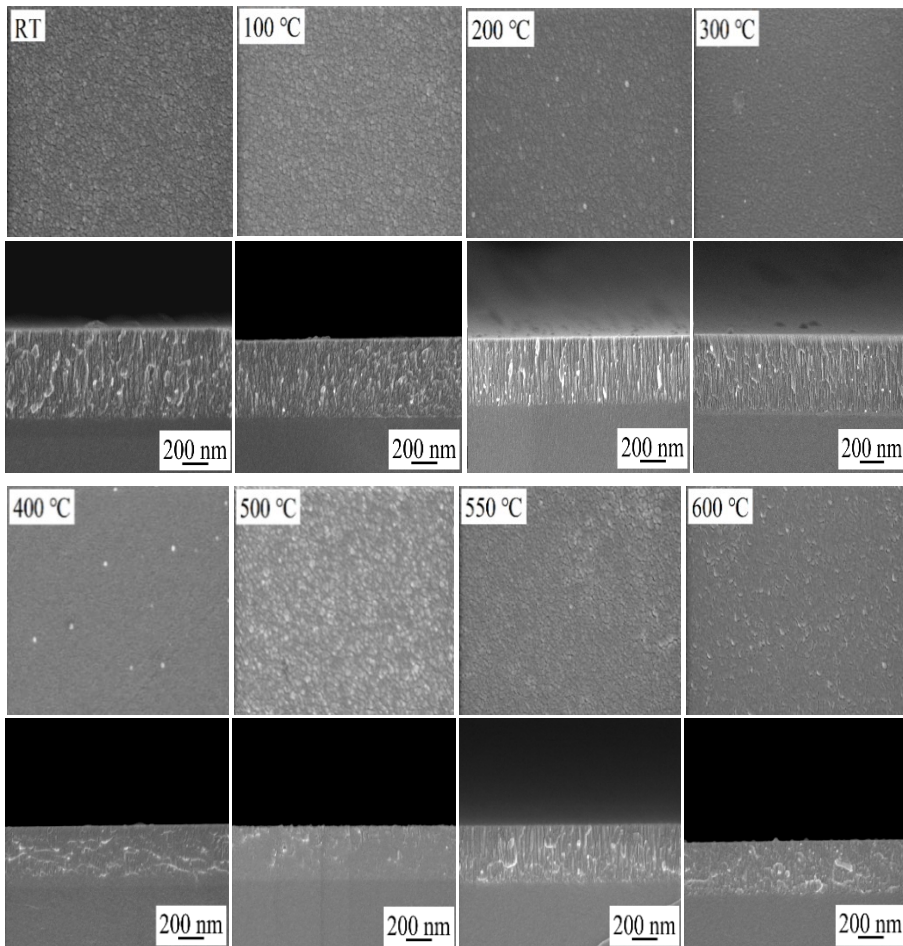


Figure 3.4. Surface and cross-sectional HR-SEM micrographs of Zn(O,Se) layers grown onto SLG substrate at RT–600°C.

Table 3.3. The crystallite sizes, atomic ratios, film thicknesses, and optical band gap of the Zn(O,Se) layers deposited at RT–600°C under nitrogen back–pressure.

Ts (°C)	Crystallite sizes (nm) ^a	EDX atomic ratios (at%) ^b			Film thickness (nm)	Band gap (eV)
		Zn	O	Se		
RT	-----	50	39	11	733	2.76
100	-----	50	38	12	639	2.98
200	-----	50	36	14	554	3.00
300	-----	50	36	14	647	2.80
400	-----	50	36	14	512	2.83
500	12.60 ± 0.80	50	39	11	454	3.00
550	13.40 ± 0.13	50	37	13	484	2.90, 3.28
600	20.50 ± 0.90	50	37	13	459	3.16, 3.29

^a represent standard deviation (s.d.), ^b EDX measurement error is ± 0.5%

Also, high resolution XPS was used to quantitatively study the surface chemical composition of the Zn(O,Se) layers deposited at 500–600°C. Thus, the selenium content remained unchanged at 11 at% for the T_s range 500–600°C, while a noticeable increase in the Zn content from 52 to 57 at% was noticed with an increase in the T_s from 500°C to 550–600°C. However, a significant decrease in the oxygen ratio from 37 to 32 at% was found in the same temperature interval.

3.1.2 Optical Properties

Figures 3.5a,b shows the UV–Vis transmittance spectra of Zn(O,Se) layers deposited at RT–600°C on the SLG substrates. All the deposited layers showed a transparency around 80% in the visible range except the thicker layers deposited at RT and 100°C, which exhibited a transparency less than 80%. It can be seen that the absorption edges shifted to a shorter wavelength (blue shift) with the increase in the T_s. The shift of the absorption edges can be attributed to the change in the electronic band structure and thickness of the Zn(O,Se) layers with the T_s [111,112]. Thus, a change in the electronic band structure of the Zn(O,Se) layers due to the formation of some defects, which creates a localized state in the band gap, leads to an increase in the band gap [111,113]. The thicker layers increase the width of the localized states in the optical band gap, accordingly, reducing the optical absorption edges with the reverse effect [111,112]. The optical E_g of the Zn(O,Se) layers was calculated based on the Tauc relation [114,115]. The optical E_g of the Zn(O,Se) layers varied from 2.76 eV to 3.29 eV with the increase in the T_s from RT to 600°C as listed in Table 3.3. This variation in the optical band gap can be related to the shift in the absorption edges and change in the thickness of the layers with the change in the T_s. Also, two different optical E_g values were observed for Zn(O,Se) layers grown at 550 and 600°C, which is attributed to the coexistence of two different solid solutions. This is in excellent agreement with the XRD, Raman, and XPS data.

Furthermore, all the deposited layers showed interference patterns, which may be attributed to the multiple reflections at air–layers and layers–substrate interfaces as a result of the dissimilar refractive indexes of the Zn(O,Se) layers, air, and the SLG substrate [116].

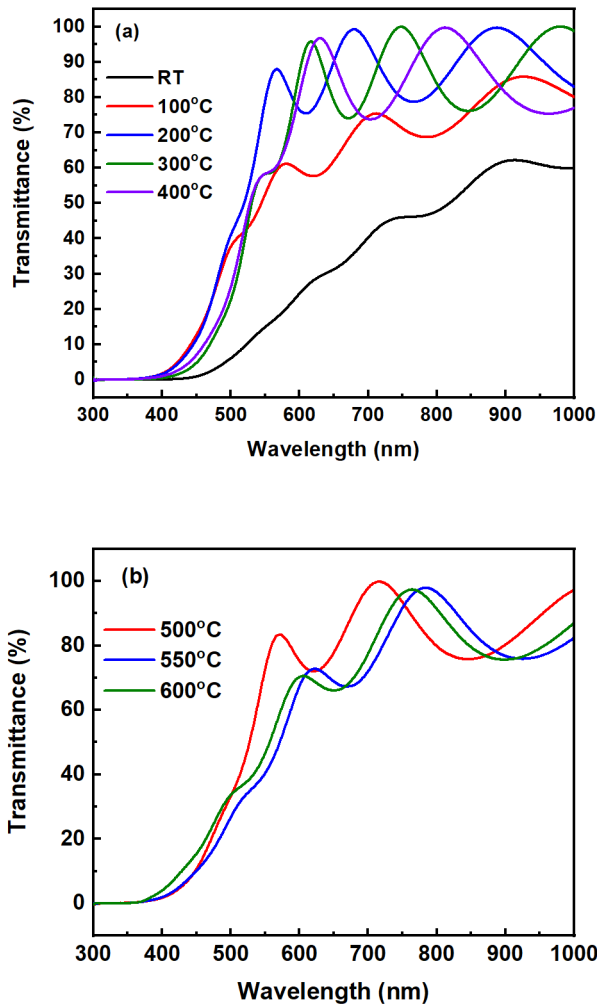


Figure 3.5. UV-Vis transmittance spectra of Zn(O,Se) layers deposited onto SLG substrate at (a) RT–400°C and (b) 500–600°C.

3.1.3 Electrical Properties

Since we propose Zn(O,Se) layers as a potential buffer layer for solar cells and other optoelectronic devices, it is vitally important to investigate the electrical properties of these layers. Thus, using the Hall effect measurements method at RT, we characterized the carrier mobility, carrier density, and resistivity of Zn(O,Se) layers as a function of T_s . It was revealed that all Zn(O,Se) layers deposited below 500°C were relatively highly resistive as a result of the amorphous structure of the Zn(O,Se) layers. Table 3.4 shows the electrical properties of the Zn(O,Se) layers grown at 500–600°C based on the Hall effect measurements. The sign of the Hall coefficient reveals that the electrons are the majority carriers in the PLD deposited Zn(O,Se) layers under nitrogen back-pressure, which corresponds to the n-type conductivity of the deposited Zn(O,Se) thin films. The resistivity of the Zn(O,Se) layers grown at 500°C was $2.1 \times 10^5 \Omega\text{-cm}$, the electron density

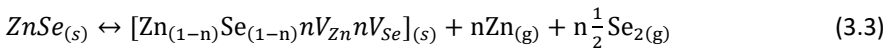
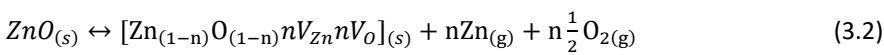
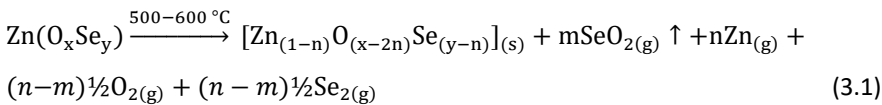
Table 3.4. The electrical properties of the Zn(O,Se) layers deposited in the temperature region of 500–600°C under nitrogen back–pressure.

T _s (°C)	Hall coefficient (cm ³ /C)	Resistivity (Ω·cm)	Carriers density (cm ⁻³)	Carriers mobility (cm ² /Vs)
500	-2.4 × 10 ⁷	2.1 × 10 ⁵	3.0 × 10 ¹¹	113.0
550	-6.0 × 10 ⁶	2.3 × 10 ⁵	1.0 × 10 ¹²	26.2
600	-2.0 × 10 ²	5.4 × 10 ¹	3.4 × 10 ¹⁶	3.4

Hall effect measurement error is ± 5.0%

was 3.0 × 10¹¹ cm⁻³, and the carrier mobility was 113.0 cm²/Vs. As the T_s increased to 550°C, the mobility remarkably decreased to 26.2 cm²/Vs, while the carrier concentration increased by one order of magnitude to 1.0 × 10¹² cm⁻³. With further increase in the T_s to 600°C, the carrier concentration significantly increased to 3.4 × 10¹⁶ cm⁻³, while the mobility and resistivity sharply decreased to 3.4 cm²/Vs and 5.4 × 10¹ Ω·cm, respectively.

To clearly understand the change in the electrical properties of Zn(O,Se) layers grown at 500–600°C, we conducted some thermodynamic studies for the Zn(O,Se) system as in paper I [117]. Specifically, the change in Gibbs free energy (ΔG) of formation for ZnSe, ZnO, and SeO₂ was calculated based on the HSC Chemistry Ver. 6.0 software and compared for T_s of 500–600°C, as seen in Table 3.5. Based on these preferred thermodynamic reactions, it was found that ZnO is the most stable phase in the Zn(O,Se) system because it shows the highest Gibbs free energy of formation. The formation of SeO₂ reduces the partial pressures of selenium and oxygen in ZnSe and ZnO, respectively. Furthermore, the partial pressure of Zn in zinc oxide is less than the partial pressure of Zn in zinc selenide, which produces a Zn–rich composition in the vapor phase of the Zn(O,Se) system. As a result, of the increased partial pressure of zinc vapor, more oxygen and selenium vacancies (n-type intrinsic defects) will be formed; consequently, this will increase the overall carrier concentration in the Zn(O,Se) layers. Thus, the carrier mobility is systematically reduced with the T_s as the carrier concentration is increased. Probably, the systematic decrease in the carrier mobility was related to the carrier scattering via ionized selenium/oxygen vacancy defects with high carrier concentrations at high temperatures. The reactions (3.1–3.8) below present the dissociation of Zn(O,Se), ZnO, and ZnSe in the gas phase and the following formation of the Frenkel defects at the equilibrium between the solid and gas phase [117,118]. The nitrogen back–pressure has the ability to inhibit the transfer of the materials through the gas phase to the substrate by decreasing the kinetic energy and the mean free path of the ablated particles. The reduced mean free path has an effect of keeping the O and Se content stable in the Zn(O,Se) layers. The EDX analysis represents a relatively stable O and Se content in the whole T_s range.



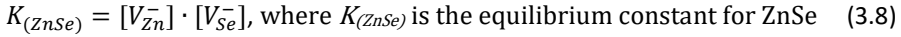
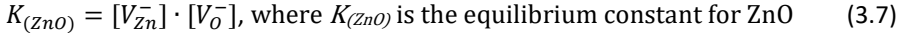


Table 3.5. The changes in the Gibbs free energies calculated for the formation of ZnO, ZnSe and SeO₂ at temperature range of 500–600°C.

Reaction	ΔG at 500°C (kcal/mole)	ΔG at 550°C (kcal/mole)	ΔG at 600°C (kcal/mole)
$Zn(g) + \frac{1}{2} O_2(g) \leftrightarrow ZnO(s)$	-74.76	-72.24	-69.73
$Zn(g) + \frac{1}{2} Se_2(g) \leftrightarrow ZnSe(s)$	-51.33	-49.02	-46.72
$\frac{1}{2} Se_2(g) + O_2(g) \leftrightarrow SeO_2(g)$	-30.97	-30.17	-29.38

3.2 Effect of the Laser Fluences on the Properties of the Zn(O,Se) Layers

Zn(O,Se) layers were grown onto SLG substrates by PLD at 500°C according to the experimental procedure presented in section 2.1.3b. The structural and optoelectronic properties of the Zn(O,Se) layers were investigated as a function of the laser fluences, which varied from 4 to 6 J cm⁻². The findings are discussed and presented in paper II.

3.2.1 Structural, Morphological and Compositional Analysis

Surface and cross-sectional HR-SEM micrographs of the Zn(O,Se) layers grown at 500°C with changing laser fluences from 4 to 6 J cm⁻² are presented in Figs 3.6, which illustrate the growth of homogenous, dense, and well-adherent Zn(O,Se) layers to the SLG substrates. As can be seen from the cross-sectional micrographs, the thickness of the Zn(O,Se) layers increased from 340 to 445 nm with the change in the laser fluence from 4 to 6 J cm⁻². Thus, this result is attributed to the presence of large numbers of atoms and ions of Zn, O, and Se in the plasma plume at higher laser fluences [119]. The EDX elemental analysis of the deposited layers shows relatively stable elemental ratios of Zn, O, and Se throughout all applied laser fluences of 4, 5 and 6 J cm⁻² as seen in Table 3.6.

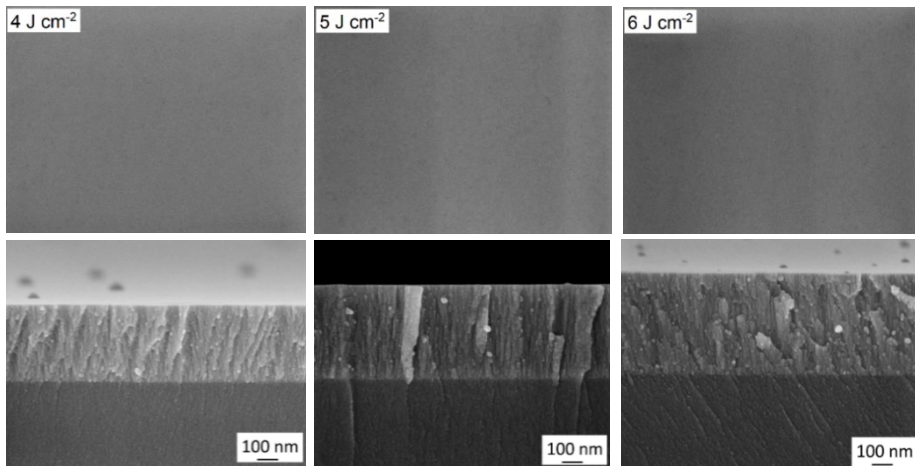


Figure 3.6. Surface and cross-sectional HR-SEM micrographs of Zn(O,Se) layers deposited onto SLG substrate at 500°C with different laser fluences of 4, 5, 6 J cm⁻².

Figure 3.7 represents the XRD patterns of the Zn(O,Se) layers deposited at 500°C onto SLG substrates using three laser fluences of 4, 5, and 6 J cm⁻² combined with XRD patterns of the reference ZnO and ZnSe phases grown by PLD at 4 J cm⁻² laser fluence and the same substrate temperature for comparison. The XRD patterns for the ZnO and ZnSe layers have been identified and explained in detail in section 3.1.1. However, all the deposited Zn(O,Se) layers showed a single XRD peak at 33.70° regardless of the applied laser fluence. This peak located at 33.70° was previously assigned to the (002) plane of ZnO_{1-x}Se_x, where x values varied from 0 to 0.12 [31,50,120]. Thus, the polycrystalline ternary Zn(O,Se) phase was formed at 500°C for all applied laser fluences. The difference in peak position between the Zn(O,Se) layers deposited in high vacuum [117] and nitrogen back–pressure is $\Delta 2\theta = 2.76$, which is attributed to the effect of the deposition atmosphere (nitrogen back–pressure). As shown in Fig 3.1b, the polycrystalline Zn(O,Se) was mixed with the amorphous phase. With increasing laser fluence from 4 to 6 J cm⁻², a significant increase in the crystallite sizes (for the peaks at 33.70°) from 34 to 42 nm was observed as shown in Table 3.6. Hence, that is attributed to the increased flux and high kinetic energy of the ablated materials in the plasma plume, which affected the crystallite size and density of the Zn(O,Se) layers [86,92,121].

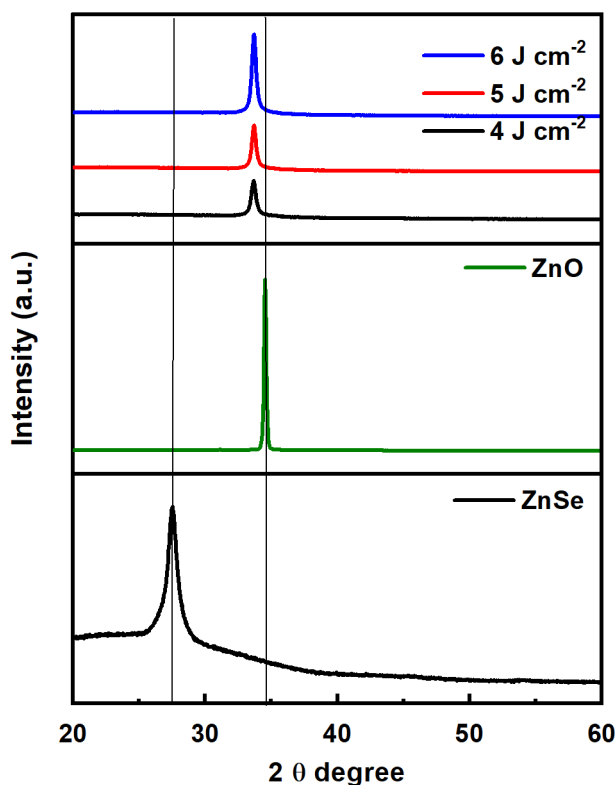


Figure 3.7. XRD patterns of Zn(O,Se) layers deposited onto SLG substrate at 500°C with different laser fluences of 4, 5, 6 J cm⁻², Combined with XRD patterns of ZnSe, ZnO layers deposited at 500°C and 4 J cm⁻² laser fluence.

Table 3.6. Crystallite sizes, atomic ratios, layer thicknesses, and optical band gaps of Zn(O,Se) layers deposited at 500°C with different laser fluences of 4–6 J cm⁻².

Laser fluences (J cm ⁻²)	Crystallite sizes (nm) ^a	EDX atomic ratios (at%) ^b			Layer thickness (nm)	Band gap (eV)
		Zn	O	Se		
4	34 ± 0.3	50.0	41.6	8.4	340	3.03
5	40 ± 0.4	50.0	41.0	9.0	419	2.94
6	42 ± 0.5	50.0	42.0	8.0	445	2.87

^a represent standard deviation (s.d.), ^b EDX measurement error is ± 1.0%

3.2.2 Optical Properties

Figure 3.8 illustrates the UV–Vis transmittance spectra of the Zn(O,Se) layers deposited at 500°C with changing laser fluences from 4 to 6 J cm⁻². All the prepared Zn(O,Se) layers are nearly transparent in the visible range of the spectra. The absorption edges shifted to a longer wavelength (redshift) as the laser fluence increased from 4 to 6 J cm⁻². This is because of an alteration of the electronic band structure of the Zn(O,Se) layers due to the formation of the localized defect states [122–125]. Thus, the valence band and the defect states experience valence band anticrossing, creating two divided bands [31,126]; as Zn(O,Se) layers are n-type, the Fermi level is located near the conduction band. Thus, the Se-derived band will be completely filled and functions as the top of the valence band, which redshifts the absorption edges. The observed redshift [80,127] in the absorption edges of the Zn(O,Se) layers with the increase in the laser fluence gradually reduced the optical E_g values of the Zn(O,Se) layers from 3.03 to 2.87 eV.

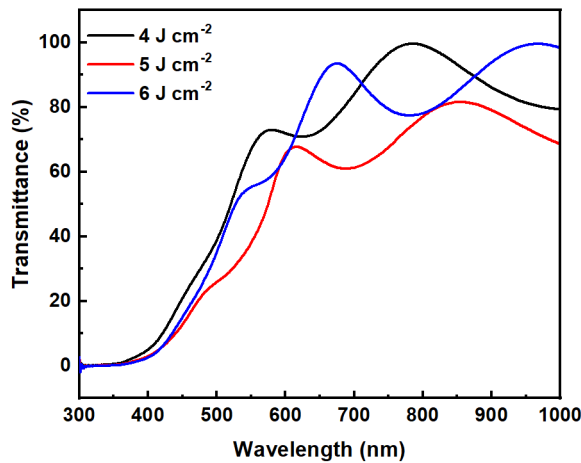


Figure 3.8. UV–Vis transmittance spectra of Zn(O,Se) layers deposited onto SLG substrate at 500°C with different laser fluences of 4, 5, 6 J cm⁻².

3.2.3 Electrical Properties

Table 3.7 illustrates the electrical properties of the Zn(O,Se) layers grown in a high vacuum at 500°C as a function of changing laser fluences from 4 to 6 J cm⁻². The negative sign of the Hall coefficient indicated the n-type conductivity of all the prepared Zn(O,Se) layers. The electron density gradually increased from 4 × 10¹⁴ cm⁻³ to 8 × 10¹⁴ cm⁻³ and

the resistivity decreased from $6 \times 10^3 \Omega\text{-cm}$ to $4 \times 10^3 \Omega\text{-cm}$ as the laser fluence changed from 4 J cm^{-2} to 5 J cm^{-2} . Similarly, a significant increase in the carrier concentration to $4 \times 10^{15} \text{ cm}^{-3}$ and a significant reduction of the resistivity to $6 \times 10^2 \Omega\text{-cm}$ were observed as the laser fluence increased to 6 J cm^{-2} . Furthermore, the carrier mobility was relatively constant for all applied laser fluences, with values around $2\text{--}3 \text{ cm}^2/\text{Vs}$. To explain the electrical behavior of the Zn(O,Se) layers as a function of the laser fluence, we referred to the thermodynamic studies shown in section 3.1.4 and paper I. Hence, the study indicated the formation of oxygen/selenium vacancies (n-type intrinsic defects), in other words Frenkel defects, which increase the overall carrier concentration of the polycrystalline Zn(O,Se) layers [51,128]. Also, the scattering lifetime of the carriers was optimal and sufficiently long for the Zn(O,Se) layers grown at high laser fluences, which increased the carrier concentration [51,129]. Thus, the increased carrier concentration of the Zn(O,Se) layers at high laser fluences led to the reduction in the resistivity with laser fluence [51,129].

Table 3.7. The electrical properties of the Zn(O,Se) layers deposited at 500°C with different laser fluences of $4\text{--}6 \text{ J cm}^{-2}$.

Laser fluences (J cm^{-2})	Resistivity ($\Omega\text{-cm}$)	Carriers density (cm^{-3})	Carriers mobility (cm^2/Vs)
4	6×10^3	4×10^{14}	3
5	4×10^3	8×10^{14}	2
6	6×10^2	4×10^{15}	3

Hall effect measurements error is $\pm 1.0\%$

3.3 Application of Zn(O,Se) as a Buffer Layer with CIGSe Solar Cells

For proof of the concept demonstrated above, we applied Zn(O,Se) layers prepared by PLD at $\text{RT}\text{--}500^\circ\text{C}$ as a buffer layer with CIGSe solar cells in a substrate configuration (glass/Mo/CIGSe/ZnOSe/i-ZnO/ZnO:Al). The solar cell parameters were studied as a function of the thickness of the Zn(O,Se) buffer layer from 300 to 100 nm. Furthermore, the solar cell parameters of the CIGSe/Zn(O,Se) devices were compared to the solar cell parameters of reference cell CIGSe/CdS and presented in paper III. It was found that, the Zn(O,Se) buffer layers deposited at RT reported the best device performance. However, the Zn(O,Se) buffer layers deposited at $100\text{--}500^\circ\text{C}$ had very low device performance, and were not considered for further investigation. Hence, this may be attributed to the absorber surface deterioration due to high temperature PLD process or may be diffusion of zinc or oxygen into the absorber at those deposition temperatures. Thus, all the following discussions are devoted to the Zn(O,Se) buffer layers deposited at RT.

3.3.1 Optical and Elemental Analysis of Amorphous Zn(O,Se) Layers

Figure 3.9 shows the UV–Vis transmittance spectra of the amorphous Zn(O,Se) layers with three thicknesses of 300, 200, and 100 nm grown onto the SLG substrate by PLD in a high vacuum at RT. As can be seen, the Zn(O,Se) layer with the 100 nm thickness has an average transparency of about 85% in the visible region of the spectra, while the layers with 200 and 300 nm thicknesses exhibited an average transparency around 75%. Furthermore, the absorption edges shifted to shorter wavelengths (blue shift), from ~ 485 to $\sim 375\text{nm}$, with decreasing layer thickness from 300 to 100 nm. Thus, this is related to the disordered (defect) structure in the amorphous layers, which form localized defect states in the electronic structure of the Zn(O,Se) layers [111,113,122]. Hence, these

defect states and the valence band experience valence band anticrossing, forming two separate bands [31,126], which lead to the blue shift of the absorption edges, as discussed earlier in sections 3.1.2 and 3.2.2. The optical E_g of the layer was estimated using the Tauc relation [114,115]. Hence, the optical E_g values of the Zn(O,Se) layers are 2.99, 3.00, and 3.05 eV for 300, 200, and 100 nm thicknesses, respectively, i.e., a minor increase in the optical E_g value to 3.05 eV is observed with the decrease in the Zn(O,Se) layer thickness to 100 nm.

Moreover, the elemental ratios of the amorphous Zn(O,Se) layers were 50.0, 36.5, and 13.5 at% for Zn, O, and Se, respectively, based on EDX analysis for all three different thicknesses, i.e., these values did not change with the change in the layer thickness. Thus, the selenium-to-oxygen composition ratio $[Se]/([O]+[Se])$ of the amorphous Zn(O,Se) layers was constant at 0.27.

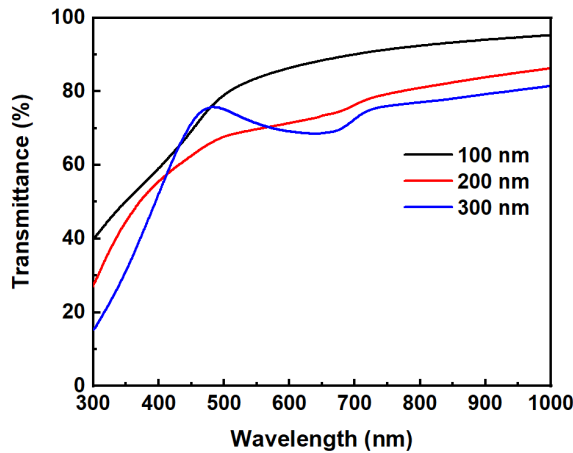


Figure 3.9. UV-Vis transmittance spectra of amorphous Zn(O,Se) layers deposited at RT onto SLG substrate with different thicknesses of 300, 200, 100 nm.

3.3.2 XPS Depth Profile Analysis of the CIGSe/Zn(O,Se) Interface

Figure 3.10 shows the XPS depth profile analysis of the CIGSe/Zn(O,Se) structure. In the topmost zone up to 100 nm, only the composition of the Zn(O,Se) layer is shown. Zn 2p, O 1s, and Se 3d presented relatively constant concentrations with an average around 52.5, 36.0, and 11.5 at%, respectively as seen in Table 3.8. These minor deviations in Zn, O, and Se concentrations from the results obtained by EDX can be related to the XPS measurement accuracy. However, at the CIGSe/Zn(O,Se) interface region, the content of Zn 2p and O 1s steadily decreased until reaching 16.5 and 11.5 at% at a thickness of 140 nm. Moreover, Cu 2p, In 3d, Ga 2p, and Se 3d belonging to the CIGSe absorber started evolving gradually in the interface area. Cu 2p, In 3d, and Se 3d increased steadily up to 16.5, 24.4, and 30.5 at% at 140 nm thickness. Nevertheless, the Ga 2p concentration varied in an extremely narrow range and was semi constant at 0.26 at% for the whole etching depth scanned. Furthermore, the elemental content of the CIGSe absorber was determined by XRF as well [83]. Thus, it had an average atomic ratio of $[Cu]/([Ga]+[In]) = 0.89$, $[Ga]/([Ga]+[In]) = 0.23$, $[In]/([Ga]+[In]) = 0.77$, and $[Se]/([Cu]+[Ga]+[In]) = 1.10$.

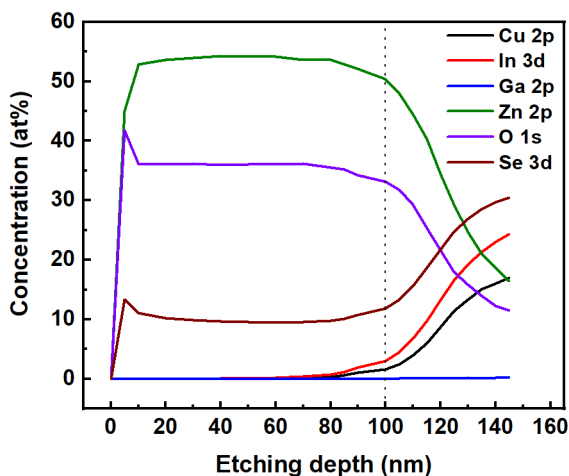


Figure 3.10. XPS depth profile analysis for a typical CIGSe/Zn(O,Se) structure showing the composition gradient of the Zn(O,Se) layer and CIGSe/Zn(O,Se) interface.

Table 3.8. Comparison of the average atomic concentrations of Zn(O,Se) layers deposited at RT measured by different techniques EDX and XPS.

Structure	Technique	atomic conc. (at%)		
		Zn	O	Se
Glass/Zn(O,Se)	EDX	50.00	36.50	13.50
CIGSe/Zn(O,Se)	XPS	52.50	36.00	11.50

Measurement uncertainty of EDX is $\pm 1.0\%$ and XPS is $\pm 10.0\%$

3.3.3 HR-SEM Analysis of CIGSe/Zn(O,Se) Devices

Figures 3.11a–c represent the cross-sectional HR-SEM micrographs of the CIGSe/Zn(O,Se) devices as a function of the thickness of the Zn(O,Se) buffer layer at 300, 200, and 100 nm. It can be seen that the CIGSe absorber surface is covered uniformly by the Zn(O,Se) buffer layer. The grown layers are homogenous and dense, with good adherence to the Mo/glass substrate and between other layers. The sputtered Mo back contact and co-evaporated CIGSe absorber layer had an average thickness of 0.3 and 1.7 μm , respectively, according to HR-SEM cross-sectional analysis, while the combined Zn(O,Se) and *i*-ZnO/ZnO:Al layers showed thicknesses of 1050, 800, and 850 nm for the 300, 200, and 100 nm thick Zn(O,Se) buffer layer, respectively (see also Figs S.3 of HR-SEM cross-sectional micrographs of the Zn(O,Se)/SLG structures in appendix 2). The thickness of the buffer layer and the top electrode is estimated as one unit altogether using HR-SEM. The thickness of the second layer associated with 200 nm thick Zn(O,Se) buffer layer is deviated by 150 nm from it is expected actual thickness. However, this deviation corresponds to the *i*-ZnO/ZnO:Al sputtering because the thickness of the *i*-ZnO/ZnO:Al layer varies based on the location of the structure inside the sputtering chamber.

3.3.4 Effect of the Zn(O,Se) Thickness on the Solar Cell Performance

Table 3.9 and Figure 3.12a represent the CIGSe solar cell parameters as a function of the thickness of the Zn(O,Se) buffer layer at 300, 200, and 100 nm. Also, a comparison of the CIGSe/Zn(O,Se) solar cells with the CIGSe/CdS reference cell is represented. The solar cell

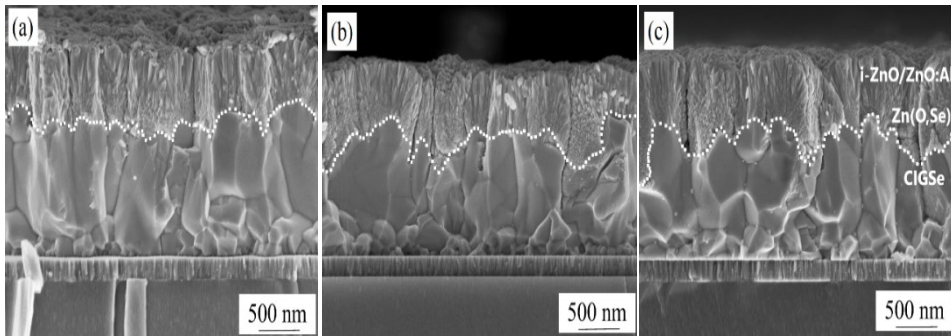


Figure 3.11. Cross-sectional HR-SEM images of the complete CIGSe/Zn(O,Se) solar cells with different thickness of the Zn(O,Se) buffer layer (a) 100 nm, (b) 200 nm, (c) 300 nm.

parameters were strongly dependent on the thickness of the Zn(O,Se) buffer layer. Hence, the J_{sc} significantly increased from 20.9 to 27.1 mA/cm² as the thickness of the Zn(O,Se) buffer layer decreased from 300 to 100 nm. This is explained by the sufficient light absorption of the CIGSe/Zn(O,Se) device with the 100 nm thickness due to high transparency (about 85%) in the visible region as shown in Fig 3.9 and the high E_g of 3.05 eV, which leads to an enhanced spectral response in EQE. The CIGSe/Zn(O,Se) device with a 100 nm thick buffer layer has an enhanced spectral response in EQE over a wide range of wavelengths (300–760 nm) compared to the devices with 200 and 300 nm thick buffer layers, which is directly reflected in the high J_{sc} values of the 100 nm thick sample. Furthermore, the low J_{sc} values for the 200 and 300 nm thick layers can be attributed to the fact that “PLD ablated materials contains macroscopic globules of molten materials” [130]; these ablated materials have a high kinetic energy and strong collision force as well. Thus, when these particulates reach the substrate, the properties of the already-deposited layers are affected and damaged. As 200 and 300 nm thick layers took a long time to deposit in the PLD chamber, the amount of damage (defects) is relatively high compared to the 100 nm thick layer. As a result, this decreases the carriers collection by impeding the photogenerated electrons [131–135]. In contrast, the FF decreased from 47.4% to 40.3% with decreasing thickness of the Zn(O,Se) buffer layer to 100 nm. This can be explained by the high series resistance (R_s) and low shunt resistance (R_{sh}) for the cells fabricated with the 100 nm thick Zn(O,Se) buffer layer as indicated in Table 3.9.

The V_{oc} values significantly increased from 395 to 454 mV as the thickness of the Zn(O,Se) buffer layer decreased from 300 to 100 nm. The recombination losses at the absorber/buffer interface are responsible for the low V_{oc} values at higher thickness [131,135]. In the thicker buffer layer, a high potential drop takes place in the buffer layer because the Fermi energy at the absorber/buffer interface moves far away from the conduction band edge [131,135]. Similarly, the potential will decrease in the whole heterostructure by the same amount as in the buffer layer, and the hole barrier will not change. In other words, the electron concentration will decrease [136], while the hole concentration will remain unchanged with increasing buffer layer thickness. Therefore, this reduces an inversion in the topmost part of the absorber layer. As a result, the recombination rate will increase through the CIGSe/Zn(O,Se) interface, resulting in a low V_{oc} [122,136–138].

The junction parameters were evaluated by fitting the $J-V$ curves of the individual solar cells using a one diode model. An ideality factor (n) and the saturation current density (J_0) were extracted and represented in Table 3.9. The theoretical view suggests

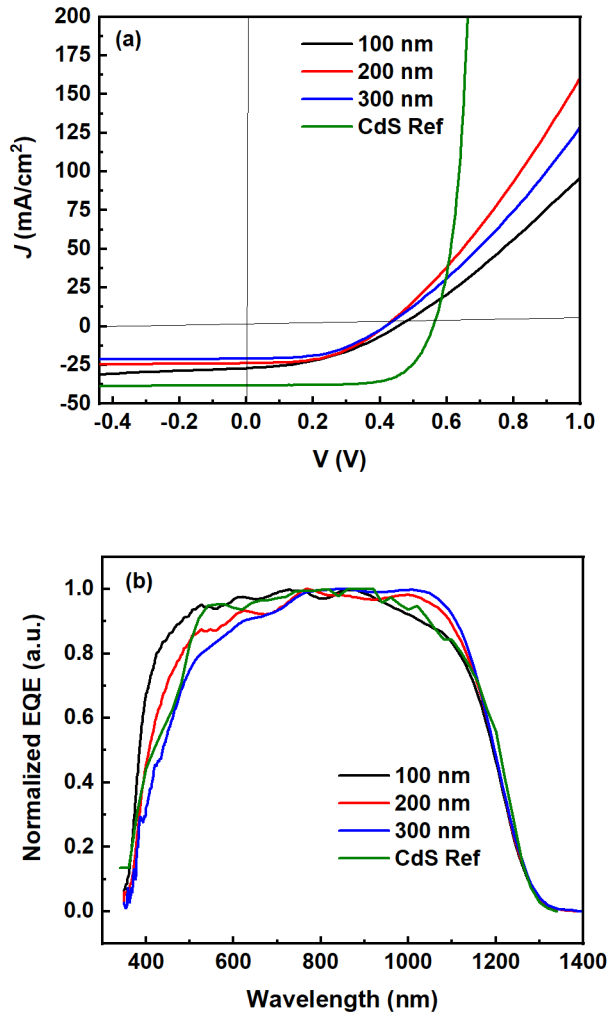


Figure 3.12. (a) J - V curves and (b) EQE spectra of the CIGSe/Zn(O,Se) devices with different thicknesses of the Zn(O,Se) buffer layer 300, 200, 100 nm, and comparison with CIGSe/CdS reference cell.

the n of the diode in a range $1 \leq n \leq 2$ is dependent on the recombination center energy and the respective capture cross sections for holes and electrons. In the case of $n > 2$, the recombination cannot be explained through a single center of recombination. A several-stage recombination process through a series of trap states deployed in space and energy can describe such a high n for a recombination process at the space-charge region [138–141]. The previous discussion clarifies that the n is heavily affected by the recombination mechanism. The ideality factor is near to but relatively higher than 2 in the case of the reference cell, which means that the space-charge region recombination is the dominant recombination mechanism in the absorber [126]. The higher fitted ideality factor values of the devices fabricated using the Zn(O,Se) buffer layer suggest that the deposition of such a layer using PLD led to additional recombination centers in the

space-charge region and recombination at the absorber/buffer interface. Furthermore, the saturation current is an estimation of the "leakage" of carriers across the p-n junction in reverse bias. This leakage is a result of the carrier recombination in the neutral regions. Thus, this means the saturation current is a measure of the recombination in a device [142,143]. A diode with a larger recombination will have a larger J_0 . The saturation current strongly affects the V_{OC} with a good agreement with the V_{OC} values in Table 3.9. The higher the J_0 corresponds to a lower V_{OC} .

The CIGSe/Zn(O,Se) device fabricated with the 100 nm thick buffer layer showed an improved spectral response in the 350–760 nm wavelength range of the EQE spectra as in Fig 3.12b. This can be explained by the relatively high transparency and high E_g of the Zn(O,Se) buffer layer with 100 nm thickness compared to the other thicknesses (200 and 300 nm), as discussed in the optical properties of the Zn(O,Se) buffer layer in section 3.3.1. However, in a very narrow wavelength range (1000–1113 nm) near the IR region, the CIGSe/Zn(O,Se) devices fabricated with 200 and 300 nm thick buffer layers showed enhanced spectral responses as in Fig 3.12b. Generally, the reduction of EQE in the IR region for TFSCs is related to several points, such as insufficient light absorption close to the CIGSe band gap, rear surface recombination, and incomplete collection of the photogenerated carriers [144–148]. The influence of these causes is identical in all three cells, but because of the high R_s of the device fabricated with a 100 nm thick buffer layer, their influence became more significant and decreased the EQE in the IR region for that specific cell. Furthermore, the E_g of the CIGSe absorber was 1.0 eV, as determined from the EQE spectra.

The solar cell parameters of the CIGSe/Zn(O,Se) devices was compared to the CIGSe/CdS reference cell (prepared and measured at Ångström Solar Center, Uppsala University), as shown in Fig 3.12a. The J_{SC} value of the CIGSe/Zn(O,Se) devices is relatively low in comparison to the reference cell. However, a significant difference in the V_{OC} and FF values was observed, confirming the presence of recombination losses and the parasitic resistance, such as high R_s and low R_{SH} , as discussed previously. Moreover, the short period of unavoidable air exposure of the CIGSe surface during transfer to the PLD deposition chamber oxidizes the Cu, In, Ga, and Se [136,149–152]. However, the ammonia in the CBD–CdS process etches the oxides, leaving a chemically clean CIGSe surface [136,149,150]. Since the ammonia etching effect is absent in the dry

Table 3.9. CIGSe solar cells parameters as a function of Zn(O,Se) buffer thickness, series and shunt resistance, saturation current, ideality factor, comparison to the reference cell using the CdS buffer layer.

Thickness (nm)	100	200	300	CdS ref *
Cell size (cm ²)	0.06	0.06	0.06	0.05
η (%)	5.0	4.5	3.9	14.7
FF (%)	40.3	47.3	47.4	68.5
V_{OC} (mV)	454.0	395.0	395.0	560.0
J_{SC} (mA/cm ²)	27.1	23.9	20.9	38.2
R_s (Ω ·cm ²)	6.0	3.1	3.5	0.2
R_{SH} (Ω ·cm ²)	81.0	139.0	242.0	1.0×10^3
J_0 (mA/cm ²)	1.8×10^{-4}	2.4×10^{-4}	2.0×10^{-4}	2.0×10^{-6}
n	3.7	3.3	3.2	2.2

* prepared and measured at Uppsala University

buffer layer deposition process, such as PLD, all residual aging products left on the CIGSe surface during the PLD deposition process stay at the absorber/buffer interface. Hence, decreasing and damaging the quality of the CIGSe/Zn(O,Se) interface, consequently, presents opportunities for recombination losses at the interface [136,153]. The combination of the PLD system with a glove box is a promising idea and can possibly prevent the CIGSe surface from oxidation and deterioration.

Figure 3.12b also, compare the EQE spectra of the CIGSe/Zn(O,Se) devices with EQE spectra of the CIGSe/CdS reference cell. The CIGSe/Zn(O,Se) devices shows an enhanced spectral response in the short wavelength region (360–550 nm) than the CIGSe/CdS reference cell. Thus, this can be explained by the high $E_g \geq 3.00$ eV of the Zn(O,Se) buffer layer compared to that of the CdS around 2.45 eV. For the rest of the wavelengths, the spectral responses of the CIGSe devices fabricated with both buffers (Zn(O,Se) or CdS) are quite similar.

Conclusions

This thesis is focused on the development and study of the Zn(O,Se) layers prepared by PLD with a systematic investigation of the effect of the deposition conditions on the structural, morphological, and optoelectronic properties of the obtained layers. In addition, the Zn(O,Se) layers prepared by PLD were applied as buffer layers in complete solar cell structures with a CIGSe absorber. The main outcomes of the thesis are:

1. Uniform, adhesive, amorphous, and polycrystalline Zn(O,Se) layers were deposited onto SLG substrates by PLD and characterized.
2. It was determined that the properties of the Zn(O,Se) layers were strongly dependent on the T_s . All layers prepared below 500°C were amorphous, and polycrystalline ternary Zn(O,Se) layers were formed at 500°C. Between 550–600°C, the formation of two different solid solutions $ZnSe_{1-y}O_y$ and $ZnO_{1-z}Se_z$ was observed where y and $z \ll 1$. This phenomenon is connected to the limited solubility of selenium and oxygen in ZnO and ZnSe, respectively, i.e., ternary Zn(O,Se) can only be formed in a relatively narrow composition range close to the binary ZnO and ZnSe.
3. All prepared Zn(O,Se) layers showed n-type conductivity with relatively high resistivity of the amorphous layers and significantly increased electrical conductivity of the polycrystalline layers.
4. Polycrystalline ternary Zn(O,Se) layers with stable composition were formed at 500°C for all applied laser fluences of 4, 5, and 6 J cm⁻². Also, a significant increase in the electrical conductivity with an increase in the laser fluence was observed.
5. UV–Vis transmittance spectra showed relatively high transparency of all deposited Zn(O,Se) layers in the visible range as a function of the T_s and laser fluences. Thus, the optical band gap of the Zn(O,Se) layers was tunable in a wide range from 2.76 to 3.29 eV depending on the T_s and the laser fluences.
6. The complete solar cell structures based on the co–evaporated CIGSe absorber and Zn(O,Se) buffer layer deposited by PLD were fabricated in the substrate configuration and characterized. It was found that the solar cells with the Zn(O,Se) buffer layer deposited at RT shows the best device performance with an average photoconversion efficiency of 5.0%. However, the solar cells with Zn(O,Se) buffer layers deposited at 100–500°C had very low device performance. The absorption capability of the CIGSe/Zn(O,Se) devices is enhanced in the blue region of the EQE spectra, which is an advantage of Zn(O,Se) compared to CdS.
7. Based on these preliminary results, we suppose that the Zn(O,Se) layers have the potential to replace the CdS buffer layer in complete solar cell structures. However, the door is still open for optimizing the complete solar cell structures based on the Zn(O,Se) buffer layer and different absorbers, optimizing PLD deposition conditions, and adjusting the conduction band offset at the absorber/buffer interface.

References

- [1] F. Blaabjerg and D. M. Ionel. Renewable Energy Devices and Systems-State-of-the-Art Technology, Research and Development, Challenges and Future Trends, Electric Power Components and Systems. 43 (2015) 1319–1328.
- [2] International Renewable Energy Agency (IRENA), Renewable Energy Technologies. Cost Analysis of Solar Photovoltaics. 1 (2012) 1–45.
- [3] Akram Abdalla. Synthesis and fabrication of hetero-structured metal oxide nanoarrays and their characterization for water splitting applications. MS thesis, KFUPM, ProQuest LLC (2016), KSA.
- [4] The energy report 2011, 100% renewable energy by 2050. <https://www.worldwildlife.org/publications/the-energy-report> (accessed 08 November 2020).
- [5] Solar industry reports 2014, global market outlook for photovoltaics 2014-2018. <https://resources.solarbusinesshub.com/solar-industry-reports/item/global-market-outlook-for-photovoltaics-2014-2018> (accessed 20 May 2018).
- [6] Taesoo D. Leea, Abasifreke U. Ebong. A review of thin film solar cell technologies and challenges. Renewable and Sustainable Energy Reviews. 70 (2017) 1286–1297.
- [7] C. Radue, E. E. van Dyk. A comparison of degradation in three amorphous silicon PV module technologies. Solar Energy Materials & Solar Cells. 94 (2010) 617–622.
- [8] Wolfram Witte, Stefanie Spiering, Dimitrios Hariskos. Substitution of the CdS buffer layer in CIGS thin film solar cells. vip-journal. 26 (2014) 23–27.
- [9] D. Hariskos, S. Spiering and M. Powalla. Buffer layers in Cu(In,Ga)Se₂ solar cells and modules. Thin Solid Films. 480–481 (2005) 99–109.
- [10] A. Politano, D. Campi, M. Cattelan, I. Ben Amara, S. Jaziri, A. Mazzotti, A. Barinov, B. Gürbulak, S. Duman, S. Agnoli, L. S. Caputi, G. Granozzi and A. Cupolillo. Indium selenide: an insight into electronic band structure and surface excitations. Scientific Report. 7 (2017) 3445.
- [11] A. Chirila, P. Reinhard, F. Pianezzi, P. Bloesch, A. R. Uhl, C. Fella, L. Kranz, D. Keller, C. Gretener, H. Hagendorfer, D. Jaeger, R. Erni, S. Nishiwaki, S. Buecheler, A. N. Tiwari. Potassium-induced surface modification of Cu(In,Ga)Se₂ thin films for high-efficiency solar cells. Nature Materials. 12 (2013) 1107–1111.
- [12] P. Jackson, D. Hariskos, E. Lotter, S. Paetel, R. Wuerz, R. Menner, W. Wischmann, M. Powalla. New world record efficiency for Cu(In,Ga)Se₂ thin-film solar cells beyond 20%. Prog. Photovolt. Res. Appl. 19 (2011) 894–897.
- [13] I. Repins, M. A. Contreras, B. Egaas, C. DeHart, J. Scharf, C. L. Perkins, B. To, R. Noufi. 19.9%-efficient ZnO/CdS/CuInGaSe₂ Solar Cell with 81.2% Fill Factor. Prog. Photovolt. Res. Appl. 16 (2008) 235–239.
- [14] Hans-Werner Schock and Rommel Noufi. CIGS-based solar cells for the next millennium. Prog. Photovolt. Res. Appl. 8 (2000) 151–160.
- [15] N. Naghavi, E. Chassaing, M. Bouttemy, G. Rocha, G. Renou, E. Leite, A. Etcheberry and D. Lincot. Electrodeposition of In₂S₃ buffer layer for Cu(In,Ga)Se₂ solar cell. Energy Procedia. 10 (2011) 155–160.
- [16] Reiner Klenk. Characterisation and modelling of chalcopyrite solar cells. Thin Solid Films. 387 (2001) 135–140.
- [17] K. M. Hynes, J. Newham. An Investigation of the Environmental Implications of the Chemical Bath Deposition of CdS through Environmental Risk Assessment. Proceedings 16th European Photovoltaic Solar Energy Conference. Glasgow, UK. 3 (2000) 2297–2300.

- [18] Kihwan Kim, Liudmila Larina, Jae Ho Yun, Kyung Hoon Yoon, Hyuk Sang Kwon and Byung Tae Ahn. Cd-free CIGS solar cells with buffer layer based on the In_2S_3 derivatives. *Phys. Chem. Chem. Phys.* 15 (2013) 9239.
- [19] Takayuki Negami, Taikan Aoyagi, Takuya Satoh, Shin-ichi Shimakawa, Shigeo Hayashi and Yasuhiro Haskimoto. Cd free CIGS solar cells fabricated by dry processes. *Conference Record of the Twenty-Ninth IEEE Photovoltaic Specialists Conference*. New Orleans, LA, USA, (2002) pp. 656–659, doi: 10.1109/PVSC.2002.1190650.
- [20] Y. M. Guo, L. P. Zhu, J. Jiang, Y. G. Li, L. Hu, H. B. Xu and Z. Z. Ye. Highly conducting and wide-band transparent F-doped $\text{Zn}_{1-x}\text{Mg}_x\text{O}$ thin films for optoelectronic applications. *Journal of Alloys and Compounds*. 602 (2014) 294–299.
- [21] N. Barreau, A. Mokrani, F. Couzinié-Devy and J. Kessler. Bandgap properties of the indium sulfide thin-films grown by co-evaporation. *Thin Solid Films*. 517 (2009) 2316–2319.
- [22] Katsumi Kushiya, Tetsuro Ni, Ichiro Sugiyama, Yasuhiko Sato, Yoshitugu Inamori and Hiroshi Takeshita. Application of Zn-compound buffer layer for polycrystalline CuInSe_2 -based thin film solar cells. *Jpn. J. Appl. Phys.* 35 (1996) 4383–4388.
- [23] Liang Wang, Deng-Bing Li, Kanghua Li, Chao Chen, Hui-Xiong Deng, Liang Gao, Yang Zhao, Fan Jiang, Luying Li, Feng Huang, Yisu He, Haisheng Song, Guangda Niu and Jiang Tang. Stable 6%-efficient Sb_2Se_3 solar cells with a ZnO buffer layer. *Nature Energy*. 2 (2017) 17046.
- [24] Sebastian S. Schmidt, Saoussen Merdes, Alexander Steigert, Reiner Klenk, Christian A. Kaufmann, Ekin Simsek Sanli, Peter A. van Aken, Mike Oertel, Anja Schneikart, Bernhard Dimmler, and Rutger Schlatmann. Interface engineering of $\text{Cu}(\text{In,Ga})\text{Se}_2$ and atomic layer deposited $\text{Zn}(\text{O,S})$ Heterojunctions. *Japanese Journal of Applied Physics*. 56 (2017) 08MC16.
- [25] Solar Frontier Achieves World Record Thin-Film Solar Cell Efficiency of 23.35%. http://www.solar-frontier.com/eng/news/2019/0117_press.html (accessed 12 October 2019).
- [26] M. Nakamura, K. Yamaguchi, Y. Kimoto, Y. Yasaki, T. Kato, H. Sugimoto. Cd-free $\text{Cu}(\text{In,Ga})(\text{Se,S})_2$ thin-film solar cell with record efficiency of 23.35%. *IEEE, J. Photovoltaics*. 9 (2019) 1863–1867.
- [27] Martin A. Green, Ewan D. Dunlop, Dean H. Levi, Jochen Hohl-Ebinger, Masahiro Yoshita, Anita W. Y. Ho-Baillie. Solar cell efficiency tables (version 54). *Prog Photovolt Res Appl*. 27 (2019) 565–575.
- [28] Martin A. Green, Ewan D. Dunlop, Jochen Hohl-Ebinger, Masahiro Yoshita, Nikos Kopidakis, Anita W.Y. Ho-Baillie. Solar cell efficiency tables (version 55). *Prog Photovolt Res Appl*. 28 (2020) 3–15.
- [29] Martin A. Green, Ewan D. Dunlop, Jochen Hohl-Ebinger, Masahiro Yoshita, Nikos Kopidaki, Xiaojing Hao. Solar cell efficiency tables (version 56). *Prog Photovolt Res Appl*. 28 (2020) 629–638.
- [30] Martin Green, Ewan Dunlop, Jochen Hohl-Ebinger, Masahiro Yoshita, Nikos Kopidakis, Xiaojing Hao. Solar cell efficiency tables (version 57). *Prog Photovolt Res Appl*. 29 (2021) 3–15.
- [31] Marie A. Mayer, Derrick T. Speaks, Kin Man Yu, Samuel S. Mao, Eugene E. Haller and Wladek Walukiewicz. Band structure engineering of $\text{ZnO}_{(1-x)}\text{Se}_x$ alloys. *Appl. Phys. Lett.* 97 (2010) 022104.

- [32] L. Kranz, C. Gretener, J. Perrenoud, R. Schmitt, F. Pianezzi, F. Mattina, P. Blösch, E. Cheah, A. Chirilă, C. M. Fella, H. Hagendorfer, T. Jäger, S. Nishiwaki, A. R. Uhl, S. Buecheler and A. N. Tiwari. Doping of polycrystalline CdTe for high-efficiency solar cells on flexible metal foil. *Nature communications*. 4 (2013) 1–7.
- [33] Nicolae Spalatu. Development of CdTe absorber layer for thin-film solar cells. PhD thesis, TalTech University, TalTech Press (2017), Estonia.
- [34] B. M. Başol, B. McCandless. Brief review of cadmium telluride-based photovoltaic technologies. *Journal of Photonics for Energy*. 4 (2014) 040996.
- [35] N. Naghavi, D. Abou-Ras, N. Allsop, N. Barreau, S. Bücheler, A. Ennaoui, C.-H. Fischer, C. Guillen, D. Hariskos, J. Herrero, R. Klenk, K. Kushiya, D. Lincot, R. Menner, T. Nakada, C. Platzer-Björkman, S. Spiering, A. N. Tiwari and T. Törndahl. Buffer layers and transparent conducting oxides for chalcopyrite $\text{Cu}(\text{In,Ga})(\text{S,Se})_2$ based thin film photovoltaics: present status and current developments. *Prog. Photovolt. Res. Appl.* 18 (2010) 411–433.
- [36] M. Turcu, O. Pakma, U. Rau. Interdependence of absorber composition and recombination mechanism in $\text{Cu}(\text{In,Ga})(\text{Se,S})_2$ heterojunction solar cells. *Appl. Phys. Lett.* 80 (2002) 2598–2600.
- [37] M. J. Furlong, M. Froment, M. C. Bernard, R. Corte's, A. N. Tiwari, M. Krejci, H. Zogg, D. Lincot. Aqueous solution epitaxy of CdS layers on CdS. *Journal of Crystal Growth*. 193 (1998) 114–122.
- [38] E. Niemi, L. Stolt. Characterization of CuInSe_2 thin films by XPS. *Surface and Interface Analysis*. 15 (1990) 422–426.
- [39] J. Lindahl, U. Zimmermann, P. Szaniawski, T. Torndahl, A. Hultqvist, P. Salome, C. Platzer-Bjorkman, M. Edoff, Inline $\text{Cu}(\text{In,Ga})\text{Se}_2$ Co-evaporation for High-Efficiency Solar Cells and Modules. *IEEE, J. Photovolt.* 3 (2013) 1100–1105.
- [40] F. Larsson, J. Keller, J. Olsson, O. Donzel-Gargand, N. M. Martin, M. Edoff, T. Törndahl. Amorphous tin-gallium oxide buffer layers in $(\text{Ag,Cu})(\text{In,Ga})\text{Se}_2$ solar cells. *Solar Energy Materials and Solar Cells*. 215 (2020) 110647.
- [41] Ramis Hertwig, Shiro Nishiwaki, Mario Ochoa, Shih-Chi Yang, Thomas Feurer, Evgeniia Gilshtein, Ayodhya N. Tiwari, and Romain Carron. ALD-ZnMgO and absorber surface modifications to substitute CdS buffer layers in co-evaporated CIGSe solar cells. *EPJ Photovoltaics*. 11 (2020) 12.
- [42] N. Naghavi, S. Spiering, M. Powalla, B. Cavana, D. Lincot, High-efficiency copper indium gallium diselenide (CIGS) solar cells with indium sulfide buffer layers deposited by atomic layer chemical vapor deposition (ALCVD). *Prog. Photovolt. Res. Appl.* 11 (2003) 437–443.
- [43] Solar Frontier Achieves World Record Thin-Film Solar Cell Efficiency of 22.9%. https://www.solar-frontier.com/eng/news/2017/1220_press.html (accessed 9 May 2018).
- [44] Peipei Xin. Alternative Buffer Layer Development in $\text{Cu}(\text{In,Ga})\text{Se}_2$ Thin Film Solar Cells. PhD dissertation, University of Delaware, ProQuest LLC (2017), USA.
- [45] Cathy Bugot, Muriel Bouttemy, Nathanaelle Schneider, Arnaud Etcheberry, Daniel Lincot, and Frédérique Donsanti. New insights on the chemistry of plasma-enhanced atomic layer deposition of indium oxysulfide thin films and their use as buffer layers in $\text{Cu}(\text{In,Ga})\text{Se}_2$ thin film solar cell. *J. Vac. Sci. Technol. A*. 36 (2018) 061510.

- [46] Soumyadeep Sinha, Dip K. Nandi, Pravin S. Pawar, Soo-Hyun Kim, Jaeyeong Heo. A review on atomic layer deposited buffer layers for Cu(In,Ga)Se₂ (CIGS) thin film solar cells: Past, present, and future. *Solar Energy*. 209 (2020) 515–537.
- [47] Wu JL, Hirai Y, Kato T, Sugimoto H, Bermudez V. New world record efficiency up to 22.9% for Cu(In,Ga)(Se,S)₂ thin-film solar cells. 7th World Conference on Photovoltaic Energy Conversion (WCPEC-7). Waikoloa, HI, USA. June 10–15, (2018).
- [48] Martin A. Green, Yoshihiro Hishikawa, Ewan D. Dunlop, Dean H. Levi, Jochen Hohl-Ebinger, Anita W.Y. Ho-Baillie. Solar cell efficiency tables (version 52). *Prog Photovolt Res Appl*. 26 (2018) 427–436.
- [49] Martin A. Green. Yoshihiro Hishikawa, Ewan D. Dunlop, Dean H. Levi, Jochen Hohl-Ebinger, Masahiro Yoshita, Anita W.Y. Ho-Baillie. Solar cell efficiency tables (version 53). *Prog Photovolt Res Appl*. 27 (2019) 3–12.
- [50] Marie A. Mayer, Derrick T. Speaks, Kin Man Yu, Samuel S. Mao, Eugene E. Haller and Wladek Walukiewicz. Band structure engineering of ZnO_(1-x)Se_(x) alloys. *Solar hydrogen and nanotechnology V*. 7770 (2010) 77700C.
- [51] Marie A. Mayer, Kin Man Yu, Eugene E. Haller and Wladek Walukiewicz. Tuning structural, electrical, and optical properties of oxide alloys: ZnO_{1-x}Se_x. *J. Appl. Phys*. 111 (2012) 113505.
- [52] Ho Nyung Lee, Hans M. Christen, Matthew F. Chisholm, Christopher M. Rouleau and Douglas H. Lowndes. Strong polarization enhancement in asymmetric three-component ferroelectric super-lattices. *Nature*. 433 (2005) 395–399.
- [53] M. Welna, M. Baranowski, W. M. Linhart, R. Kudrawiec, K. M. Yu, M. Mayer & W. Walukiewicz. Multicolor emission from intermediate band semiconductor. ZnO_{1-x}Se_x. *Scientific Reports*. 7 (2017) 44214.
- [54] A. Y. Cho, J. R. Arthur. Molecular beam epitaxy. *Prog. Solid State Chem*. 10 (1975) 157–192 doi:10.1016/0079-6786(75)90005-9.
- [55] K. Iwata, P. Fons, A. Yamada, H. Shibata, K. Matsubara, K. Nakahara, H. Takasu and S. Niki. Bandgap Engineering of ZnO Using Se. *phys. stat. sol.* 229 (2002) 887–890.
- [56] Angelika Polity, Bruno K. Meyer, Thorsten Krämer, Changzhong Wang, Ute Habocek, and Axel Hoffmann. ZnO based ternary transparent conductors. *phys. stat. sol.* 203 (2006) 2867–2872.
- [57] Marie A. Mayer, Kin Man Yu, Derrick T. Speaks, Jonathan D. Denlinger, Lothar A. Reichertz, Jeffrey W. Beeman, Eugene E. Haller, and Wladek Walukiewicz. Band Gap Engineering of Oxide Photoelectrodes: Characterization of ZnO_{1-x}Se_x. *J. Phys. Chem. C*. 116 (2012) 15281–15289.
- [58] J. H. Boyle, B. E. McCandless, W. N. Shafarman, R. W. Birkmire. Structural and optical properties of (Ag,Cu)(In,Ga)Se₂ polycrystalline thin film alloys. *J Appl Phys*. 115 (2014) 223504.
- [59] Gwo-Ching Wang, Toh-Ming Lu. RHEED Transmission Mode and Pole Figures, 1st ed., Springer, New York, (2014). doi:10.1007/978-1-4614-9287-0.
- [60] P. Capper, S.Irvine, T. Joyce. Epitaxial Crystal Growth: Methods and Materials. In: Kasap S., Capper P. (eds) *Springer Handbook of Electronic and Photonic Materials*. Springer Handbooks. Springer, Cham (2017). https://doi.org/10.1007/978-3-319-48933-9_14.
- [61] S. Valligatla, A. Chiasera, S. Varas, N. Bazzanella, D. N. Rao, G. C. Righini, M. Ferrari. High quality factor 1-D Er³⁺-activated dielectric microcavity fabricated by RF-sputtering. *Optics Express*. 20 (2012) 21214–21222.

- [62] J. E. Mahan. *Physical Vapor Deposition of Thin Film*. John Wiley & Sons, Inc. (2000) ISBN 0-471-33001-9.
- [63] RF sputtering Advantage, RF sputtering Disadvantage, 2012. <https://www.rfwireless-world.com/Terminology/Advantages-and-Disadvantages-of-RF-Sputtering.html> (accessed 05 July 2020).
- [64] Howard M. Smith and A. F. Turner. Vacuum deposited thin films using a ruby laser. *Appl. Opt.* 4 (1965) 147.
- [65] H. Schwarz and H. A. Tourtellotte. Vacuum Deposition by High-Energy Laser with Emphasis on Barium Titanate Films. *J. Vac. Sci. Technol.* 6 (1969) 373.
- [66] J. Desserre and J. F. Floy. Interaction of laser light beam pulses with complex targets: Application to production of compound thin films. *Thin Solid Films.* 29 (1975) 29.
- [67] Zaitsev-Zotov S. V, Martynyuk A. N and Protasov E. A. Superconductivity of BaPb/sub_{1-x}/Bi/sub_x/O₃ films prepared by laser evaporation method. *Sov. Phys. Solid State.* 25 (1983) 100–103.
- [68] D. Dijkkamp, T. Venkatesan, X. D. WU, S. A. Shaheen, N. Jisrawi, Y. H. Min-lee, W. L. Mclean, and M. Croft. Preparation of Y-Ba-Cu oxide superconductor thin films using pulsed laser evaporation from high Tc bulk material. *Appl. Phys. Lett.* 51 (1987) 619.
- [69] Types of lasers, Newport corporation 2021. <https://www.newport.com/n/laser-types> (accessed 03 March 2021).
- [70] R. M. Bowman, A. I. Ferguson, and C. M. Pegrum. In-situ fabrication of y-ba-cu-oxide thin films by pulsed laser deposition. *IEEE Transactions on magnetics.* 27 (1991) 1459–1462.
- [71] excimer laser. https://en.wikipedia.org/wiki/Excimer_laser (accessed 24 July 2021).
- [72] what is excimer laser. <https://www.gigaphoton.com/en/technology/laser/what-is-an-excimer-laser> (Accessed 01 August 2021).
- [73] F. J. Duarte and L. W. Hillman. *Dye Laser Principles*. In: Peter Liao and Paul Kelley (eds.) Academic, 1st edition. Elsevier, New York, (1990). Chapter 6, ISBN: 9780323139328.
- [74] C. Tallman and R. Tennant. Large-scale excimer-laser-pumped dye lasers. In: F. J. Duarte (eds) *High Power Dye Lasers*. 1st edition. Springer, Berlin, (1991) Chapter 4, <https://doi.org/10.1007/978-3-540-47385-5>.
- [75] H. Sankur, W. J. Gunning, J. DeNatale, and J. F. Flintoff. High-quality optical and epitaxial Ge films formed by laser evaporation. *J. Appl. Phys.* 65 (1989) 2475.
- [76] Douglas B. Chrisey and Graham K. Hübner. *Pulsed Laser Deposition of Thin Films*. Wiley-Interscience; 1st edition. John Wiley & Sons Inc. New York, (1994) pp. 3–11, 214, 231–235. ISBN-10: 0471592188.
- [77] Willmott P. R., Huber J. R. Pulsed laser vaporization and deposition. *Reviews of Modern Physics.* 72 (2000) 315–328.
- [78] Samuli Komulainen. *Microstructure Characterization of Pulsed Laser Deposited Metal Oxide Nanoparticles*. MS thesis, University of Oulu (2016), Finland.
- [79] Robert Eason. *Pulsed Laser Deposition of Thin Films Applications-LED Growth of Functional Materials*. Hoboken, John Wiley & Sons, Inc. New Jersey, (2007) ISBN-10: 0-471-44709-9.
- [80] D. Bäuerle. *Laser Processing and Chemistry*. Springer, (2000) pp. 210, 460–462, 468–471, 638.
- [81] M. Schilling, A. Guillaume, J. M. Scholtyssek and F. Ludwig. Design of experiments for highly reproducible pulsed laser deposition of YBa₂Cu₃O_{7-δ}. *J. Phys. D: Appl. Phys.* 47 (2014) 1–10.

- [82] VAC COAT, Pulsed laser deposition, 04 FEB 2020. <https://vaccoat.com/blog/pulsed-laser-deposition-pld/> (accessed 02 November 2020).
- [83] Louis Gouillart, Andrea Cattoni, Wei-Chao Chen, Julie Goffard, Lars Riekehr, Jan Keller, Marie Jubault, Negar Naghavi, Marika Edoff, Stéphane Collin. Interface engineering of ultrathin Cu(In,Ga)Se₂ solar cells on reflective back contacts. *Prog Photovolt Res Appl.* 29 (2020) 1–10.
- [84] G. Perna, V. Capozzi, M. C. Plantamura, A. Minafra, S. Orlando and V. Marotta. ZnSe films deposited on crystalline GaAs and amorphous quartz substrates by means of pulsed laser ablation technique. *Eur. Phys. J. B.* 29 (2002) 541–545.
- [85] A. S. Aly, A. A. Akl & H. Howari. Effect of pulsed laser power annealing on structural and optical characteristics of ZnSe thin films. *Acta Physica Polonica A.* 128 (2015) 414–418.
- [86] S. Xiao, L. Zhao, Y. Liu & J. Lian. Nanocrystalline ZnO films prepared by pulsed laser deposition and their abnormal optical properties. *Applied Surface Science.* 283 (2013) 781–787.
- [87] V. Craciun, J. Elders, J. G. E. Gardeniers & W. I. Boyd. Characteristics of high quality ZnO thin films deposited by pulsed laser Deposition. *Appl. Phys. Lett.* 65 (1994) 2963–2965.
- [88] V. Vaithianathan, B. Lee & S. Kim. Growth of phosphorus doped ZnO thin films by pulsed laser deposition. *phys. stat. sol.* 201 (2004) 2837–2840.
- [89] Y. B. Man, Z. H. Xi, S. C. Chen, M. Liu & J. Wei. XRD study on the effect of the deposition condition on pulsed laser deposition of ZnO films. *Cent. Eur. J. Phys.* 6 (2008) 643–647.
- [90] M. G. Tsoutsouva, C. N. Panagopoulou, D. Papadimitriou, I. Fasaki & M. Kompitsas. ZnO thin films prepared by pulsed laser deposition. *Materials Science and Engineering B.* 176 (2011) 480–483.
- [91] J. B. Franklin, B. Zou, P. Petrov, D. W. McComb, M. P. Ryan and M. A. McLachlan. Optimised pulsed laser deposition of ZnO thin films on transparent conducting Substrates. *J. Mater. Chem.* 21 (2011) 8178–8182.
- [92] J. N. Zeng, K. J. Low, M. Z. Ren, T. Liew & F. Y. Lu. Effect of deposition conditions on optical and electrical properties of ZnO films prepared by pulsed laser deposition. *Applied Surface Science.* 197–198 (2002) 362–367.
- [93] A. L. Patterson. The Scherrer Formula for X-Ray Particle Size Determination. *Phys. Rev.* 56 (1939) 978.
- [94] Weichang Zhou, Ruibin Liu, Dongsheng Tang, Xiaoxu Wang, Haiming Fan, Anlian Pan, Qinglin Zhang, Qiang Wan, Bingsuo Zou. Luminescence and local photonic confinement of single ZnSe:Mn nanostructure and the shape dependent lasing behavior. *Nanotechnology.* 24 (2013) 055201.
- [95] Weichang Zhou, Ruibin Liu, Dongsheng Tang & Bingsuo Zou. The effect of dopant and optical micro-cavity on the photoluminescence of Mn-doped ZnSe nanobelts. *Nanoscale Research Letters.* 8 (2013) 314.
- [96] Z. D. Hu, X. F. Duan, M. Gao, Q. Chen and L.-M. Peng. ZnSe nanobelts and nanowires synthesized by a closed space vapor transport technique. *J Phys Chem C.* 111 (2007) 2987–2991.
- [97] Qin Yang, Hua Cai, Zhigao Hu, Zhihua Duan, Xu Yang, Jian Sun, Ning Xu & Jiada Wu. Extended photoresponse and multi-band luminescence of ZnO/ZnSe core/shell nanorods. *Nanoscale Research Letters.* 9 (2014) 31.

- [98] Shen, Liming, Bao, Ningzhong, Yanagisawa, Kazumichi, Domen, Kazunari, Gupta, Arunava, Grimes, Craig A. Direct synthesis of ZnO nanoparticles by a solution-free mechanochemical reaction. *Nanotechnology*. 17 (2006) 5117–5123.
- [99] X. L. Xu, S. P. Lau, G. Y. Chen, B. K. Tay. Polycrystalline ZnO thin films on Si (100) deposited by filtered cathodic vacuum arc. *J. Cryst. Growth*. 223 (2001) 201–205.
- [100] C. Bundesmann, N. Ashkenov, M. Schubert, D. Spemann, T. Butz, E. M. Kaidashev, M. Lorenz and M. Grundmann. Raman scattering in ZnO thin films doped with Fe, Sb, Al, Ga, and Li. *Appl. Phys. Lett.* 83 (2003) 1974–1976.
- [101] A. Kaschner, U. Habocek, Martin Strassburg, Matthias Strassburg, G. Kaczmarczyk, A. Hoffmann, C. Thomsen, A. Zeuner, H. R. Alves, D. M. Hofmann, and B. K. Meyer. Nitrogen-related local vibrational modes in ZnO: N. *Appl. Phys. Lett.* 80 (2002) 1909–1911.
- [102] Min-Yeong Kim, Malenahalli Halappa Naveen, Nanjanagudu Ganesh Gurudatt and Yoon-Bo Shim. Detection of nitric oxide from living cells using polymeric zinc organic frame work-derived zinc oxide composite with conducting polymer. *Advanced science news*. 1700502 (2017) 1–10.
- [103] R. Al-Gaashani, S. Radiman, A. R. Daud, N. Tabet, Y. Al-Douri. XPS and optical studies of different morphologies of ZnO nanostructures prepared by microwave methods. *Ceramics International*. 39 (2013) 2283–2292.
- [104] D. R. Kumar, D. Manoj and J. Santhanalakshmi. Au–ZnO bullet-like heterodimer nanoparticles: synthesis and use for enhanced nonenzymatic electrochemical determination of glucose. *RSC Adv*. 4 (2014) 8943–8952.
- [105] R. Sankar Ganesh, M. Navaneethan, Ganesh Kumar Mani, S. Ponnusamy, K. Tsuchiya, C. Muthamizhchelvan, S. Kawasaki, Y. Hayakawa. Influence of Al doping on the structural, morphological, optical, and gas sensing properties of ZnO nanorods. *Journal of Alloys and Compounds*. 698 (2017) 555–564.
- [106] Fen Qiao, Rong Kang, Qichao Liang, Yongqing Cai, Jiming Bian and Xiaoya Hou. Tunability in the optical and electronic properties of ZnSe microspheres via Ag and Mn doping. *ACS Omega*. 4 (2019) 12271–12277.
- [107] S. Bera, S. Dhara, S. Velmurugan and A. K. Tyagi. Analysis on Binding Energy and Auger Parameter for Estimating Size and Stoichiometry of ZnO Nanorods. *International Journal of Spectroscopy*. 371092 (2012). doi:10.1155/2012/371092.
- [108] A. V. Naumkin, A. Kraut-Vass, S. W. Gaarenstroom, and C. J. Powell. NIST X-ray Photoelectron Spectroscopy Database. NIST Standard Reference Database 20, Version 4.1, (2012). DOI: <http://dx.doi.org/10.18434/T4T88K>.
- [109] Ronald Hesse. Unifit for Windows (Line Positions and Data Formats), version (2018), Scientific Software GmbH. Leipzig, Germany.
- [110] Sergei Bereznev, Hrachya Kocharyan, Natalia Maticiuca, Revathi Naidu, Olga Volobujeva, Andrey Tverjanovich, Julia Kois. One-stage pulsed laser deposition of conductive zinc oxysulfide layers. *Applied Surface Science*. 425 (2017) 722–727.
- [111] N. Khedmi, M. Ben Rabeha, M. Kanzari, Thickness dependent structural and optical properties of vacuum evaporated CuIn_5S_8 thin films. *Energy Procedia*. 44 (2014) 61–68.
- [112] Sönmezoglu S, Arslan A, Serin T, Serin N. The effects of film thickness on the optical properties of $\text{TiO}_2\text{-SnO}_2$ compound thin films. *Physica Scripta*. 84 (2011) 065602–065607.
- [113] M. G. Varnamkhasti, H. R. Fallah, M. Mostajaboddavati, A. Hassanzadeh. Influence of Ag thickness on electrical, optical and structural properties of nanocrystalline $\text{MoO}_3/\text{Ag}/\text{ITO}$ multilayer for optoelectronic applications. *Vacuum*. 86 (2012) 1318–1322.

- [114] J. Tauc. Optical Properties and Electronic Structure of Amorphous Ge and Si. *Mat. Res. Bull.* 3 (1968) 37–46.
- [115] J. Tauc, R. Grigorovic and A. Vancu. Optical Properties and Electronic Structure of Amorphous Germanium. *phys. stat. sol.* 15 (1966) 627.
- [116] R. Bensaha and H. Bensouyad. Synthesis, characterization and properties of zirconium oxide (ZrO₂)-doped titanium oxide (TiO₂) thin films obtained via sol-gel process. In: Czervinski, F. (eds) *Heat Treatment—Conventional and Novel Applications*. IntechOpen, (2012), chapter 10, 207–234. doi: 10.5772/51155.
- [117] Svetlana Polivtseva, Nicolae Spalatu, Akram Abdalla, Olga Volobujeva, Jaan Hiie and Sergei Bereznev. Pulsed laser deposition of Zn(O,Se) layers for optoelectronic application. *ACS Appl. Energy Mater.* 1 (2018) 6505–6512.
- [118] Y. Natsume, H. Sakata. Zinc oxide films prepared by sol-gel spin-coating. *Thin Solid Films.* 372 (2000) 30–36.
- [119] Wai-Keat Lee, Hin-Yong Wong, Kah-Yoong Chan, Yong Thian-Khok, Seong-Shan Yap, Teck-Yong Tou. Effects of laser fluence on the structural properties of pulsed laser deposited ruthenium thin films. *Appl. Phys. A.* 100 (2010) 561–568.
- [120] W. Shan, W. Walukiewicz, J. W. Ager III, K. M. Yu, J. Wu, E. E. Haller, Y. Nabetani, T. Mukawa, Y. Ito, T. Matsumoto. Effect of oxygen on the electronic band structure in ZnO_xSe_{1-x} alloys. *Appl. Phys. Lett.* 83 (2003) 299.
- [121] Ashraf Hassan Farha, Ali Oguz Er, Yuksel Ufuktepe, Hani E. Elsayed-Ali. Laser-fluence effects on NbN_x thin films fabricated by pulsed laser deposition. *Mater. Chem. Phys.* 132 (2012) 667–672.
- [122] Xianwu Xiu, Zhiyong Pang, Maoshui Lv, Ying Dai, Lina Ye, Shenghao Han. Transparent conducting molybdenum-doped zinc oxide films deposited by RF magnetron sputtering. *Appl. Surf. Sci.* 253 (2007) 3345–3348.
- [123] Stanford R. Ovshinsky & David Adler. Local structure, bonding, and electronic properties of covalent amorphous semiconductors. *Contemp. Phys.* 19 (2006) 109–126.
- [124] H. El-Zahed, M. Dongol and M. Radwan. Annealing and thickness effect on the optical absorption of Ge₂₀Te₈₀ and Cu₆Ge₁₄Te₈₀ films. *Eur. Phys. J. AP.* 17 (2002) 179–186.
- [125] W. Shan, W. Walukiewicz, J. Wu, K. M. Yu, J. W. Ager III, S. X. Li, E. E. Haller, J. F. Geisz, D. J. Friedman and S. R. Kurtz. Band-gap bowing effects in B_xGa_{1-x}As alloys. *J. Appl. Phys.* 93 (2003) 2696–2699.
- [126] K. Alberi, J. Wu, W. Walukiewicz, K. M. Yu, O. D. Dubon, S. P. Watkins, C. X. Wang, X. Liu, Y. J. Cho and J. Furdyna. Valence-band anticrossing in mismatched III-V semiconductor alloys. *Phys. Rev. B.* 75 (2007) 045203.
- [127] Akram Abdalla, Sergei Bereznev, Nicolae Spalatu, Olga Volobujeva, Natalja Sleptsuk, Mati Danilson. Pulsed laser deposition of Zn(O,Se) layers in nitrogen background Pressure. *Sci. Rep.* 9 (2019) 1–9.
- [128] Elvira Fortunato, Alexandra Goncalves, Vitor Assunc̃ao, Ant´onio Marques, Hugo ´Aguas, Luis Pereira, Isabel Ferreira, Rodrigo Martins. Growth of ZnO:Ga thin films at room temperature on polymeric substrates: thickness dependence. *Thin Solid Films* 442 (2003) 121–126.
- [129] Marie Annette Mayer. Band structure engineering for solar energy applications: ZnO_{1-x}Se_x films and devices. PhD dissertation, University of California, Berkeley (2012), USA.
- [130] Geoff Martin and Al Mottola. Intensified CCDs Investigate Oplasma Plumes, 01 July 2000. <https://www.laserfocusworld.com/detectors-imaging/article/16555580/intensified-ccds-investigate-Oplasma-plumes> (Accessed 24 November 2020).

- [131] Helena Wilhelm, Hans-Werner Schock, Scheer Roland. Interface recombination in heterojunction solar cells: influence of buffer layer thickness. *J. Appl. Phys.* 109 (2011) 084514.
- [132] Chang-Soo Lee, Suncheul Kim, Young-Min Shin, Byung Guk Park, Byung Tae Ahn, HyukSang Kwon. Performance improvement in Cd-free Cu(In,Ga)Se₂ solar cells by modifying the electronic structure of the ZnMgO buffer layer. *RSC Adv.* 4 (2014) 36784.
- [133] Johan Lindahl, Jan Keller, Olivier Donzel-Gargand, Piotr Szaniawski, Marika Edoff, Tobias Törndahl. Deposition temperature induced conduction band changes in zinc tin oxide buffer layers for Cu(In,Ga)Se₂ solar cells. *Solar Energy Materials & Solar Cells.* 144 (2016) 684–690.
- [134] M. Gloeckler and J. R. Sites. Efficiency limitations for wide-band-gap chalcopyrite solar cells. *Thin Solid Films.* 480–481 (2005) 241–245.
- [135] M. Turcu, U. Rau, Fermi level pinning at CdS/Cu(In,Ga)(Se,S)₂ interfaces: effect of chalcopyrite alloy composition. *J. Phys. Chem. Solid.* 64 (2003) 1591–1595.
- [136] J. Lindahl, J. T. Wätjen, A. Hultqvist, T. Ericson, M. Edoff, T. Törndahl. The effect of Zn_{1-x}Sn_xO_y buffer layer thickness in 18.0% efficient Cd-free Cu(In,Ga)Se₂ solar cells. *Prog Photovolt Res Appl.* 21 (2013) 1588–1597.
- [137] Y. M. Guo, L. P. Zhu, J. Jiang, Y. G. Li, L. Hu, H. B. Xu, Z. Z. Ye. Highly conducting and wide-band transparent F-doped Zn_{1-x}Mg_xO thin films for optoelectronic applications. *J. Alloys Compd.* 602 (2014) 294–299.
- [138] Jan Keller, Francis Chalvet, Jonathan Joel, Asim Aijaz, Tomas Kubart, Lars Riekehr, Marika Edoff, Lars Stolt, Tobias Törndahl. Effect of KF absorber treatment on the functionality of different transparent conductive oxide layers in CIGSe solar cells. *Prog Photovolt Res Appl.* 26 (2018) 13–23.
- [139] M. Nardone, V. G. Karpov, D. Shvydka, M. L. C. Attygale. Theory of electronic transport in noncrystalline junctions. *J. Appl. Phys.* 106 (2009) 074503.
- [140] U. Rau, M. Schmidt, A. Jasenek, G. Hanna, H. W. Schock. Electrical characterization of Cu(In,Ga)Se₂ thin-film solar cells and the role of defects for the device performance. *Solar Energy Materials & Solar Cells.* 67 (2001) 137–143.
- [141] Juan Sun, Venkatram Nalla, Mai Nguyen, Yi Ren, Sing Yang Chiam, Yue Wang, Kong Fai Tai, Handong Sun, Nikolay Zheludev, Sudip K. Batabyal, Lydia H. Wong. Effect of Zn(O,S) buffer layer thickness on charge carrier relaxation dynamics of CuInSe₂ solar cell. *Solar Energy.* 115 (2015) 396–404.
- [142] Jan Keller, Oleksandr V. Bilousov, Erik Wallin, Olle Lundberg, Janet Neerken, Stephan Heise, Lars Riekehr, Marika Edoff, and Charlotte Platzer-Björkman. Effect of Cu Content on Post-Sulfurization of Cu(In,Ga)Se₂ Films and Corresponding Solar Cell Performance. *Phys. Status Solidi A.* 216 (2019) 1900472.
- [143] Viktor V. Brus, Christopher M. Proctor, Niva A. Ran, and Thuc-Quyen Nguyen. Capacitance Spectroscopy for Quantifying Recombination Losses in Nonfullerene Small-Molecule Bulk Heterojunction Solar Cells. *Adv. Energy Mater.* 6 (2016) 1502250.
- [144] Steven S. Hegedus, William N. Shafarman. Thin-film solar cells: device measurements and analysis. *Prog. Photovoltaics Res. Appl.* 12 (2004) 155–176.
- [145] Christiana Honsberg, Stuart Bowden. Quantum efficiency, Photovoltaics Education 2019. <https://www.pveducation.org/pvcdrom/solar-cell-operation/quantum-efficiency> (Accessed 14 March 2021).

- [146] Louis Gouillart, Wei-Chao Chen, Andrea Cattoni, Julie Goffard, Lars Riekehr, Jan Keller, Marie Jubault, Negar Naghavi, Marika Edoff, and Stéphane Collin. Reflective Back Contacts for Ultrathin Cu(In,Ga)Se₂-Based Solar Cells. *IEEE Journal of Photovoltaics*. 10 (2020) 250–254.
- [147] Jan Keller, Oleksandr V. Bilousov, Janet Neerken, Erik Wallin, Natalia M. Martin, Lars Riekehr, Marika Edoff, and Charlotte Platzer-Björkman. Heavy Alkali Treatment of Post Sulfurized Cu(In,Ga)Se₂ Layers: Effect on Absorber Properties and Solar Cell Performance. *Sol. RRL*. 4 (2020) 2000248.
- [148] Prasert Sinsersuksakul, Leizhi Sun, Sang Woon Lee, Helen Hejin Park, Sang Bok Kim, Chuanxi Yang, and Roy G. Gordon. Overcoming Efficiency Limitations of SnS-Based Solar Cells. *Adv. Energy Mater.* 4 (2014) 1400496.
- [149] J. Kessler, K.O. Velthaus, M. Ruckh, R. Laichinger, H. W. Schock, D. Lincot, R. Ortega, J. Vedel. Chemical bath deposition of CdS on CuInSe₂, etching effects and growth kinetics. *Proceedings of the 6th International Photovoltaic Science and Engineering Conference*. New Delhi, India, (1992) pp. 1005–1010.
- [150] J. Kessler, K. O. Velthaus, M. Ruckh, R. Laichinger, H. W. Schock, D. Lincot, R. Ortega, J. Vedel. Chemical bath deposition of CdS on CuInSe₂: combining dry and wet processes for high efficiency thin film solar cells. *Proceedings of the 11th European Photovoltaics Solar Energy Conference*. Montreux, Switzerland, (1992) pp. 870–873.
- [151] Max Hilaire Wolter, Benjamin Bissig, Enrico Avancini, Romain Carron, Stephan Buecheler, Philip Jackson, and Susanne Siebentritt. Influence of Sodium and Rubidium Postdeposition Treatment on the Quasi-Fermi Level Splitting of Cu(In,Ga)Se₂ Thin Films. *IEEE Journal of Photovoltaics*. 8 (2018) 1320–1325.
- [152] Ye-Chan Kim, Ho-Jung Jeong, Jin-Yong Kim, Jae-Hyung Jang. The effect of partial electrolyte treatment on the properties of Cu(In,Ga)Se₂ solar cell. *Thin Solid Films* 638 (2017) 396–399.
- [153] Jan Keller, Kostiantyn V. Sopiha, Olof Stolt, Lars Stolt, Clas Persson, Jonathan J. S. Scragg, Tobias Törndahl, Marika Edoff. Wide-gap (Ag,Cu)(In,Ga)Se₂ solar cells with different buffer materials—A path to a better heterojunction. *Prog Photovolt Res Appl*. 28 (2020) 1–14.

Acknowledgments

I would like to thank my great creator almighty Allah for granting me life, strength, power, health, patience, and science to complete my study.

Also, I would like to express my deepest appreciation to my thesis supervisor Dr. Sergei Bereznev for his trust, guides, unconditional support, friendly discussion, and continuous encouragement during the study.

I extend my gratitude to the department director prof. Malle Krunk, Heads of the doctoral school prof. Andres Öpik and Prof. Ilona Oja Acik for giving me opportunity to join the Department of Materials and Environmental Technology and presume my doctoral study.

I am thankful to Prof. Maarja Grossberg the Head of the Laboratory of Optoelectronic Materials Physics for allowing me to actively use the laboratory facilities and continuous support.

My profound appreciation to Dr. Valdek Mikli, Dr. Olga Volobujeva, Dr. Souhaib Oueslati, Dr. Mati Danlison, Dr. Erki Kärber, Dr. Nicolae Spalatu, Dr. Reelika Kaupmees for their support and useful discussions.

Also, I am grateful to Dr. Jan Keller from Uppsala University for collaborative work, and fruitful discussions.

My gratitude also goes to my colleagues and all the people I have worked with within our department, who make the learning environment friendly.

This research was supported by the institutional research funding IUT19–28 of the Estonian Ministry of Education and Research, TalTech base finance project B54, PUT1495 Project of the Estonian Ministry of Education and Research, and the European Union through the European Regional Development Fund project “Center of Excellence” TK141, “Advanced materials and high–technology devices for sustainable energetics, sensorics, and nanoelectronics”. Further, partially supported by ASTRA “TUT Institutional Development Programme for 2016–2022” Graduate school of Functional Materials and Technologies (2014–2020.4.01.16–0032). Also, partially by the Archimedes foundation through the Dora Plus scholarship platform.

I would like to express my warmest gratitude to my family for their continuous support and motivation.

Abstract

Pulsed Laser Deposition of Zn(O,Se) Layers for Optoelectronic Applications

TFSCs are one of the most promising sources of renewable energy. They consist of different functional layers, such as the absorber layer, buffer layer, front and back contacts, etc. Usually, the buffer layer should be an n-type semiconductor with a wide band gap and appropriate electrical properties. Also, the buffer layer should have a minimal defect density at the absorber/buffer interface in a complete TFSCs structure. An implementation of an intermediate buffer layer between the p-type absorber layer and the front contact can improve the photovoltaic properties of the rectifying junctions significantly. For example, implementing a buffer layer reduces the interfacial charge recombination by accelerating an electron–hole pairs separation.

CdS is a well-known or standard buffer layer used in TFSCs with different absorbers, which allows the highest recorded efficiencies of these devices to be obtained. In these devices, CdS is usually prepared by the wet CBD method. Despite the high performance of CdS, there is a current trend to substitute CdS with other materials due to some drawbacks, such as a parasitic light absorption that leads to optical losses in the wavelength range of 350–550 nm and the environmental impact due to the toxicity of Cd. Thus, a number of buffer layers were investigated, such as zinc and indium based buffer layers, as an alternative for CdS. Recently, a Zn(O,S) buffer layer combined with a Cu(In,Ga)(Se,S)₂ absorber has achieved the highest recorded photoconversion efficiency of 23.35%.

To follow this prospective approach, in this thesis, we proposed and investigated the properties of Zn(O,Se) layers as an alternative buffer layer for the conventional toxic CdS in optoelectronic devices. Zn(O,Se) layers were deposited by the PLD technique using a target prepared from hot-pressed premixed fine powders of ZnO = 75 at% and ZnSe = 25 at%. The effect of the T_s and the effect of the laser fluences on the structural, optical, and electrical properties of the Zn(O,Se) layers were systematically studied using different techniques, such as XRD, Raman, XPS, HR-SEM, EDX, UV–Vis, and Hall effect measurements. Also, the Zn(O,Se) was applied as a buffer layer in complete TFSCs structures of the substrate configuration with the CIGSe absorber. The PV parameters of the CIGSe/Zn(O,Se) solar cells were analyzed by measuring the *J–V* curves and EQE spectra.

For the effect of the T_s on the properties of the Zn(O,Se) layers deposited by PLD in nitrogen back-pressure, the structural investigation showed that all Zn(O,Se) layers grown at RT–400°C were amorphous, while a polycrystalline ternary Zn(O,Se) phase formed at 500°C. However, at the T_s of 550–600°C, two different solid solutions were formed as ZnSe_{1-y}O_y and ZnO_{1-z}Se_z due to the limited solubility of O and Se in ZnSe and ZnO, respectively. The thickness of the Zn(O,Se) layers monotonically decreased from 733 nm to 459 nm with increasing T_s from RT to 600°C. The UV–Vis spectra showed a relatively high transmittance around 80% in the visible part of the spectrum for the deposited Zn(O,Se) layers with thicknesses of 647–454 nm. Furthermore, with increasing T_s, the absorption edges shifted to a shorter wavelength region, and the optical band gap varied from 2.76 to 3.29 eV. The 50 mTorr of nitrogen back-pressure effectively maintained stable ratios of the elemental content of the deposited layers in the whole range of the T_s. The Hall effect measurements revealed the n-type conductivity of the

Zn(O,Se) layers, further showing that all Zn(O,Se) layers deposited below 500°C were relatively highly resistive. However, the electrical conductivity of the Zn(O,Se) layers deposited at 500–600°C increased significantly.

For the effect of the laser fluences on the properties of the Zn(O,Se) layers deposited at 500°C, the XRD analysis showed the formation of the polycrystalline ternary Zn(O,Se) for all three laser fluences. The crystallite sizes and the layer thickness increased from 34 to 42 nm and from 340 to 445 nm, respectively, with increasing laser fluences from 4 to 6 J cm⁻². The UV–Vis transmittance spectra showed relatively high transparency of Zn(O,Se) layers around 80% for all applied laser fluences. Moreover, by increasing the laser fluences, the absorption edges shifted to a longer wavelength and the optical band gap gradually decreased from 3.03 to 2.87 eV. The Hall effect measurements revealed the n-type conductivity of all deposited Zn(O,Se) layers. The carrier concentration increased to 4 x 10¹⁵ cm⁻³ with an increase in the laser fluence to 6 J cm⁻².

The application of Zn(O,Se) as a buffer layer in combination with a CIGSe absorber was successful; however, the obtained photoconversion efficiency of 5.0% is less than the photoconversion efficiency (14.7%) of the reference cell using a CdS buffer layer. It was found that the performance of the solar cells was dependent on the thickness of the amorphous Zn(O,Se) buffer layer. Thus, the open circuit voltage, short circuit current, and photoconversion efficiency were increased significantly to 454 mV, 27.1 mA/cm², and 5.0%, respectively, by decreasing the thickness of the amorphous Zn(O,Se) buffer layer to 100 nm. Furthermore, the parasitic absorption of the CIGSe/Zn(O,Se) devices in the blue region was reduced in comparison with the CIGSe/CdS reference cell due to the high optical band gap ≥ 3.0 eV of the amorphous Zn(O,Se) buffer layers. On the basis of the preliminary results of these Cd-free solar cells, we suppose that Zn(O,Se) has the potential to replace CdS in solar cells. Thus, follow-up optimization of the deposition conditions and also the selenium-to-oxygen ratios in Zn(O,Se) seems to be a prospective way to improve the performance of the Zn(O,Se) buffer layer in optoelectronic devices.

Lühikokkuvõte

Impulsslaser-sadestatud Zn(O,Se) kiled optoelektronseteks rakendusteks

Mitme erineva funktsionaalsusega kihist koosnevad õhukesekilelised päikeseelemendid on kõige lootustandvamad taastuenergia allikad. Õhukesekihilised päikeseelemendid koosnevad päikesevalgust neelavast kihist, puhverkihist, kontaktkihtidest ja valgust tagasipeegeldavast kihist. Tavapäraselt kasutatakse puhverkihina laia keelutsooniga ning sobivate elektriliste ja optiliste omadustega n-tüüpi pooljuhtmaterjali. Lisaks peab puhverkiht sobituma valgust neelava absorberkihi struktuursete omadustega, et viia miinimumini kontaktpinna defektide kontsentratsioon. Puhverkihi kasutamine absorberkihi ja läbipaistva aknakihi vahel võimaldab tunduvalt parandada päikeseelemendi töövõimet. Näiteks kiirendab puhverkihi kasutamine elektronide ja aukude eemaldumist üksteisest, seega vähendab laengukandjate rekombinatsiooni kontakthalal.

Kõige tuntum puhverkihina kasutatav materjal on CdS, mida kasutatakse paljudes õhukesekilelistes päikeseelementides koos erinevate absorbermaterjalidega. Õhukesekileliste päikeseelementide rekordkasutegurid on saavutatud just CdS-puhverkihiga. Päikeseelementides kasutatav CdS-puhverkiht sadestatakse tavaliselt keemilise vanni meetodil. Vaatamata sellele, et CdS on väga hea puhvermaterjal ja suurepärase optoelektronsete omadustega, on CdS kasutamisel ka puudusi. Nimelt neelab ka CdS valgust põhjustades optilist kadu 350–550 nm lainepikkustel, lisaks on Cd vees lahustuvad ühendid mürgised. Seetõttu võivad CdS sadestusel tekkivad jääklahused avaldada mõju keskkonnale. Seetõttu on uus suund asendada CdS teiste materjalidega, nagu näiteks erinevate tsingil ning indiumil põhinevate puhverkihtidega. Viimased tulemused näitavad, et päikeseelement Zn(O,S) puhverkihi ning Cu(In,Ga)(Se,S)₂ valgust neelava kihiga on saavutanud 23.35 %-lise kasuteguri.

Tuginedes neile lootustandvatele tulemustele kasvatati antud doktoritöö raames Zn(O,Se) kui alternatiivse puhvermaterjali kilesid ning uuriti nende kilede omadusi. Zn(O,Se) kiled sadestati impulsslaser-sadestuse meetodil kasutades sihtmärki, mis on valmistatud kuumalt pressitud eelsegatud peenest pulbrist, mille oli ZnO-i 75 mol% ja ZnSe-i 25 mol%. Süstemaatiliselt uuriti sadestustemperatuuri (T_s) ning laserkiirguse impulsi energiatiheduse mõju Zn(O,Se) kilede struktuurilistele, optilistele ning elektrilistele omadustele, kasutades järgnevaid meetodeid: röntgendifraktsiooni (XRD), Raman spektroskoopiat, röntgenfotoelektron-spektroskoopiat (XPS), kõrgelahutusega skaneerivat elektronmikroskoopiat (HRSEM), energiadiispersiivset röntgenmikroanalüüsi (EDX), UV-Vis spektroskoopiat ning Halli efekti mõõtmisi. Lisaks kasutati Zn(O,Se) puhverkihina Cu(In,Ga)Se₂ (CIGSe) valgust neelava kihiga õhukesekilelistes päikeseelementides. CIGSe/Zn(O,Se) päikeseelementide parameetrite analüüsiks kasutati voolu-pinge kõveraid ning kvantefektiivsuse (EQE) mõõtmisi.

Esimesena uuriti sadestustemperatuuri mõju lämmastiku vasturõhu tingimustes sadestatud Zn(O,Se) kilede kristallstruktuurile. Kõik toatemperatuuri ning 400°C vahel sadestatud Zn(O,Se) kiled olid amorfseid, kuid alates 500°C temperatuurist moodustus polükristalne kolmikühend Zn(O,Se). Samas tekkisid temperatuuride vahemikus $T_s = 550^\circ\text{C}$ kuni $T_s = 600^\circ\text{C}$ erineva koostisega tahked lahused ZnSe_{1-y}O_y ja ZnO_{1-z}Se_z. Erinevad koostised tekkisid vähenenud O ja Se lahustuvuse tõttu vastavalt ZnSe-s ja ZnO-s. Zn(O,Se) kile paksus vähenes ühtlaselt 733-lt 459 nm-ni temperatuuri tõustes

toatemperatuurilt 600°C-ni. UV–Vis spektroskoopia näitas Zn(O,Se) kilede suhteliselt kõrget läbilaskvust (umbes 80 %, kile paksus 647–454 nm) nähtavas piirkonnas. Lisaks sellele nihkus sadestustemperatuuri T_s tõustes neeldumispää lühikeste lainepikkuste piirkonda. Optilise keelutsooni laius muutus 2.76 eV ja 3.29 eV vahel. Lämmastiku vasturõhk 50 mTorr hoidis ühtlast vahekorda kilede elementaarses keemilises koostises kogu T_s piirkonnas. Halli mõõtmised näitasid, et Zn(O,Se) kiled olid n-tüüpi juhtivusega ning lisaks kõik kiled, mis olid kasvatatud temperatuuridel alla 500°C olid suhteliselt kõrge takistusega. Samas temperatuuridel $T_s = 500\text{--}600^\circ\text{C}$ sadestatud Zn(O,Se) kilede elektrijuhtivus tõusis märkimisväärselt.

Järgmisena uuriti laserkiirguse impulsi energiatiheduse mõju Zn(O,Se) kilede omadustele. XRD analüüs näitas, et temperatuuril $T_s = 500^\circ\text{C}$ kavatud kiledel tekkis kõigi kolme kasutatud laserkiirguse impulsi energiatiheduse puhul polükristalne kolmikühend Zn(O,Se). Laserkiirguse suurenedes 4-lt 6 J cm⁻²-ni suurenesid kristallitide suurus 34-lt 42 nm-ni ning kile paksus 340-lt 445 nm-ni. UV–Vis spektroskoopia näitas Zn(O,Se) kilede suhteliselt kõrget läbilaskvust (umbes 80 %) kõikide kasutatud laseri impulsi energiatiheduse väärtuste puhul. Lisaks sellele nihkus laserkiirguse suurenedes neeldumispää pikematele lainepikkustele, keelutsooni laius aga vähenes järk-järgult 3.03-lt 2.87 eV-ni. Halli mõõtmised näitasid n-tüüpi juhtivust kõikides erineva laserkiirgusimpulsi energiatihedusega sadestatud kiledes, sealjuures 6 J cm⁻² juures tõusis laengukandjate tihedus 4×10^{15} cm⁻³-ni.

Rakendades Zn(O,Se)-d puhverkihina koos valgust neelava kihiga CIGSe andis edukaid tulemusi, oli siiski saadud 5.0%-ne kasutegur väiksem võrreldes CdS puhverkihti kasutava päikeseelemendi 14.7%-st kasutegurist. Leiti, et päikeseelementide tootlikus sõltus amorfse Zn(O,Se) puhverkihi paksusest. Amorfse Zn(O,Se) puhverkihi paksuse vähenedes 100 nm-ni suurenesid märgatavalt avatud ahela pinge, lühisvool ning päikeseelemendi kasutegur vastavalt 454 mV-ni, 27.1 mA/cm²-ni ning 5.0 %-ni. Peale selle vähenes sinises spektriosas optiline kadu CIGSe/Zn(O,Se) päikeseelemendis võrreldes CIGSe/CdS päikeseelemendiga, kuna amorfne Zn(O,Se) puhverkiht on kõrge keelutsooni laiusega ≥ 3.0 eV. Cd vaba päikeseelemendi esmaseste mõõtmistulemuste põhjal oletame, et Zn(O,Se) puhverkiht näitab potentsiaali asendada tavapärasest CdS puhverkihti. Saadud tulemused näitavad, et kasvatustingimuste ning seleeni ja hapniku osakaalu optimeerimine Zn(O,Se) kiledes on perspektiivne viis parandada Zn(O,Se) puhverkihi omadusi optoelektronsetes seadmetes.

Appendix 1

Publication I

Akram Abdalla, Sergei Bereznev, Nicolae Spalatu, Olga Volobujeva, Natalja Sleptsuk and Mati Danilson. Pulsed laser deposition of Zn(O,Se) layers in nitrogen background Pressure. *Scientific Reports*. 2019, 9: 17443.

OPEN

Pulsed laser deposition of Zn(O,Se) layers in nitrogen background Pressure

Akram Abdalla^{1*}, Sergei Bereznev¹, Nicolae Spalatu¹, Olga Volobujeva¹, Natalja Sleptsuk² & Mati Danilson¹

Zinc oxy-selenide Zn(O,Se) is a novel material, that can replace the toxic CdS buffer layer in thin film solar cells and other optoelectronic devices. In this paper a systematic study of the structural, optical and electrical properties of Zn(O,Se) layers, grown by pulsed laser deposition under 50 mTorr of nitrogen background pressure, over a wide range of the substrate temperature, from RT to 600 °C, is reported. XRD, Raman, HR-SEM, XPS, UV-Vis techniques and Hall effect measurements have been used to investigate the structural, and optoelectronic properties of Zn(O,Se) layers. XRD analysis revealed that the polycrystalline ternary Zn(O,Se) phase formed at 500 °C. Raman analysis confirmed the formation of the polycrystalline Zn(O,Se) phase at 500 °C and an amorphous phase at substrate temperatures below 500 °C. Similarly, XPS analysis accompanied with the modified Auger parameters confirmed formation of ternary Zn(O,Se) layer at 500 °C as well. HR-SEM investigation showed the growth of homogenous, dense and adherent films onto a glass substrate. Furthermore, optical studies revealed that all prepared films are practically transparent in the visible region of the spectrum, with a band gap around 3 eV. Hall effect measurements revealed that conductivity, and electron concentration, increased by four orders of magnitude at 600 °C. It was found, that nitrogen background pressure maintained stable ratios of elemental contents in the whole range of the substrate temperature for Zn(O,Se) layers.

An urgent global need for sustainable energy resources has opened a multi-disciplinary research area towards potential clean energy resources, such as solar cells and hydrogen generation¹, as renewable energy sources. With respect to solar cells, particularly in high efficiency thin film solar cells such as CdTe and CIGS, a thin layer of CdS is used as a standard buffer layer which has, up to now, achieved a power conversion efficiency of 12.6%, 22.1% and 23.35% for CZTS^{2,3}, CdTe^{2,4} and CIGS^{2,5} solar cells respectively. On the other hand, CdS is a toxic material having parasitic absorption in the 350–550 nm range, which decrease the efficiency of the device^{6–8}. To address this issue, significant attention has been devoted to replacing the CdS buffer layer. Thus, synthesis of new, wide band gap, buffer material, with optimized optical and electrical properties, to overcome the CdS limitations, is required. As a result, different materials have been tested and reported such as Zn(O,OH)_x/Zn(O,S,OH)_x⁹, Zn_{1-x}Mg_xO^{10,11}, ZnS/ZnSe¹², indium sulfide/indium selenide^{13,14} and ZnO¹⁵.

Zinc oxy-selenide is an excellent candidate for the substitution of the CdS buffer layer in thin film solar cell structure due to its non-toxic, earth abundant and tuneable wide band gap character¹⁶. On the other hand, there is limited information available about the structural, optical and electrical properties of this material. Zn(O,Se) layers can be prepared by different methods such as pulsed laser deposition (PLD)¹⁶, radio frequency (RF) sputtering¹⁷ and molecular beam epitaxy (MBE)¹⁸. Among them, PLD is one of the most promising techniques for the stoichiometric deposition of complex-oxide heterostructures, super-lattices, and well-controlled interfaces¹⁹. High quality, uniform and adherent layers can be deposited by PLD.

Recently, band gap grading, via incorporation of selenium in the CdTe absorber has improved the overall cell efficiency^{8,20–22}. For instance, CdSe, used as partner buffer layer for CdTe solar cells, instead of CdS, improved cell performance and recorded a power conversion efficiency of 14% with low open-circuit-voltage (Voc) and fill factor (FF), but high short circuit current (Jsc)^{8,23}. It was demonstrated that during the cell processing, CdSe diffused into CdTe, converting itself from photo-inactive CdSe to photo-active, low band gap, CdTe_{1-x}Se_x^{23,24} with the successful removal of the undesired CdSe sub-layer. In other words, this approach extended photon collection to a

¹School of Engineering, Department of Materials and Environmental Technology, Tallinn University of Technology, Ehitajate tee 5, Tallinn, 19086, Estonia. ²TJS Department of Electronics, Tallinn University of Technology, Ehitajate tee 5, Tallinn, 19086, Estonia. *email: akrami.abdalla@gmail.com

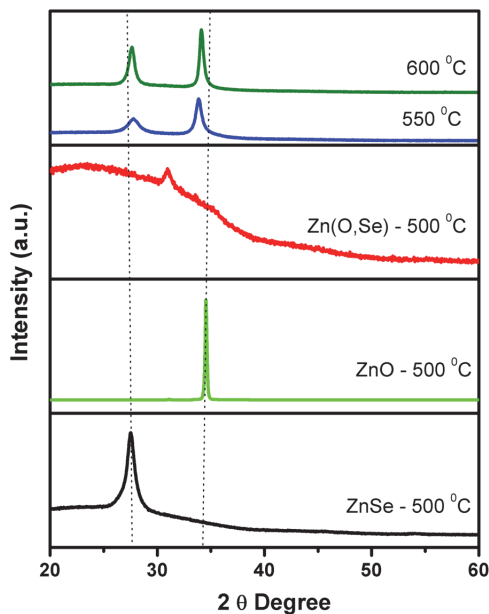


Figure 1. XRD patterns of the Zn(O,Se) films deposited in the substrate temperature region of 500–600 °C under nitrogen back-pressure.

longer wavelength, reduced losses in short wavelength and increased the carrier lifetime so giving excellent device performance^{22,25}. With regards to this, in previous work¹⁶, ternary Zn(O,Se) thin film was deposited by PLD in high vacuum. Its structural, optical and electrical properties were investigated and Zn(O,Se) layers were applied, for the first time, as a buffer layer, with CdTe absorber in a superstrate structure which yielded a reasonable power conversion efficiency of 7.6%¹⁶. It was also found that the crystal structure of Zn(O,Se) film only formed at 500 °C, and all structures deposited below this growth temperature were amorphous. Herein, this view is extended to control the composition contents and to develop the crystal structure of Zn(O,Se) layers by depositing it in nitrogen background pressure instead of high vacuum. For composition control, the nitrogen back-pressure reduce the mean free path and kinetic energy of the ablated particles. Which it has an impact of retaining the ablated particles and prevent their evaporation from the substrate surface. In case of crystal structure, the nitrogen partial pressure effects the lattice parameters of the films which will be reflected in the crystal structure^{26,27}.

The aim of this work was the deposition of Zn(O,Se) thin films by PLD under nitrogen back-pressure and different substrate temperatures (Ts), with the study of the structural and optoelectronic properties of the prepared Zn(O,Se) layers. Special attention was paid to the comparison between Zn(O,Se) layers deposited in high vacuum and under nitrogen back-pressure.

Results and Discussions

According to XRD results all Zn(O,Se) layers deposited below 500 °C were amorphous (see Supplementary Fig. S1). Figure 1 represents the XRD patterns of the Zn(O,Se) layers deposited at the substrate temperature from 500 to 600 °C combined with the XRD patterns of pure phases of ZnO and ZnSe layers deposited at 500 °C for comparison. The ZnO layer showed an XRD peak at 34.53°. In the literature, this peak is assigned to (002) plane of the ZnO wurtzite structure^{28–34}, while the ZnSe layer exhibited an XRD peak at 27.47° which is well indexed to (111) plane of ZnSe cubic phase^{35,36}. Zn(O,Se) film, grown at 500 °C, showed only one diffraction peak at 30.94° together with a residual amorphous hump, attributed to the formation of an oriented polycrystalline Zn(O,Se) phase mixed with an amorphous phase. The diffraction peak located at approximately 30.94° has been shown, in the literature, as corresponding to (002) plane $\text{ZnO}_{1-x}\text{Se}_x$ in which the x values varied from 0 to 0.12¹. As the substrate temperature was increased to 550 °C the diffractogram showed two distinct peaks at 27.70° and 34.09° indicating to the formation of different solid solutions. These peaks cannot be assigned to pure phases of ZnO and ZnSe as their diffractograms showed reflections at different 2θ values/positions. Considering the solubility of oxygen in ZnSe and selenium in ZnO, the XRD peak located at 27.7° and 30.09° can be attributed to the formation of $\text{ZnSe}_{(1-y)}\text{O}_y$ and $\text{ZnO}_{(1-z)}\text{Se}_z$ solid solutions, where y and z < 1 indicates the low solubility of O and Se in ZnSe and ZnO, respectively. With increasing the substrate temperature to 600 °C, both peaks shift towards 2θ values of ZnO and ZnSe pure phases, indicating to further decrease of Se and O solubility in ZnO and ZnSe, correspondingly.

Ts, (°C)	Crystallite sizes (nm) ^a	Elemental ratios (at%) ^b			Film Thickness (nm)	Band gap (eV)
		Zn	O	Se		
500	12.60 ± 0.8	50	39	11	454	3.00
550	13.40 ± 0.13	50	37	13	484	2.90, 3.28
600	20.50 ± 0.9	50	37	13	459	3.16, 3.29

Table 1. The crystallite sizes, elemental contents, film thicknesses and band gap values (E_g) of the Zn(O,Se) films deposited at 500–600 °C under nitrogen back-pressure. The error bars in ^arepresent standard deviation (s.d.). ^bMeasurement error of EDX is ±0.5.

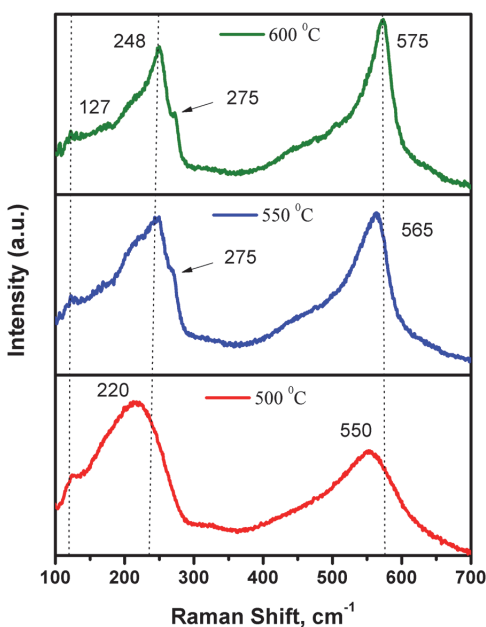


Figure 2. Raman spectra of the Zn(O,Se) films deposited in the substrate temperature region of 500–600 °C under nitrogen back-pressure.

Furthermore, an observable increase in both XRD peak intensities has been noticed with increasing the substrate temperature from 500 to 600 °C, and this behaviour is attributed to an increase in the crystallite size (see Table 1). The Scherrer formula (1) was used to calculate the crystallite size D ³⁷.

$$D = \frac{0.94\lambda}{\beta \cos\theta} \quad (1)$$

where λ is wavelength of X-ray radiation (1.5406 Å), θ is the Bragg angle and β is the full width at the half maximum (FWHM) of the peak located in the 2θ at 30.94–34.09° range in radians.

The crystallite sizes of Zn(O,Se) films deposited at 500–600 °C is calculated from the peak located at 30.94–34.09° and summarized in Table 1. The crystallite sizes increased with the increase of the substrate temperature. In comparison with PLD deposited Zn(O,Se) films in high vacuum¹⁶, the crystallite sizes decreased for the similar growth temperature interval. This can be due to an effect of the nitrogen background pressure. The nitrogen background pressure increases the nucleation sites because of the increased reaction of the ablated particles at the surface²⁷. Therefore, the surface diffusion length of atoms is decreased. In addition, the kinetic energy of the ablated species is decreased by increasing the number of collisions between the ablated species in the gas phase. As a result, the crystallite size decreases²⁷.

RT Raman spectroscopy has also been used for further structural characterization of the deposited layers. Figure 2 displays the Raman spectra of Zn(O,Se) films deposited at 500–600 °C. All Zn(O,Se) layers deposited at 100–600 °C exhibited a weak band of Raman scattering located at 127 cm^{-1} which corresponds to Zn(O,Se) phase (see Supplementary Fig. S2 for the substrate temperature range 100–400 °C). In addition, Zn(O,Se) films, deposited in the temperature range from 100 to 500 °C, exhibited two strong broad bands located at 220 cm^{-1} and 550 cm^{-1} , which correspond to the formation of Zn(O,Se) phase (amorphous in the range 100–400 °C). However, for Zn(O,Se)

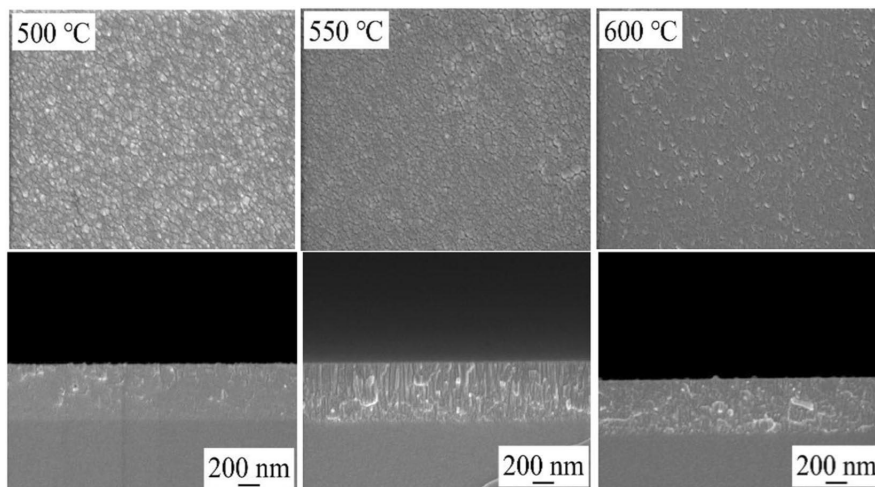


Figure 3. HR-SEM images and cross-sectional views of the Zn(O,Se) films deposited in the substrate temperature region of 500–600 °C under nitrogen back-pressure.

films deposited at 550 and 600 °C, an observable shift in both peaks position, to 248 cm^{-1} and (565/575 cm^{-1}), can be seen, which originate from longitudinal optical (LO) phonon modes of ZnSe^{17,38–41} and longitudinal optical (LO) phonon E_1 symmetry mode of ZnO^{17,42–44} respectively. These shifts in both Raman bands confirmed that ternary Zn(O,Se) polycrystalline phase formed at 500 °C, shifted towards formation of ZnSe(1-y)Oy/ZnO(1-z)Sez solid solutions, due to the decrease of O solubility in ZnSe and vice versa at 550/600 °C substrate temperature.

Besides those Raman bands, extra weak peaks started appearing, from 550 °C, located at 275 cm^{-1} . This additional Raman scattering is attributed to the intrinsic host lattice defects, such as oxygen and selenium vacancies, or Zn interstitials, which become activated with high substrate temperatures 550 and 600 °C⁴⁵.

Figure 3 represents surface and cross-sectional SEM images of Zn(O,Se) films deposited at 500–600 °C. Homogenous, dense, and well-adherent to the glass substrate surface, the films have been grown over the entire substrate temperature range. Moreover, with increasing the substrate temperature from RT to 500 °C the grain size of the films increased, with an average grain size between 15–86 nm, and from 550 °C and above, the grain size showed a decreasing tendency. Furthermore, as can be seen from the cross-sectional views in Fig. 3 and (Supplementary Fig. S3), the thickness of the deposited films decreased with increasing substrate temperature from 733 nm for the film deposited at RT to 454 nm for the film deposited at 500 °C, see Table 1 and (Supplementary Table S1). A similar trend has been observed in previous work of PLD Zn(O,Se) films deposited in high vacuum¹⁶, and was explained by the formation of a denser, compact and highly ordered polycrystalline structure, with the increase of substrate temperature.

Table 1 shows the atomic ratios of the elements in Zn(O,Se) films deposited at 500–600 °C (see Supplementary Table S1, for the temperature range RT – 400 °C). This shows stable ratios of the elemental contents in the whole substrate temperature range, accompanied with minor differences in the oxygen and selenium contents with changing the substrate temperature. When compared to PLD deposited Zn(O,Se) films in high vacuum¹⁶, the PLD deposited Zn(O,Se) films in nitrogen background pressure maintained stable elemental contents, particularly for Se content, in the whole range of the substrate temperature. This can be attributed to the positive effect of nitrogen background pressure which prevents evaporation of Se before the nucleation stage.

High-resolution XPS was used to quantitatively analyse the surface chemical composition and to identify the possible phases of each species of the Zn(O,Se) layers deposited at 500–600 °C. XPS analysis has been conducted for all Zn(O,Se) samples 500–600 °C after surface cleaning with argon (Ar^+) sputtering for 30s. Figure 4 shows the XPS spectra of C 1s, Zn 2p, O 1s, and Se 3d of Zn(O,Se) layers deposited at 500 °C. The XPS analysis revealed that the samples consisted of Zn, O, and Se, and no impurities were found. Specifically, Fig. 4a shows the binding energy for the adventitious C 1s peak at 284.6 eV which was considered for charge corrections, moreover, those two peaks appeared in C 1s spectrum positioned at 284.30 eV and 297.25 eV are attributed to Se Auger peaks. Figure 4b shows the Zn 2p XPS core-level spectrum of the sample deposited at 500 °C. Only one set of doublet was used to fit Zn 2p spectrum. None of fitting parameters, FWHM, area, nor doublet separation, were fixed. The spectra show features at 1021.23 eV and 1044.55 eV corresponding to Zn2p_{3/2} and Zn2p_{1/2}, respectively. The spin-orbit splitting of 23.32 eV between the peaks is in a good agreement with the value for Zn²⁺ oxidation state^{46–49}. For O 1s two peaks of different forms of oxygen were fitted Fig. 4c. The first oxygen peak is positioned at the lower binding energy of 529.86 eV, and is assigned to O ions in the Zn–O bonding of the Zn(O,Se) layers^{46–49}. The second peak located at 531.29 eV is related to OH group absorbed onto the surface of the Zn(O,Se) layers⁴⁷. The Se 3d region shown in Fig. 4d displays two sets of doublets, first main peak centered at 53.74 eV binding energy and the other at 54.53 eV. Each doublet comprises two peaks due to the spin-orbit splitting of the Se 3d

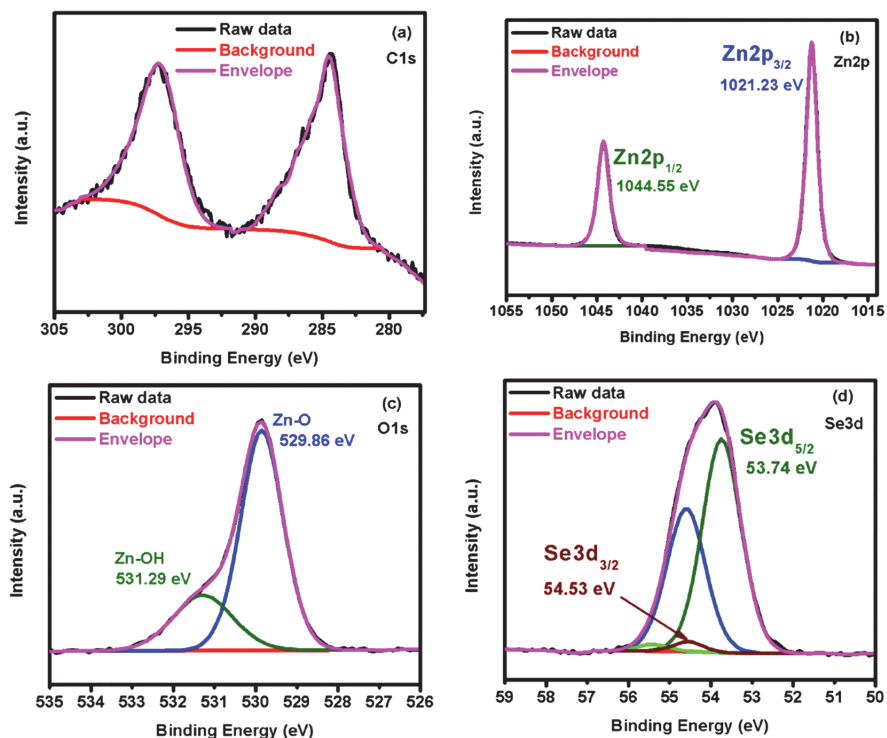


Figure 4. XPS spectrum of the Zn(O,Se) layers deposited at 500 °C under nitrogen back-pressure: (a) C 1s, (b) Zn 2p, (c) O 1s and (d) Se 3d.

Samples	Zn2p _{3/2} /Se3d _{5/2}	L ₃ M ₄₅ M ₄₅	m-AP	Refs.
	peak position eV	Kinetic energy eV	α'	
ZnO	1022.10	987.70	2009.80	⁵⁰
ZnO	1021.60	988.80	2010.40	⁵¹
ZnSe	1022.00	989.50	2011.50	⁵⁰
Zn(O,Se), Zn2p	1021.23	989.30	2010.50	This work
SeO ₂	58.80	1301.60	1360.40	⁵⁰
Zn(O,Se), Se3d	53.74	1306.58	1360.32	This work

Table 2. Binding energy and modified Auger parameters (m-AP) for Zn(O,Se) layers deposited at 500 °C under nitrogen back-pressure. Measurement error of XPS are (Binding energy ± 0.02 eV, for quantification ± 10%).

level, which are assigned to Se 3d_{5/2} and Se 3d_{3/2} of Zn-Se bonding⁵⁰. The trend is similar for Zn(O,Se) layers deposited at 550 and 600 °C except minor shifts in binding energy, due to the formation of different solid solution of ZnSe(1-y)Oy and ZnO(1-z)Sez (see Supplementary Figs. S5 and S6). The elemental ratios of Zn(O,Se) layers were determined also on the basis of XPS surface analysis. Significant increase in Zn contents was observed with the increase in substrate temperature from 500 °C to 550/600 °C from 52 at% to 57 at%, while remarkable decrease was found for oxygen contents in similar temperature interval. Regardless, the selenium contents remain stable for the substrate temperature range 500–600 °C (see Supplementary Table S2). The modified Auger parameters (m-AP) α' for Zn(O,Se) layers were calculated from the experimental binding energies of the Zn 2p_{3/2} and Se 3d_{5/2} photoelectron peaks and kinetic energies of Zn L₃M₄₅M₄₅ and Se L₃M₄₅M₄₅ Auger peak values⁵¹ of standard pure ZnO, ZnSe, SeO₂ phases and Zn(O,Se) layers deposited at 500 °C are presented in Table 2. By considering Wanger plot^{52,53} and data presented in Table 2, we compared peak positions, kinetic energies and m-APs (α') of Zn(O,Se) layers with standard values for pure ZnO, ZnSe and SeO₂ phases^{51–53}. Thus, the calculated three parameters of Zn(O,Se) layers are different from those standard values, which mean different compound has been formed, i.e.

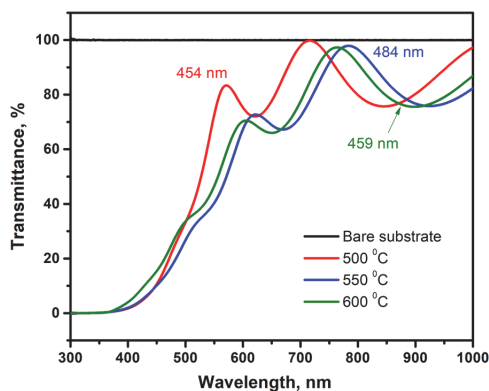


Figure 5. Transmittance spectra of bare substrate and Zn(O,Se) films deposited in the substrate temperature region of 500–600 °C under nitrogen back-pressure with their corresponding films thickness.

Ts, °C	Hall coefficient (cm ³ /C) ^a	Resistivity (Ω cm) ^a	Concentration (cm ⁻³) ^a	Mobility (cm ² /Vs) ^a
500	-2.4 × 10 ⁷	2.1 × 10 ⁵	3.0 × 10 ¹¹	113.0
550	-6.0 × 10 ⁶	2.3 × 10 ⁵	1.0 × 10 ¹²	26.2
600	-2.0 × 10 ²	5.4 × 10 ¹	3.4 × 10 ¹⁶	3.4

Table 3. The electrical parameters of the Zn(O,Se) films deposited in the temperature region of 500–600 °C under nitrogen back-pressure. ^aMeasurement errors of Hall effect measurement is ±5.0.

ternary Zn(O,Se) compound has been formed at 500 °C. In addition, core-level peak positions, Auger peak kinetic energies and m-APs (α') of Zn(O,Se) layers deposited at 550/600 °C are different from that of Zn(O,Se) layers deposited at 500 °C (see Supplementary Tables S2), which mean formation of the solid solutions of ZnSe(1- γ)Oy/ZnO(1- z)Sez in a good agreement with XRD and Raman results.

Figure 5 shows the optical transmittance spectra of Zn(O,Se) films deposited at 500–600 °C (see Supplementary Fig. S7 for the temperature range RT – 400 °C). All the produced films exhibited transparency of around 80% in the visible region of the spectra, except films produced at RT and 100 °C, which showed less than 80%. With increasing substrate temperature, the absorption edges shifted to a lower wavelength (blue shift). The optical band gaps of all Zn(O,Se) films were evaluated based on the Tauc relation (2)^{7,54} by plotting $h\nu$ versus $(\alpha h\nu)^2$ and extrapolating the linear part of the plot to $h\nu$ axis (x axis) (see Supplementary Fig. S8).

$$(\alpha h\nu) = A(h\nu - E_g)^n \quad (2)$$

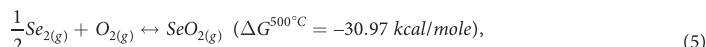
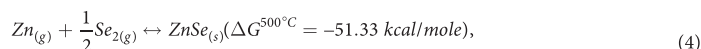
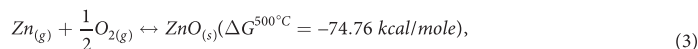
where α is absorption coefficient and estimated from $\alpha = 2.303 \log(T/d)$, T is the transmittance, d is the film thickness, E_g is the band gap, $h\nu$ is the photon energy, eV is the unit for band gaps and exponent n depends on transition type ($n = 1/2$ for direct allowed).

The calculated band gaps of Zn(O,Se) films fluctuated with the substrate temperature from 2.76 eV for RT to 3.29 eV for 600 °C see Table 1 and (Supplementary Table S1 for Zn(O,Se) films deposited at RT – 400 °C). This fluctuation in the band gaps can be attributed to the variation in film thickness and shifting in the absorption edges with the substrate temperature. In addition, the films deposited at 550 and 600 °C showed two different band gaps ~2.98 and ~3.28 eV which is in excellent agreement with the XRD results which showed two diffraction peaks corresponding to a shift of Zn(O,Se) phase toward formation of ZnSe(1- γ)Oy/ZnO(1- z)Sez solid solutions, as in XRD at 550/600 °C.

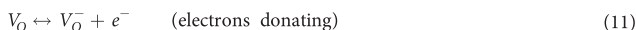
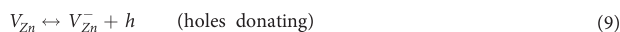
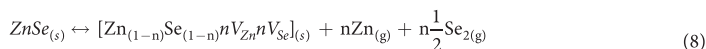
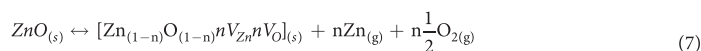
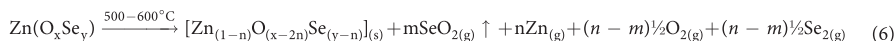
Table 3 shows the Hall effect measurements of Zn(O,Se) films deposited at 500–600 °C. All the films deposited below 500 °C showed very high dark resistivity, which was associated to their amorphous, semi-insulating, behaviour. The sign of the Hall coefficient has revealed that the electrons are the majority carriers in the PLD deposited Zn(O,Se) films, under nitrogen background pressure, which corresponds to the n-type conductivity of the films.

The films deposited at 500 °C were characterized as having high resistivity of 10⁵ Ω-cm, electron concentration of ~ 10¹¹ cm⁻³ and a mobility of 113.0 cm²/V.s. By increasing the substrate temperature to 550 °C, the electron concentration increased by nearly one order of magnitude, from 10¹¹ to 10¹² cm⁻³, while the mobility was significantly reduced, up to 26.2 cm²/V.s. A further increase of the substrate temperature to 600 °C sharply increased the electron concentration by approximately four orders of magnitude (~10¹⁶ cm⁻³) and dramatically reduced the mobility to 3.4 cm²/V.s. The changes in the electrical properties of Zn(O,Se) films, grown under nitrogen background pressure, can be explained based on the same thermodynamic considerations from a previous study¹⁶.

Therein, the Gibbs energies of the formation for ZnSe, ZnO and SeO₂ in the temperature interval of 500–600 °C were analysed, as follows:



These thermodynamically favoured reactions indicate that the ZnO and ZnSe are the most stable phases in the Zn(O,Se) and together, with the formation of SeO₂, generate conditions for increased partial pressure of oxygen and selenium above ZnO and ZnSe and hence the creation of a Zn-rich composition in the Zn(O,Se) vapour phase. This fact leads to an increase in the overall concentration of oxygen and selenium vacancies (n-type intrinsic defects), and consequently enhances the electron concentration in Zn(O,Se) films. As the electron concentration increased, with increasing substrate temperature, the Hall mobility decreased systematically (Table 3). This behaviour is explained by the scattering of carriers, through ionized oxygen/selenium vacancy defects with high concentrations, at elevated temperatures. The formation of Frenkel defects and the equilibrium constant in the Zn(O,Se) system are given below^{16,55}.



$K_{(\text{ZnO})} = [V_{\text{Zn}}^-] \cdot [V_{\text{O}}^-]$, where $K_{(\text{ZnO})}$ is the equilibrium constant for ZnO.

$K_{(\text{ZnSe})} = [V_{\text{Zn}}^-] \cdot [V_{\text{Se}}^-]$, where $K_{(\text{ZnSe})}$ is the equilibrium constant for ZnSe.

Thus, all these equations, and the aforementioned considerations, are valid for Zn(O,Se) films deposited under nitrogen atmosphere, and the background pressure only serves to inhibit the transport of the material, through the gas phase to the substrate, by reducing the mean free path and kinetic energy of the ablated particles. The latter phenomenon (i.e., reduced mean free path) has an impact of retaining the Se content in Zn(O,Se) system (EDX analysis showed constant Se concentration in the entire temperature interval).

Compared to previous work¹⁶, the electron concentration in the Zn(O,Se) films grown at 500–600 °C, in high vacuum, is significantly higher than the electron concentration in Zn(O,Se) films deposited at the same temperatures, but under nitrogen pressure, although for both growth conditions the trend is the same. Considering the relatively stable Se concentration (according to EDX) the reduced electron concentration can be explained as being due to slightly increased partial pressure of Se (in the form of SeO₂) in the Zn(O,Se) system. According to Eq. (5) the higher the concentration of Se in the solid phase is, the higher the partial pressure of SeO₂ above Zn(O,Se) and the lower the concentration of Se vacancies. The increased partial pressure of Se will also have an impact on ZnO (due to solubility of Se in ZnO) by reducing the concentration of oxygen vacancies. Under these conditions, the reduced concentrations of selenium and oxygen vacancies lowers the electron concentration in Zn(O,Se) grown under nitrogen atmosphere. The XRD results showed two diffraction peaks with an increase in the substrate temperature to 550 and 600 °C. This fact indicates, that at these temperatures, the solubility of oxygen in ZnSe, selenium in ZnO (i.e., ZnSe has low solubility in ZnO and vice versa) and solubility of SeO₂ from the solid phase are significantly reduced and ZnSe and ZnO does not form a homogenous Zn(O,Se) solid solution. Thus, the changes in the electrical properties correlate well with XRD and SEM/EDX results.

In summary, homogenous, adherent and polycrystalline Zn(O,Se) layers have been deposited by PLD under 50 mTorr of nitrogen background pressure. All Zn(O,Se) layers deposited in the substrate temperature range RT–400 °C were amorphous, and a conductive polycrystalline Zn(O,Se) phase was formed at 500 °C. Optical investigation confirmed that all films are practically transparent in the visible range of the spectrum with band gap value around 3 eV. It was found, that the nitrogen partial pressure had a dramatic influence on the defect structure of the deposited layers and maintained stable ratios of the elemental contents, over the whole substrate temperature range, in comparison with PLD of Zn(O,Se) films in high vacuum.

Methods

Deposition of Zn(O,Se) structure. Zn(O,Se) layers were deposited onto glass substrates by PLD under nitrogen background pressure in the temperature range from RT to 600 °C. Soda lime glass substrates, 3.6×3.6 cm in size, were prepared and ultrasonically cleaned for 15 min in 20% solution of Decon 90 and deionized water at 50 °C respectively. The substrates were dried under filtered air flow, then exposed to Nova Scan Digital UV-Ozone cleaning system for 15 min. (ZnO:ZnSe) of 25.4 mm dia. \times 6 mm thick targets for PLD were prepared by hot-pressing of pre-mixed fine powders of ZnO (75 at %) and ZnSe (25 at %) (99.99% purity, Testbourne Ltd). The deposition was performed by Neocera Pioneer 120 PLD system equipped with 248 nm KrF excimer laser (Coherent Compex Pro 102 F). The target to substrate distance was 9 cm¹⁶. The background pressure in the vacuum chamber was 50 mTorr at a constant flow rate of nitrogen of 9 standard cubic centimeter (Scm). For all substrate temperatures, similar deposition conditions were applied as follows: (40000 laser pulses, 200 mJ pulse energy, 10 Hz repetition rate), the laser beam was focused on \sim 5 mm² spot on the surface of (ZnO:ZnSe) target. For comparison, pure phases of ZnO and ZnSe layers were also deposited by PLD at 500 °C. The substrate was rotated during the deposition process for uniform distribution of the ablated materials onto the substrate, and the target was rotating and rastering to avoid local heating of the target and uniform consumption of the materials.

Characterization. The phase composition of the prepared Zn(O,Se) films was characterized by X-ray diffraction (XRD) and Raman spectroscopy. XRD analyses were conducted in the Bragg - Brentano (θ - 2θ) geometry using a Rigaku Ultima IV diffractometer with Cu K α radiation. Crystallite size was evaluated using the software PDXL Version 1.4.0.3 on the Rigaku system. Raman measurements were performed by a Horiba's LabRam HR800 spectrometer, equipped with 532 nm green laser with a spot size of \sim 5 μ m. Optical transmittance spectra were measured in the wavelength range of 300–1000 nm by means of Shimadzu UV-1800, UV-Vis spectrophotometer. Film thickness and morphology were characterized by means of high-resolution scanning electron microscope (HR-SEM) Zeiss Merlin equipped with In-Lens SE detector for topographic imaging. Elemental analysis was conducted using Energy Dispersive X-ray (EDX) system (Bruker EDX-XFlash6/30 detector)⁷. XPS measurements were performed with a Kratos Axis Ultra DLD XPS spectrometer with monochromatic Al K α radiation (1486.6 eV). The pass energy for the high-resolution scan was kept at 20 eV. Scans were acquired with steps of 100 meV. A charge neutraliser system was switched on during acquisitions. The spectrometer was calibrated to give Au 4f_{7/2} metallic gold binding energy of 83.98 eV and the spectrometer dispersion is adjusted to give a binding energy of 932.68 eV for metallic Cu 2p_{3/2}. The binding energy for the adventitious C 1s peak at 284.6 eV was considered for charge corrections. Mini Beam I Ar⁺ ion source was operated at 2 keV and 10 mA for 30 s to sputter clean the samples surface as they were exposed to the atmospheric conditions.

Hall measurements were performed by the Van Der Pauw method at room temperature using Ecopia HMS-3000 system. The gold spring probes were placed at the corners of the sample symmetrically. A constant current passed through the electrodes and an applied magnetic field was 0.55 T. Hall effect parameters, such as charge carrier's mobility, concentration, Hall coefficient and resistivity were calculated.

Data availability

All data generated or analysed during this study are included in this published article (and its Supplementary Information files).

Received: 20 April 2019; Accepted: 30 October 2019;

Published online: 25 November 2019

References

- Mayer, M. *et al.* Band structure engineering of ZnO_(1-x)Se_x alloys. *Appl. Phys. Lett.* **97**, 022104, <https://doi.org/10.1063/1.3464323> (2010).
- Green, M. A. *et al.* Solar cell efficiency tables (version 54). *Prog Photovolt Res Appl* **27**, 565–575, <https://doi.org/10.1002/pip.3171> (2019).
- Wang, W. *et al.* Device characteristics of CZTSSe thin-film solar cells with 12.6% efficiency. *Adv. Energy Mater.* **4**, 1301465, <https://doi.org/10.1002/aenm.201301465> (2014).
- First solar press release. First solar achieves yet another cell conversion efficiency world record, 24 February 2016 (<https://www.solarpowerworldonline.com/2016/02/24939/>).
- Solar frontier achieves world record thin-film solar cell efficiency of 23.35% (http://www.solar-frontier.com/eng/news/2019/0117_press.html).
- Kim, K. *et al.* Cd-free CIGS solar cells with buffer layer based on the In₂S₃ derivatives. *Phys. Chem. Chem. Phys.* **15**, 9239, <https://doi.org/10.1039/c3cp50324k> (2013).
- Bereznev, S. *et al.* One-stage pulsed laser deposition of conductive zinc oxysulfide layers. *Applied Surface Science.* **425**, 722–727, <https://doi.org/10.1016/j.apsusc.2017.07.078> (2017).
- Baines, T. *et al.* Incorporation of CdSe layers into CdTe thin film solar cells. *Sol. Energy Mater. Sol. Cells.* **180**, 196–204, <https://doi.org/10.1016/j.solmat.2018.03.010> (2018).
- Kushiya, K. *et al.* Application of Zn-compound buffer layer for polycrystalline CuInSe₂-based thin film solar cells. *Jpn. J. Appl. Phys.* **35**, 4383–4388, <https://doi.org/10.1143/JJAP.35.4383/pdf> (1996).
- Negami, T. *et al.* Cd free CIGS solar cells fabricated by dry processes. *IEEE*. 656–659, <https://ieeexplore.ieee.org/stamp/stamp.jsp?tp=&arnumber=1190650> (2002).
- Guo, Y. *et al.* Highly conducting and wide-band transparent F-doped Zn_{1-x}Mg_xO thin films for optoelectronic applications. *Journal of Alloys and Compounds.* **602**, 294–299, <https://doi.org/10.1016/j.jallcom.2014.02.181> (2014).
- Hariskos, D., Spiering, S. & Powalla, M. Buffer layers in Cu(In,Ga)Se₂ solar cells and modules. *Thin Solid Films.* **480–481**, 99–109, <https://doi.org/10.1016/j.tsf.2004.11.118> (2005).
- Barreau, N., Mokrani, A., Couzinié-Devy, F. & Kessler, J. Bandgap properties of the indium sulfide thin-films grown by co-evaporation. *Thin Solid Films.* **517**(7), 2316–2319, <https://doi.org/10.1016/j.tsf.2008.11.001> (2009).

14. Politano, A. *et al.* Indium selenide: an insight into electronic band structure and surface excitations. *Scientific Report*. **7**, 3445, <https://doi.org/10.1038/s41598-017-03186-x> (2017).
15. Wang, L. *et al.* Stable 6%-efficient Sb₂Se₃ solar cells with a ZnO buffer layer. *Nature Energy*. **2**, 17046 <https://www.nature.com/articles/nenergy201746> (2017).
16. Polivtseva, S. *et al.* Pulsed laser deposition of Zn(O,Se) layers for optoelectronic application. *ACS Appl. Energy Mater.* **1**, 6505–6512, <https://doi.org/10.1021/acsaem.8b01431> (2018).
17. Angelika Polity, A. *et al.* ZnO based ternary transparent conductors. *phys. stat. sol.* **203**, 2867–2872, <https://doi.org/10.1002/pssa.200669570> (2006).
18. Iwata, K. *et al.* Bandgap Engineering of ZnO Using Se. *phys. stat. sol.* **229**, 887–890, 0370-1972/02/22902-0887 \$ 17.50p.50/0 (2002).
19. Nyung, H., Christen, H., Chisholm, M., Rouleau, C. & Lowndes, D. Strong polarization enhancement in asymmetric three-component ferroelectric super-lattices. *Nature*. **433**, 395, <https://doi.org/10.1038/nature03261> (2005).
20. Wu, S. *et al.* High-efficiency Cu₂ZnSn(S,Se)₄ solar cells fabricated through a low-cost solution process and a two-step heat treatment. *Prog. Photovolt: Res. Appl.* **25**, 58–66, <https://doi.org/10.1002/pip.2810> (2017).
21. Zhang, T. *et al.* High efficiency solution-processed thin-film Cu(In,Ga)(Se,S)₂ solar cells. *Energy Environ. Sci.* **9**, 3674–3681, <https://doi.org/10.1039/c6ee02352e> (2016).
22. Munshi, A. *et al.* Polycrystalline CdSe/CdTe absorber cells with 28 mA/cm² short-circuit current. *IEEE Journal of Photovoltaics*. **8**(1), 310–314, <https://doi.org/10.1109/JPHOTOV.2017.2775139> (2018).
23. Paudel, N. & Yan, Y. Enhancing the photo-currents of CdTe thin-film solar cells in both short and long wavelength regions. *Appl. Phys. Lett.* **105**, 183510–183515, <https://doi.org/10.1063/1.4901532> (2014).
24. Poplawsky, J. *et al.* Structural and compositional dependence of the CdTe_{1-x}Se_x alloy layer photoactivity in CdTe-based solar cells. *Nat. Commun.* **7**, 12537, <https://doi.org/10.1038/ncomms12537> (2016).
25. Swanson, D., Sites, J. & Sampath, W. Co-sublimation of CdSe_{1-x}Te_x layers for CdTe solar Cells. *Solar Energy Mater & Solar Cells*. **159**, 389–394, <https://doi.org/10.1016/j.solmat.2016.09.025> (2017).
26. Dedoncker, R. *et al.* Reactive sputter deposition of CoCrCuFeNi in nitrogen/argon mixtures. *Journal of Alloys and Compounds*. **769**, 881–888, <https://doi.org/10.1016/j.jallcom.2018.08.044> (2018).
27. Sudhir, S. G. Control of the structure and surface morphology of gallium nitride and aluminum nitride thin films by nitrogen background pressure in pulsed laser deposition. *Journal of Electronic Materials*. **27**, 215–221, 10.1007%2Fs11664-998-0390-y.pdf (1998).
28. Xiao, S., Zhao, L., Liu, Y. & Lian, J. Nanocrystalline ZnO films prepared by pulsed laser deposition and their abnormal optical properties. *Applied Surface Science*. **283**, 781–787, <https://doi.org/10.1016/j.apsusc.2013.07.018> (2013).
29. Cracian, V., Elders, J., Gardieniers, J. G. E. & Boyd, W. I. Characteristics of high quality ZnO thin films deposited by pulsed laser Deposition. *Appl. Phys. Lett.* **65**, 2963–2965, 0003-6951/94/65(23)/2963/3/\$6.00 (1994).
30. Vathianathan, V., Lee, B. & Kim, S. Growth of phosphorus doped ZnO thin films by pulsed laser deposition. *phys. stat. sol.* **201**, 2837–2840, <https://doi.org/10.1002/pssa.200405030> (2004).
31. Man, Y. B., Xi, Z. H., Chen, S. C., Liu, M. & Wei, J. XRD study on the effect of the deposition condition on pulsed laser deposition of ZnO films. *Cent. Eur. J. Phys.* **6**, 643–647, <https://doi.org/10.2478/s11534-008-0062-9> (2008).
32. Tsoutsouva, M. G., Panagopoulou, C. N., Papadimitriou, D., Fasaki, I. & Kompitsas, M. ZnO thin films prepared by pulsed laser deposition. *Materials Science and Engineering B*. **176**, 480–483, <https://doi.org/10.1016/j.mseb.2010.03.059> (2011).
33. Franklin, J. B. *et al.* Optimised pulsed laser deposition of ZnO thin films on transparent conducting Substrates. *J. Mater. Chem.* **21**, 8178–8182, <https://doi.org/10.1039/c1jm10658a> (2011).
34. Zeng, N. J., Low, K. J., Ren, M. Z., Liew, T. & Lu, F. Y. Effect of deposition conditions on optical and electrical properties of ZnO films prepared by pulsed laser deposition. *Applied Surface Science*. **197–198**, 362–367, [https://doi.org/10.1016/S0169-4332\(02\)00425-7](https://doi.org/10.1016/S0169-4332(02)00425-7) (2002).
35. Perna, G. *et al.* ZnSe films deposited on crystalline GaAs and amorphous quartz substrates by means of pulsed laser ablation technique. *Eur. Phys. J. B*. **29**, 541–545, <https://doi.org/10.1140/epjb/e2002-00337-0> (2002).
36. Aly, A. S., Akl, A. A. & Howari, H. Effect of pulsed laser power annealing on structural and optical characteristics of ZnSe thin films. *Acta Physica Polonica A*. **128**, 414–418, <https://doi.org/10.12693/APhysPolA.128.414> (2015).
37. Reddy, S. T. & Kumar, S. M. C. Co-evaporated SnS thin films for visible light photodetector applications. *RSC Adv.* **6**, 95680–95692, <https://doi.org/10.1039/c6ra20129f> (2016).
38. Zhou, W. *et al.* Luminescence and local photonic confinement of single ZnSe:Mn nanostructure and the shape dependent lasing behavior. *Nanotechnology*. **24**, 055201, <https://doi.org/10.1088/0957-4484/24/5/055201> (2013).
39. Zhou, W., Liu, R., Tang, D. & Zou, B. The effect of dopant and optical micro-cavity on the photoluminescence of Mn-doped ZnSe nanobelts. *Nanoscale Research Letters*. **8**, 314, <https://doi.org/10.1186/1556-276X-8-314> (2013).
40. Hu, Z. D., Duan, X. F., Gao, M., Chen, Q. & Peng, L. M. ZnSe nanobelts and nanowires synthesized by a closed space vapor transport technique. *J Phys Chem C*. **111**, 2987–2991, <https://doi.org/10.1021/jp067556e> (2007).
41. Yang, Q. *et al.* Extended photoresponse and multi-band luminescence of ZnO/ZnSe core/shell nanorods. *Nanoscale Research Letters*. **9**, 31, <https://doi.org/10.1186/1556-276X-9-31> (2014).
42. Shen, L. *et al.* Direct synthesis of ZnO nanoparticles by a solution-free mechanochemical reaction. *Nanotechnology*. **17**, 5117–5123, <https://doi.org/10.1088/0957-4484/17/20/013> (2006).
43. Xu, X. L., Lau, S. P., Chen, G. Y. & Tay, B. K. Polycrystalline ZnO thin films on Si (100) deposited by filtered cathodic vacuum arc. *J. Cryst. Growth*. **223**, 201–205, [https://doi.org/10.1016/S0022-0248\(01\)00611-X](https://doi.org/10.1016/S0022-0248(01)00611-X) (2001).
44. Bundesmann, C. *et al.* Raman scattering in ZnO thin films doped with Fe, Sb, Al, Ga, and Li. *Appl. Phys. Lett.* **83**, 1974–1976, <https://doi.org/10.1063/1.1609251> (2003).
45. Kaschner, A. *et al.* Nitrogen-related local vibrational modes in ZnO: N. *Appl. Phys. Lett.* **80**, 1909–1911, <https://doi.org/10.1063/1.1461903> (2002).
46. Kim, M.-Y., Naveen, M. H., Gurudatt, N. G. & Shim, Y.-B. Detection of nitric oxide from living cells using polymeric zinc organic frame work- derived zinc oxide composite with conducting polymer. *Advanced science news*. **1700502**, 1–10, <https://doi.org/10.1002/asmll.201700502> (2017).
47. Al-Gaashani, R., Radiman, S., Daud, A. R., Tabet, N. & Al-Douri, Y. XPS and optical studies of different morphologies of ZnO nanostructures prepared by microwave methods. *Ceramics International*. **39**, 2283–2292, <https://doi.org/10.1016/j.ceramint.2012.08.075> (2013).
48. Kumar, D. R., Manoj, D. & Santhanalakshmi, J. Au–ZnO bullet-like heterodimer nanoparticles: synthesis and use for enhanced nonenzymatic electrochemical determination of glucose. *RSC Adv.* **4**, 8943–8952, <https://doi.org/10.1039/c3ra45269g> (2014).
49. Ganesh, R. S. *et al.* Influence of Al doping on the structural, morphological, optical, and gas sensing properties of ZnO nanorods. *Journal of Alloys and Compounds*. **698**, 555–564, <https://doi.org/10.1016/j.jallcom.2016.12.187> (2017).
50. Qiao, F. *et al.* Tunability in the optical and electronic properties of ZnSe microspheres via Ag and Mn doping. *ACS Omega*. **4**, 12271–12277, <https://doi.org/10.1021/acsomega.9b01539> (2019).
51. Bera, S., Dhara, S., Velmurugan, S. & Tyagi, A. K. Analysis on Binding Energy and Auger Parameter for Estimating Size and Stoichiometry of ZnO Nanorods. *International Journal of Spectroscopy*. **371092**, <https://doi.org/10.1155/2012/371092> (2012).
52. Naumkin, A. V., Kraut-Vass, A., Gaarenstroom, S.W. & Powell, C. J. NIST X-ray Photoelectron Spectroscopy Database. *NIST Standard Reference Database 20, Version 4.1*, <https://doi.org/10.18434/FT4T88K> (2012).

53. Hesse, R. *et al.* Unifit for Windows (Line Positions and Data Formats), version 2018, Scientific Software GmbH, <http://www.unifitsoftware.de/PDF/Line%20Positions%20and%20Data%20Formats-unifit2018.pdf> (2018).
54. Cheng, Q., Wang, D. & Zhou, H. Electrodeposition of Zn(O,S) (zinc oxysulfide) thin films: Exploiting its thermodynamic and kinetic processes with incorporation of tartaric acid. *Journal of Energy Chemistry*. **27**, 913–922, <https://doi.org/10.1016/j.jechem.2017.07.020> (2017).
55. Natsume, Y. & Sakata, H. Zinc oxide films prepared by sol-gel spin-coating. *Thin Solid Films*. **372**, 30–36, [https://doi.org/10.1016/S0040-6090\(00\)01056-7](https://doi.org/10.1016/S0040-6090(00)01056-7) (2000).

Acknowledgements

This research was supported by the institutional research funding IUT19-28 Project of the Estonian Ministry of Education and Research, the European Union through the European Regional Development Fund, Project TK141, partly from IUT-19-11 and IUT19-4 of the Estonian Ministry of Education and Research, Project B54 of the Estonian Science foundation, PUT1495 Project of the Estonian Ministry of Education and Research, the European Union through the European Regional Development Fund, Project TK141. The authors are grateful to PRS service for proof-reading this manuscript.

Author contributions

Sergei Bereznev and Akram Abdalla planned and designed the study. A. Abdalla conducted all experimental work with major role in writing and processed all figures and tables. All the experiments are thoroughly supervised by S. Bereznev and provided his assistant where required with minor role in writing. N. Spalatu contributed in the electrical part and XRD interpretation. O. Volobujeva performed HR-SEM and EDX characterization. N. Sleptsuk conducted electrical measurements. M. Danilson measured and analysed XPS part. All authors reviewed the manuscript and agreed about the contents.

Competing interests

The authors declare no competing interests.

Additional information

Supplementary information is available for this paper at <https://doi.org/10.1038/s41598-019-54008-1>.

Correspondence and requests for materials should be addressed to A.A.

Reprints and permissions information is available at www.nature.com/reprints.

Publisher's note Springer Nature remains neutral with regard to jurisdictional claims in published maps and institutional affiliations.



Open Access This article is licensed under a Creative Commons Attribution 4.0 International License, which permits use, sharing, adaptation, distribution and reproduction in any medium or format, as long as you give appropriate credit to the original author(s) and the source, provide a link to the Creative Commons license, and indicate if changes were made. The images or other third party material in this article are included in the article's Creative Commons license, unless indicated otherwise in a credit line to the material. If material is not included in the article's Creative Commons license and your intended use is not permitted by statutory regulation or exceeds the permitted use, you will need to obtain permission directly from the copyright holder. To view a copy of this license, visit <http://creativecommons.org/licenses/by/4.0/>.

© The Author(s) 2019

Publication II

Akram Abdalla, Erki Kärber, Valdek Mikli, Sergei Bereznev. The effect of laser fluences on the structural and optoelectronic properties of Zn(O,Se) films. *Materials Science in Semiconductor Processing*. 2021, 121, 105429.



Contents lists available at ScienceDirect

Materials Science in Semiconductor Processing

journal homepage: <http://www.elsevier.com/locate/mssp>

The effect of laser fluences on the structural and optoelectronic properties of Zn(O,Se) films

Akram Abdalla^{*}, Erki Kärber, Valdek Mikli, Sergei Bereznev^{**}

School of Engineering, Department of Materials and Environmental Technology, Tallinn University of Technology, Ehitajate Tee 5, Tallinn, 19086, Estonia

ARTICLE INFO

Keywords:

PLD
Laser fluences
Zn(O,Se)
Buffer layer

ABSTRACT

Zinc oxy-selenide (Zn(O,Se)) is a prospective semiconductor that could be applied as a buffer layer in optoelectronic devices as an alternative for toxic CdS layers. A complete investigation of the effect of changing laser fluences from 4 to 6 J cm⁻² on the phase composition, optical and electrical properties of Zn(O,Se) films prepared by pulsed laser deposition in a high vacuum at 500°C is reported. Deposited Zn(O,Se) films were characterized using HR-SEM, XRD, UV-Vis, and Hall effect measurements. HR-SEM micrographs illustrated the deposition of uniform, adherent, and compact Zn(O,Se) films. XRD investigation confirmed the formation of a Zn(O,Se) phase at 500°C for all three laser fluences. In addition, the UV-Vis transmittance spectra indicated the relative transparency of the deposited films in the visible range, accompanied by a redshift in the absorption edges as the laser fluences increased. Electrical measurements showed a significant increase of the electron concentration and electrical conductivity in the obtained films as laser fluence increased to 6 J cm⁻².

1. Introduction

Substituting the anion or cation for an isoelectric element might have an excellent effect on the optoelectronic and structural properties of a semiconductor, particularly if there is a reasonable difference in the covalent radii and electronegativity between the substituting elements and the host atoms. Recently, a partial substitution of the anion site of CdTe absorber layers, via the incorporation of selenium, led to the band gap grading of the CdTe absorber, which improved the material performance significantly [1–4]. For example, CdSe was combined with CdTe absorber as a buffer layer, and the cell performance was enhanced and showed a high photoconversion efficiency of 14.7% [1,5]. It was reported that during fabrication, the CdSe penetrated to the CdTe lattice and formed a low band gap, high absorption capability alloy of CdTe_{1-x}Se_x [5,6]. As a result, this elongated the carrier lifetime and enhanced the absorption efficiency in the shorter and longer wavelength ranges [4,7]. The process of band gap engineering for semiconductors is attractive for different applications. For example, the partial replacement of the arsenic site in GaAs with nitrogen atoms is a hot area of research for near-infrared laser technology. For ZnO used in optoelectronic applications, both sites can be partially substituted. The Zn site has been partially substituted by Mg and Cd atoms to form Zn_{1-x}Mg_xO

and Zn_{1-x}Cd_xO, respectively [8]. Partial replacement of the O site was also performed by S and Se atoms etc. which formed ZnO_{1-x}S_x and ZnO_{1-x}Se_x and significantly affected the structural, optical, and electrical properties.

We focused our attention on Zn(O,Se), which is a promising semiconductor due to its advantageous properties such as earth abundance, a tunable wide band gap and less toxic compared to CdS [9,10]. The band gap of Zn(O,Se) range from 2.70 to ~3.30 eV, depending on the growth temperature and selenium ratios [9,10]. Zn(O,Se) is a suitable alternative variant for replacing the CdS buffer layer in solar cells and other optoelectronic devices because this material is nearly transparent in the visible part of the spectra and less toxic compared to CdS. It is possible to prepare Zn(O,Se) thin films via various techniques. Iwata et al. [11] deposited ZnO_{1-x}Se_x films by radio frequency molecular beam epitaxy (RF-MBE) at 350°C onto a sapphire substrate and found a decreasing band gap trend with increasing Se content. Polity et al. [12] also deposited ZnO_{1-x}Se_x by RF-sputtering at 340°C onto a glass/sapphire substrate, reported the limited solubility of O in ZnSe, and confirmed the band gap change with the Se ratio. Moreover, Mayer et al. [13] grew ZnO_{1-x}Se_x films by pulsed laser deposition (PLD) at 200–500°C onto sapphire substrates with varying x ratios, from 0 to 0.12, which also supported the variation in the band gap with the variations of Se

^{*} Corresponding author.

^{**} Corresponding author.

E-mail addresses: akrami.abdalla@gmail.com (A. Abdalla), sergei.bereznev@taltech.ee (S. Bereznev).

<https://doi.org/10.1016/j.mssp.2020.105429>

Received 12 March 2020; Received in revised form 20 July 2020; Accepted 27 August 2020
1369-8001/© 2020 Elsevier Ltd. All rights reserved.

content. We also previously deposited $\text{ZnO}_{1-x}\text{Se}_x$ films by PLD in nitrogen back-pressure and high vacuum [9,10], the crystal structure of the $\text{ZnO}_{1-x}\text{Se}_x$ phase formed at 500°C , while above 500°C , the solubility of Se in ZnO, and the solubility of O in ZnSe decreased. Hence, the deposition conditions and all parameters related to PLD should be investigated to improve the optical, electrical, and structural properties of the resultant Zn(O,Se) films.

The goal of this contribution is to study the effect of laser fluences variation on the structural and optoelectronic properties of Zn(O,Se) films deposited at 500°C in a high vacuum.

2. Materials and methods

2.1. Growth of Zn(O,Se) films

Zn(O,Se) thin films were grown onto glass substrates by PLD at 500°C in a high vacuum. All details of the substrate preparation steps (soda-lime glass (SLG), 3.6×3.6 cm in size) and the Zn(O,Se) target description were reported in our previous studies [9,10]. The films growth was completed using a Neocera Pioneer PLD system equipped with a 248 nm KrF excimer laser. The distance between the substrate and target was 9 cm [9,10]. Laser fluences were changed from 4 J cm^{-2} to 6 J cm^{-2} . For all laser fluences, identical growth parameters were maintained (500°C substrate temperature, 80 min deposition time, and 10 Hz repetition rate). For comparison, ZnSe and ZnO thin films were grown onto SLG by PLD under the same conditions as well. The substrate and target were rotated; additionally, the target was rastered during the deposition process [9,10].

2.2. Characterization

The surface and cross-section morphologies of the grown Zn(O,Se) films were studied using a ZEISS Ultra 55 scanning electron microscope (SEM). Energy-dispersive X-ray spectroscopy (EDS) (Bruker ESPRIT system 1.82) was used to determine the atomic ratios of the elements in the prepared films [14]. The structural and phase composition of the obtained films were determined using a Rigaku Ultima IV diffractometer with $\text{Cu K}\alpha$ radiation. UV–Vis transmittance spectra were measured using a Shimadzu UV–1800 spectrophotometer at a 300–1000 nm wavelength range, and the electrical properties were analyzed at RT using the MMR's variable temperature Hall System equipped with a Hall van der Pauw controller H-50. Indium was used as a contact material for the four-probe contact preparation in van der Pauw geometry [9,10].

3. Results and discussion

3.1. XRD analysis

Fig. 1 presents the XRD diffractogram of Zn(O,Se) films grown at 500°C by using three different laser fluences, 4, 5, and 6 J cm^{-2} , and of ZnSe and ZnO films grown at the same substrate temperature and a 4 J cm^{-2} laser fluence for comparison. The ZnSe film showed a diffraction peak at 27.47° , attributable to the ZnSe cubic phase of the (111) plane [15,16]. While the diffraction peak of ZnO film appeared at 34.53° with an excellent index to the (002) plane of wurtzite ZnO structure [17–23]. The Zn(O,Se) films grown with different laser fluences in the $4\text{--}6 \text{ J cm}^{-2}$ range presented a single XRD peak at 33.70° , which referred to the formation of a ternary polycrystalline Zn(O,Se) phase. The peak positioned at 33.70° was previously identified as belonging to the (002) plane of $\text{ZnO}_{1-x}\text{Se}_x$, where x values changed from 0 to 0.12 [13,24,25].

A noticeable narrowing and increase in the diffraction peak intensities were observed with the shift of laser fluences from 4 to 6 J cm^{-2} , which leads to increasing crystalline sizes (Table 1). According to our assumption, the increase of the crystallite sizes at higher laser fluences can be connected with the increase of the kinetic energy and flux of the ablated species in the plasma plume, which significantly affects

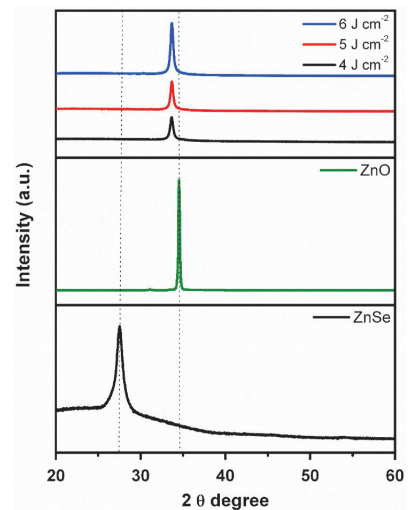


Fig. 1. XRD pattern of Zn(O,Se) films deposited at 500°C in different laser fluences of $4\text{--}6 \text{ J cm}^{-2}$.

Table 1

Crystallite sizes, atomic ratios, film thicknesses and band gap of Zn(O,Se) films deposited at 500°C with different laser fluences of $4\text{--}6 \text{ J cm}^{-2}$

Laser fluence (J cm^{-2})	Crystallite size (nm) ^a	atomic ratios			Film thickness (nm)	Band gap (eV)
		Zn	O	Se		
4	34 ± 0.3	50.0	41.6	8.4	340	3.03
5	40 ± 0.4	50.0	41.0	9.0	419	2.94
6	42 ± 0.5	50.0	42.0	8.0	445	2.87

^a represent standard deviation (s.d.)

^b Measurement uncertainty of EDS is $\pm 1.0\%$

the Zn(O,Se) film density and crystalline quality [17,23,26]. The crystalline sizes (D) of the Zn(O,Se) films were determined based on the Scherrer relation (1) [27].

$$D = \frac{0.94\lambda}{\beta \cos\theta} \quad (1)$$

where β is the full width at the half maximum (FWHM) (in radians) of the peak located at 33.70° in the 2θ , λ is the wavelength of X-ray radiation (1.5406 \AA), and θ is the Bragg angle.

3.2. SEM analysis

Fig. 2 shows the surface and cross-sectional high-resolution SEM photographs of the Zn(O,Se) films deposited at 500°C with varying the laser fluences from 4 to 6 J cm^{-2} . Uniform, compact, and adherent to the substrate Zn(O,Se) films were deposited. Furthermore, the cross-sectional views show that the thickness of the films increased from 340 to 445 nm as the laser fluences shifted from 4 to 6 J cm^{-2} . This phenomenon is connected with the availability of higher numbers of atoms and ions of Zn, O and Se at higher laser fluences [28].

The elemental compositions in the deposited films (Table 1) indicate a relatively stable composition throughout the range of laser fluences used.

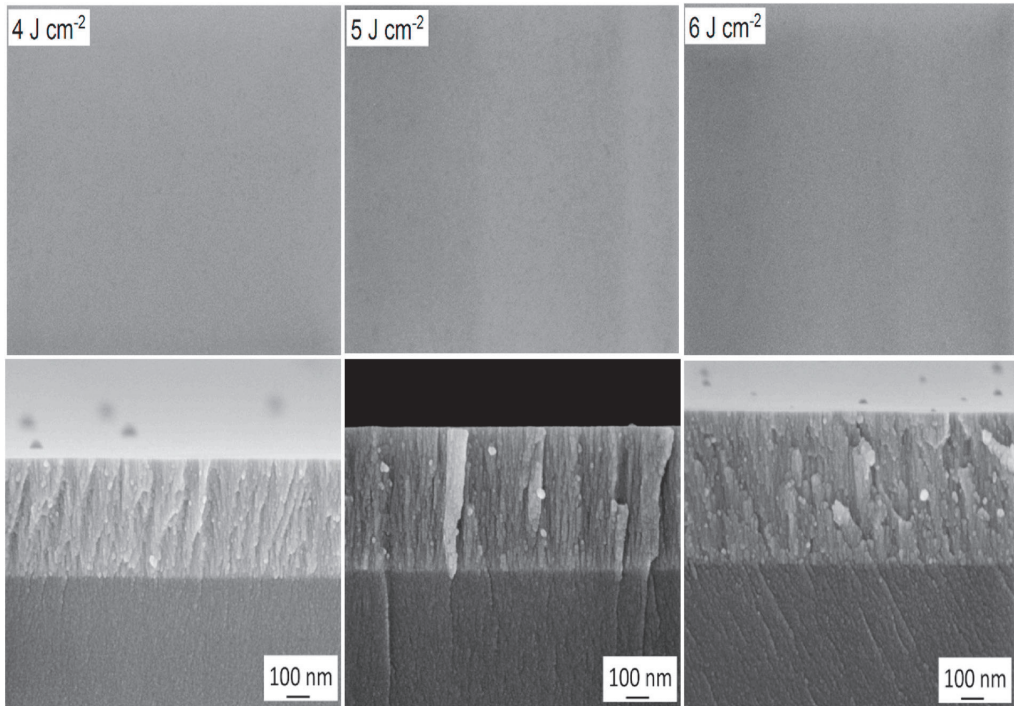


Fig. 2. Surface and cross-sectional SEM images of Zn(O,Se) films deposited at 500°C with different laser fluences of 4–6 J cm⁻².

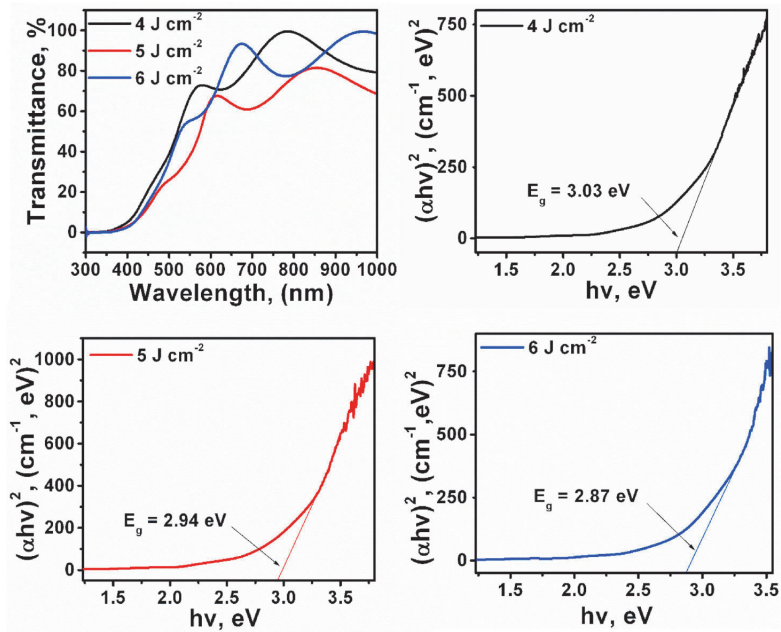


Fig. 3. Transmittance spectra and Optical band gap of Zn(O,Se) films deposited at 500°C with different laser fluences of 4–6 J cm⁻².

3.3. Optical analysis

Fig. 3 presents the UV–Vis transmittance spectra of the Zn(O,Se) films grown at 500°C with different laser fluences from 4 to 6 J cm⁻². All the formed Zn(O,Se) films are nearly transparent. When the laser fluences varied from 4 to 6 J cm⁻², the absorption edges shifted to a longer wavelength (redshift). This shift results from the change in the band structure of the films due to the introduction of Frenkel defects (Se and O vacancies). These defects create localized states in the electronic structure of the films [29–33]. The Tauc formula (2) was used in determining the band gap of the Zn(O,Se) films [34,35]. $(\alpha hv)^2$ was plotted against hv , and the linear part was extrapolated to the (x-axis) hv axis, see Figure (3). When the laser fluences varied from 4 to 6 J cm⁻², the band gap of the Zn(O,Se) films decreased from 3.03 to 2.87 eV. Hence, the decrease is attributable to the observed redshift in the absorption edges and an increase in the film thicknesses [10,36].

$$(\alpha hv) = A(hv - E_g)^n \quad (2)$$

where hv is the photon energy, α is the absorption coefficient and is estimated from $\alpha = 2.303 \log(T/d)$, T is the transmittance, d is the film thickness, exponent n depends on the transition type ($n = 1/2$ for direct allowed), and E_g is the band gap.

3.4. Electrical properties

Table 2 presents the electrical properties of the prepared Zn(O,Se) films for three different laser fluences, 4, 5, and 6 J cm⁻², based on Hall effect measurements. The electrons were the dominant carriers in all prepared Zn(O,Se) films due to the negative sign of the Hall coefficient (i.e. n-type conductivity).

The resistivity of Zn(O,Se) film deposited with a 4 J cm⁻² laser fluence was $6 \times 10^3 \Omega \text{ cm}$, which classified it as a high resistive film, while the electron concentration was $4 \times 10^{14} \text{ cm}^{-3}$. When the laser fluence was raised to 5 J cm⁻², the resistivity decreased to $4 \times 10^3 \Omega \text{ cm}$ and the electron concentration increased to $8 \times 10^{14} \text{ cm}^{-3}$. The trend was similar when increasing the laser fluence to 6 J cm⁻², and the resistivity decreased further, down to $6 \times 10^2 \Omega \text{ cm}$, mainly due to the corresponding increase of the electron concentration to $4 \times 10^{15} \text{ cm}^{-3}$. The electron mobility was similar in all samples, $2\text{--}3 \text{ cm}^2 \text{ V}^{-1} \text{ s}^{-1}$.

The reduction of the Zn(O,Se) film resistivity by one order of magnitude, in addition to the formation of a high electron concentration of nearly 10^{15} cm^{-3} at 6 J cm⁻² laser fluence reflects the most interesting finding. To explain these findings, the thermodynamic investigations from a previous study [9] were considered. In that study, the Gibbs free energies of the formation of ZnO, ZnSe, and SeO₂ and the dissociation reactions of Zn(O,Se), ZnSe, and ZnO were analyzed at the equilibrium medium of the gas and solid phases. The thermodynamic investigations revealed the formation of Frenkel defects, in other words, the creation of n-type intrinsic defects (oxygen and selenium vacancies), which leads to an increase in the overall electron concentration of Zn(O,Se) polycrystalline films [37,38], which in turn increases the electrical conductivity.

4. Conclusions

Homogeneous, adherent, and electrically conductive Zn(O,Se) films were grown using PLD for all applied laser fluences, 4–6 J cm⁻², at 500°C in a high vacuum. The atomic ratios of the elemental contents were relatively similar for all deposited Zn(O,Se) films. UV–Vis studies showed that the grown films are nearly transparent in the visible part of the spectra, with a minor decrease of the band gap values as the laser fluence increased. Laser fluence had a significant effect on the defect structure of the Zn(O,Se) films. Thus, its crystal structure improved with an increase in laser fluence.

Table 2

The electrical properties of the Zn(O,Se) films deposited at 500°C with different laser fluences of 4–6 J cm⁻²

Laser fluence (J cm ⁻²)	Resistivity ($\Omega \text{ cm}$)	Concentration (cm ⁻³)	Mobility (cm ² V ⁻¹ s ⁻¹)
4	6×10^3	4×10^{14}	3
5	4×10^3	8×10^{14}	2
6	6×10^2	4×10^{15}	3

Uncertainty of Hall effect measurements is $\pm 1.0\%$

Data availability

All data generated or analyzed during this study are included in this published article via (DOI: [10.17632/ktmwy73gwm.2](https://doi.org/10.17632/ktmwy73gwm.2)).

CRedit author contribution statement

Akram Abdalla: Writing - original draft, planned and designed the study, conducted all experimental work with major role in writing and processed all figures and tables. **Erki Kärber:** contributed in the XRD and electrical measurements with minor role in writing. **Valdek Mikli:** performed HR-SEM and EDS characterization. **Sergei Bereznev:** planned and designed the study. Thoroughly supervised all the experiments, and provided his assistant where required. All authors reviewed the manuscript and agreed about the contents.

Declaration of competing interest

The authors declare that they have no known competing financial interests or personal relationships that could have appeared to influence the work reported in this paper.

Acknowledgements

This research was supported by the European Union through the European Regional Development Fund project TK141, and by the project PRG627 of the Estonian Ministry of Education and Research.

References

- [1] T. Baines, G. Zoppi, L. Bowen, T.P. Shalvey, S. Mariotti, K. Durose, J.D. Major, Incorporation of CdSe layers into CdTe thin film solar cells, *Sol. Energy Mater. Sol. Cells* 180 (2018) 196–204, <https://doi.org/10.1016/j.solmat.2018.03.010>.
- [2] S.-H. Wu, C.W. Chang, H.J. Chen, C.F. Shih, Y.Y. Wang, C.-C. Li, S.-W. Chan, High-efficiency Cu₂ZnSn(S,Se)₄ solar cells fabricated through a low-cost solution process and a two-step heat treatment, *Prog. Photovoltaics Res. Appl.* 25 (2016) 58–66, <https://doi.org/10.1002/ppp.2810>.
- [3] T. Zhang, Y. Yang, D. Liu, S. Chi Tse, W. Cao, Z. Feng, S. Chen, L. Qian, High efficiency solution-processed thin-film Cu(In,Ga)(Se,S)₂ solar cells, *Energy Environ. Sci.* 9 (2016) 3674–3681, <https://doi.org/10.1039/c6ee02352e>.
- [4] A. Munshi, J. Kephart, A. Abbas, J. Raguse, J. Beaudry, K. Barth, J. Walls, W. Sampath, Polycrystalline CdSe/CdTe absorber cells with 28 mA/cm² short-circuit current, *IEEE Journal of Photovoltaics* 8 (2018) 310–314, <https://doi.org/10.1109/JPHOTOV.2017.2775139>.
- [5] N.R. Paudel, Y. Yan, Enhancing the photo-currents of CdTe thin-film solar cells in both short and long wavelength regions, *Appl. Phys. Lett.* 105 (2014) 183510–183515, <https://doi.org/10.1063/1.4901532>.
- [6] J.D. Poplawsky, W. Guo, N. Paudel, A. Ng, K. More, D. Leonard, Y. Yan, Structural and compositional dependence of the CdTe_xSe_(1-x) alloy layer photoactivity in CdTe-based solar cells, *Nat. Commun.* 7 (2016) 1–9, <https://doi.org/10.1038/ncomms12537>.
- [7] D.E. Swanson, J.R. Sites, W.S. Sampath, Co-sublimation of CdSe_{1-x}Te_x layers for CdTe solar cells, *Sol. Energy Mater. Sol. Cells* 159 (2017) 389–394, <https://doi.org/10.1016/j.solmat.2016.09.025>.
- [8] T. Makino, Y. Segawa, M. Kawasaki, A. Ohtomo, R. Shiroki, K. Tamura, T. Yasuda, H. Koinuma, Band gap engineering based on Mg₂Zn_{1-x}O and Cd₂Zn_{1-x}O ternary alloy films, *Appl. Phys. Lett.* 78 (2001) 1237, <https://doi.org/10.1063/1.1350632>.
- [9] Svetlana Politseva, Nicolae Spalatu, Akram Abdalla, Olga Volobujeva, Jaan Hiie, Sergei Bereznev, Pulsed laser deposition of Zn(O,Se) layers for optoelectronic application, *ACS Appl. Energy Mater.* 1 (2018) 6505–6512, <https://doi.org/10.1021/acsaem.8b01431>.
- [10] Akram Abdalla, Sergei Bereznev, Nicolae Spalatu, Olga Volobujeva, Natalja Sleptuk, Mati Danilson, Pulsed laser deposition of Zn(O,Se) layers in

- nitrogen background Pressure, *Sci. Rep.* 9 (2019) 1–9, <https://doi.org/10.1038/s41598-019-54008-1>.
- [11] K. Iwata, P. Fons, A. Yamada, H. Shibata, K. Matsubara, K. Nakahara, H. Takasu, S. Niki, Bandgap engineering of ZnO using Se, *phys. stat. sol.* 229 (2002) 887–890, [https://doi.org/10.1002/1521-3951\(200201\)229:2<887::AID-PSSB887>3.0.CO;2-G](https://doi.org/10.1002/1521-3951(200201)229:2<887::AID-PSSB887>3.0.CO;2-G).
- [12] Angelika Polity, Bruno K. Meyer, Thorsten Krämer, Changzhong Wang, Ute Haboeck, Axel Hoffmann, ZnO based ternary transparent conductors, *phys. stat. sol.* 203 (2006) 2867–2872, <https://doi.org/10.1002/pssa.200669570>.
- [13] Marie A. Mayer, Derrick T. Speaks, Man Yu Kin, Samuel S. Mao, Eugene E. Haller, Wladek Walukiewicz, Band structure engineering of $\text{ZnO}_{(1-x)}\text{Se}_x$ alloys, *Appl. Phys. Lett.* 97 (2010), <https://doi.org/10.1063/1.3464323>, 022104.
- [14] V. Miki, J. Hiie, V. Valdna, M. Viljus, R. Traksmaa, U. Kallavus, Formation of structure of the CdTe film, recrystallized on Mo/glass substrate under high temperature and mechanical pressure, *Thin Solid Film* 517 (2009) 2252–2255, <https://doi.org/10.1016/j.tsf.2008.10.102>.
- [15] G. Perna, V. Capozzi, M.C. Plantamura, A. Minafra, S. Orlando, V. Marotta, ZnSe films deposited on crystalline GaAs and amorphous quartz substrates by means of pulsed laser ablation technique, *Eur. Phys. J. B.* 29 (2002) 541–545, <https://doi.org/10.1140/epjb/e2002-00337-0>.
- [16] A.S. Aly, A.A. Akl, H. Howari, Effect of pulsed laser power annealing on structural and optical characteristics of ZnSe thin films, *Acta Phys. Pol., A* 128 (2015) 414–418, <https://doi.org/10.12693/APhysPolA.128.414>.
- [17] S. Xiao, L. Zhao, Y. Liu, J. Lian, Nanocrystalline ZnO films prepared by pulsed laser deposition and their abnormal optical properties, *Appl. Surf. Sci.* 283 (2013) 781–787, <https://doi.org/10.1016/j.apsusc.2013.07.018>.
- [18] V. Craciun, J. Elders, J.G.E. Gardeniers, W.I. Boyd, Characteristics of high quality ZnO thin films deposited by pulsed laser Deposition, *Appl. Phys. Lett.* 65 (1994) 2963–2965, 0003-6951/94/65(23)/2963/3/\$6.00.
- [19] V. Vaithianathan, B. Lee, S. Kim, Growth of phosphorus doped ZnO thin films by pulsed laser deposition, *phys. stat. sol.* 201 (2004) 2837–2840, <https://doi.org/10.1002/pssa.200405030>.
- [20] Y.B. Man, Z.H. Xi, S.C. Chen, M. Liu, J. Wei, XRD study on the effect of the deposition condition on pulsed laser deposition of ZnO films, *Cent. Eur. J. Phys.* 6 (2008) 643–647, <https://doi.org/10.2478/s11534-008-0062-9>.
- [21] M.G. Tsoutsouva, C.N. Panagopoulou, D. Papadimitriou, I. Fasaki, M. Kompitsas, ZnO thin films prepared by pulsed laser deposition, *Mater. Sci. Eng. B* 176 (2011) 480–483, <https://doi.org/10.1016/j.mseb.2010.03.059>.
- [22] J.B. Franklin, B. Zou, P. Petrov, D.W. McComb, M.P. Ryan, M.A. McLachlan, Optimised pulsed laser deposition of ZnO thin films on transparent conducting Substrates, *J. Mater. Chem.* 21 (2011) 8178–8182, <https://doi.org/10.1039/c1jm10658a>.
- [23] J.N. Zeng, K.J. Low, M.Z. Ren, T. Liew, F.Y. Lu, Effect of deposition conditions on optical and electrical properties of ZnO films prepared by pulsed laser deposition, *Appl. Surf. Sci.* 197–198 (2002) 362–367, [https://doi.org/10.1016/S0169-4332\(02\)00425-7](https://doi.org/10.1016/S0169-4332(02)00425-7).
- [24] Marie A. Mayer, Derrick T. Speaks, Man Yu Kin, Samuel S. Mao, Eugene E. Haller, Wladek Walukiewicz, Band structure engineering of $\text{ZnO}_{1-x}\text{Se}_x$ alloys, *Proceeding of SPIE*, 2010, p. 77700C, <https://doi.org/10.1117/12.859482>.
- [25] W. Shan, W. Walukiewicz, J.W. Ager III, K.M. Yu, J. Wu, E.E. Haller, Y. Nabetani, T. Mukawa, Y. Ito, T. Matsumoto, Effect of oxygen on the electronic band structure in $\text{ZnO}_x\text{Se}_{1-x}$ alloys, *Appl. Phys. Lett.* 83 (2003) 299, <https://doi.org/10.1063/1.1592885>.
- [26] Ashraf Hassan Farha, Ali Oguz Er, Yuksel Ufuktepe, E. Hani, Elsayed-Ali, Laser-fluence effects on NbNx thin films fabricated by pulsed laser deposition, *Mater. Chem. Phys.* 132 (2012) 667–672, <https://doi.org/10.1016/j.matchemphys.2011.11.084>.
- [27] S.T. Reddy, S.M.C. Kumar, Co-evaporated SnS thin films for visible light photodetector applications, *RSC Adv.* 6 (2016) 95680–95692, <https://doi.org/10.1039/c6ra20129f>.
- [28] Wai-Keat Lee, Hin-Yong Wong, Kah-Yoong Chan, Yong Thian-Khok, Seong-Shan Yap, Teck-Yong Tou, Effects of laser fluence on the structural properties of pulsed laser deposited ruthenium thin films, *Appl. Phys. A* 100 (2010) 561–568, <https://doi.org/10.1007/s00339-010-5875-x>.
- [29] Xianwu Xiu, Zhiyong Pang, Maoshui Lv, Ying Dai, Lina Ye, Shenghao Han, Transparent conducting molybdenum-doped zinc oxide films deposited by RF magnetron sputtering, *Appl. Surf. Sci.* 253 (2007) 3345–3348, <https://doi.org/10.1016/j.apsusc.2006.07.024>.
- [30] N. Khedmi, M. Ben Rabeha, M. Kanzari, Thickness dependent structural and optical properties of vacuum evaporated CuIn_2S_3 thin films, *Energy Procedia* 44 (2014) 61–68, <https://doi.org/10.1016/j.egypro.2013.12.010>.
- [31] M.G. Varnamkhasti, H.R. Fallah, M. Mostajaboddavati, A. Hassanzadeh, Influence of Ag thickness on electrical, optical and structural properties of nanocrystalline $\text{MoO}_3/\text{Ag}/\text{TTO}$ multilayer for optoelectronic applications, *Vacuum* 86 (2012) 1318–1322, <https://doi.org/10.1016/j.vacuum.2011.12.002>.
- [32] Stanford R. Ovshinsky, David Adler, Local structure, bonding, and electronic properties of covalent amorphous semiconductors, *Contemp. Phys.* 19 (2006) 109–126, <https://doi.org/10.1080/00107517808210876>.
- [33] El-Zahed, M. Dongol, M. Radwan, Annealing and thickness effect on the optical absorption of $\text{Ge}_{20}\text{Te}_{80}$ and $\text{Cu}_3\text{Ge}_{14}\text{Te}_{86}$ films, *Eur. Phys. J. AP* 17 (2002) 179–186, <https://doi.org/10.1051/epjap:2002010>.
- [34] Sergei Bereznev, Hrachya Kocharyan, Natalia Maticiu, Revathi Naidu, Olga Volobujeva, Andrey Tverjanovich, Julia Kois, One-stage pulsed laser deposition of conductive zinc oxysulfide layers, *Appl. Surf. Sci.* 425 (2017) 722–727, <https://doi.org/10.1016/j.apsusc.2017.07.078>.
- [35] Cheng Qiao, Dong Wang, Huanping Zhou, Electrodeposition of Zn(O,S) (zinc oxysulfide) thin films: Exploiting its thermodynamic and kinetic processes with incorporation of tartaric acid, *Journal of Energy Chemistry* 27 (2017) 913–922, <https://doi.org/10.1016/j.jechem.2017.07.020>.
- [36] A. Aly, A. Alaa, Akl, Influence of film thickness on optical absorption and energy gap of thermally evaporated $\text{CdS}_{0.1}\text{Se}_{0.9}$ thin films, *Chalcogenide Lett.* 12 (2015) 489–496, <https://www.researchgate.net/publication/282671368>.
- [37] Elvira Fortunato, Alexandra Goncalves, Vitor Assuncao, Antonio Marques, Hugo Águas, Luis Pereira, Isabel Ferreira, Rodrigo Martins, Growth of ZnO:Ga thin films at room temperature on polymeric substrates: thickness dependence, *Thin Solid Films* 442 (2003) 121–126, [https://doi.org/10.1016/S0040-6090\(03\)00958-1](https://doi.org/10.1016/S0040-6090(03)00958-1).
- [38] Marie A. Mayer, Man Yu Kin, Eugene E. Haller, Wladek Walukiewicz, Tuning structural, electrical, and optical properties of oxide alloys: $\text{ZnO}_{1-x}\text{Se}_x$, *J. Appl. Phys.* 111 (2012) 113505, <https://doi.org/10.1063/1.4724336>.

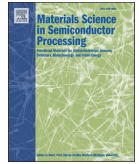
Publication III

Akram Abdalla, Mati Danilson, Souhaib Oueslati, Maris Pilvet and Sergei Bereznev. Amorphous Zn(O,Se) buffer layer for Cu(In,Ga)Se₂ thin film solar cells. *Materials Science in Semiconductor Processing*. 2021, 132, 105862.



Contents lists available at ScienceDirect

Materials Science in Semiconductor Processing

journal homepage: www.elsevier.com/locate/msspAmorphous Zn(O,Se) buffer layer for Cu(In,Ga)Se₂ thin film solar cellsAkram Abdalla^{*}, Mati Danilson, Souhaib Oueslati, Maris Pilvet, Sergei Bereznev

Department of Materials and Environmental Technology, School of Engineering, Tallinn University of Technology, Ehitajate tee 5, Tallinn, 19086, Estonia

ARTICLE INFO

Keywords:
Zn(O,Se)
Thickness effect
Solar cell
PLD

ABSTRACT

Amorphous Zn(O,Se) was used as a buffer layer with Cu(In,Ga)Se₂ absorber in thin film solar cells. The complete device was fabricated using vacuum technique only, and no wet method was involved. The solar cells parameters were investigated with a change in the thickness of the buffer layer from 100 to 300 nm. In addition, the performance of the fabricated solar cells was compared to that of a reference solar cell, using CdS as a buffer layer on Cu(In,Ga)Se₂. The preliminary results of this Cd-free solar cells showed a reasonable device performance. Also, the parasitic absorption in the blue region for the Cu(In,Ga)Se₂/Zn(O,Se) device has been reduced, due to high transparency and high optical band gap of amorphous Zn(O,Se) buffer. Moreover, the Zn(O,Se) is relatively less toxic than the CdS buffer layer. Thus, the parasitic absorption in the 350–550 nm range and the toxicity raised from using CdS as a buffer layer have been overcome. Furthermore, open circuit voltage, short circuit current and an overall photoconversion efficiency of the device were enhanced to 454 mV and 27.1 mA/cm² and 5.0% respectively with decreasing the thickness of amorphous Zn(O,Se) buffer layer to 100 nm.

1. Introduction

The chalcopyrite absorber Cu(In,Ga)Se₂ (CIGSe), with a high absorption coefficient and direct band gap (E_g), is one of the most efficient materials for thin film solar cells (TFSCs) [1–3]. Co-evaporation is the preferred method to produce highly photosensitive p-type CIGSe absorber layers [4]. The n-type buffer layer can be produced by different techniques, and has a significant function such as providing excellent optoelectronic properties at the absorber/window layer interface, increasing the overall solar cell performance. The buffer layer aids electron-hole separation, thus, decreasing interfacial charge recombination [5]. In order to design and develop a suitable buffer layer, it is important to fulfill the fundamental requirements relating to the electronic model of the device [6,7]. These requirements are defined as: proper conduction band (E_c) line-up between the window layer (i-ZnO) and the absorber layer; low optical absorption (i.e. relatively wide E_g); minimal defect density at the absorber/buffer interface; and the Fermi level (E_f) positioned close to the absorber conduction band at the absorber/buffer interface [6,7]. TFSCs which include photoabsorbers such as Cu₂ZnSnS₄ (CZTS), CIGSe and CdTe use n-type CdS usually prepared by chemical bath deposition (CBD) as a buffer layer [5–10]. The CdS fulfill main part from the needed requirements of buffer layer, which allows the highest efficiency (η) of these absorbers to be reached [3]. A CdS buffer layer protects the CIGSe absorber from the subsequent

deposition process through the entire coverage of the CIGSe surface. In addition, it forms optimal band alignment between the transparent conductive oxide (TCO) and the absorber layer [5]. However, CdS with $E_g = 2.45$ eV has some drawbacks, such as: parasitic absorption causing optical losses in the wavelength range of 350–550 nm; the environmental impact, due to the toxicity of Cd; and the CBD deposition method being non-vacuum method, in contrast with the vacuum production line of CIGSe and ZnO [5]. To overcome these issues, much research and development (R&D) was directed toward the replacement of CdS by a low-toxicity, wide band gap buffer layer. Also, to replace the CBD method by vacuum techniques such as close-space sublimation [11] etc. The development of Cd-free devices began in 1992 [6], and has been intensively investigated and developed, achieving a current record efficiency of 23.35% from the combination of Zn(O,S) buffer and Cu(In,Ga)(S,Se)₂ absorber [2,3,12,13]. Similarly, other buffer layer materials were investigated, including ZnS/ZnSe [14], In₂S₃/In₂Se₃ [15,16], Zn_{1-x}Mg_xO [17,18] and Zn(O,OH)_x/Zn(O,S,OH)_x [19]. Some of these materials have reached maturity [20] and show promising for industrial application, but intensive R&D is still required to develop potential buffers for highly efficient solar cells.

In our previous study, Zn(O,Se) has shown potential as a buffer layer in TFSCs [21], due to its suitable optoelectronic properties. E_g of Zn(O,Se) is wide and tunable, ranging between 2.70 eV to near 3.30 eV, and is dependent on deposition temperature, film thickness and the

^{*} Corresponding author.

E-mail addresses: akrami.abdalla@gmail.com, akram.ibrahim@taltech.ee (A. Abdalla).

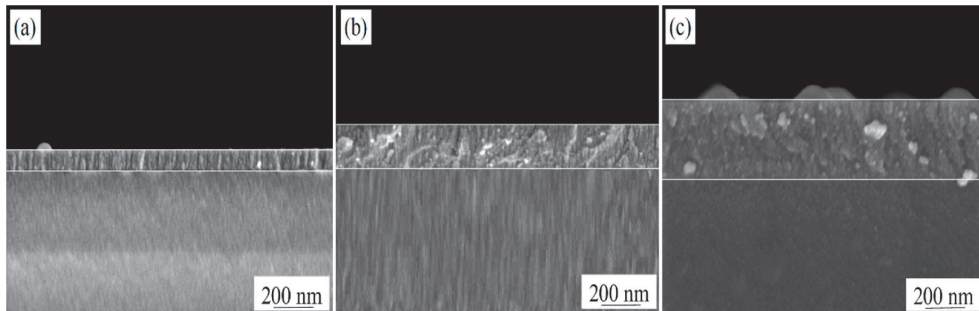


Fig. 1. Cross-sectional HR-SEM images of Zn(O,Se) buffer layers deposited on SLG substrate at RT with different thickness of (a) 100, (b) 200 nm and (c) 300 nm.

selenium-to-oxygen ratio [21]. The Zn(O,Se) layer deposited using the pulsed laser deposition (PLD) method was applied as a buffer layer with the CdTe absorber material, and a conversion efficiency of 8% was achieved for the non-optimized complete solar cell structure [21]. In the Zn(O,Se) system, parasitic absorption in the blue region was reduced, showing an advantage over the CdS buffer layer, in addition to low toxicity of Zn(O,Se) vs. CdS [21,22].

The aim of this study was to explore the possibility of using Zn(O,Se) as a buffer layer in a complete CIGSe solar cell structure, and to investigate the optimal thickness of the Zn(O,Se) buffer layer for the CIGSe absorber. A comparison of solar cell performance containing the Zn(O,Se) buffer layer with a reference cell, containing a CdS buffer layer, was also performed.

2. Materials and methods

2.1. Device fabrication

The glass/Mo/CIGSe structures were received from Ångström Solar Center, Uppsala University. A CIGSe absorber was co-evaporated onto soda-lime glass (SLG), coated with sputtered Mo as a back contact, using a three-stage process at a substrate temperature of approximately 550°C. The co-evaporated CIGSe layer had E_g of 1.00 eV and an average atomic ratio of $[Cu]/([Ga]+[In]) = 0.89$ (CGI), $[Ga]/([Ga]+[In]) = 0.23$ (GGI), and $[Se]/([Cu]+[Ga]+[In]) = 1.10$ as determined by x-ray fluorescence (XRF) spectrometry. In the next step, in our lab an amorphous $ZnO_{0.73}Se_{0.27}$ (a-Zn(O,Se)) buffer layer, with a thickness of 100, 200 and 300 nm, was deposited on top of the CIGSe surface and onto SLG substrate for optical and elemental analysis, at room temperature (RT) by PLD in high vacuum [21]. The growth of the $ZnO_{0.73}Se_{0.27}$ layers was done by Neocera pioneer PLD system integrated with KrF excimer laser 248 nm (Coherent Compex Pro 102). The pressure in the vacuum chamber during the deposition of layers was around 10^{-6} Torr, while the distance between substrate and target was 9 cm. The deposition time varied as 20, 40 and 60 min to prepare Zn(O,Se) layers with the thickness 100, 200 and 300 nm respectively. For each deposition we applied similar conditions as follow (200 mJ pulse energy, 10 Hz repetition rate). The laser beam was focused on ~ 5 mm² spot on the surface of Zn(O,Se) target. A top electrode, consisting of *i*-ZnO and ZnO:Al layers, was

sequentially deposited by RF-magnetron sputtering technique [23], from an undoped and a 1.5 at% Al-doped ceramic ZnO target. The stack of the complete device was glass/Mo/CIGSe/Zn(O,Se)/*i*-ZnO/ZnO:Al. Each of the three samples were sectioned into small cells with an area of approximately 0.06 cm², by mechanical scribing.

2.2. Characterization

The optical properties of Zn(O,Se) buffer layers were determined from UV–Vis transmittance spectra, the E_g values were calculated based on the Tauc relation [24,25]. The cross-sectional morphologies of bare Zn(O,Se) buffer layers on SLG substrate and CIGSe/Zn(O,Se) devices were studied using a ZEISS Ultra 55 high resolution scanning electron microscope (HR-SEM) [26]. The elemental ratio of the Zn(O,Se) buffer layers were investigated by energy dispersive x-ray spectroscopy (EDS). Depth profile analysis of the CIGSe/Zn(O,Se) structure was performed by Axis Ultra DLD XPS spectrometer with monochromatic Al K α x-ray radiation (1486.6 eV). The analysis area is defined by field of view selection. Field of view Slot (400 × 800 μ m) was selected. The ejected photoelectrons were detected using a 180° hemispherical analyzer fitted with a 128-channel delay-line detector. The samples surfaces were sputter etched using Mini Beam I Ar⁺ ion source operated at 4 keV and 10 mA for 20 cycles, 1 min per cycle. The etching depth was correlated to the etching time using the thickness of the CIGSe/Zn(O,Se) structure determined from HR-SEM cross-section view.

The devices' performances were determined by measuring the current density–voltage characteristics (J – V) at RT. The J – V curves were measured using a Keithley 2400 source meter, under standard test conditions (AM 1.5, 100 mW/cm²) using a Newport Class AAA solar simulator. The series and shunt resistances were calculated from light J – V curves, based on the equation slope $\sim (R)^{-1}$. Thus, the series resistance (R_S) was calculated by taking the inverse of the slope at open circuit voltage (V_{OC}), while the shunt resistance (R_{SH}) was calculated by taking the inverse of the slope at short circuit current (J_{SC}). A standard halogen lamp was used as the light source for the external quantum efficiency (EQE) measurements, together with a computer-controlled prism monochromator (Carl Zeiss SPM-2, $f = 40$ cm). Monochromatic and modulated (120 Hz) light was focused on the front surface of the solar cell. The photogenerated short-circuit current signal was converted to potential using an Autolab PGSTAT30 potentiostat/galvanostat, and detected using a Stanford Research Systems lock-in amplifier (SR810DSP). The software that measures EQE scans the spectrum that exits the monochromator slit from the desired range, at the same time recording the signal from the lock-in amplifier [27].

Table 1

Comparison of the average atomic concentrations of Zn(O,Se) layers deposited at RT measured by different technique EDS and XPS.

Structure	Technique	atomic conc. (at%)		
		Zn	O	Se
Glass/Zn(O,Se)	EDS	50.00	36.50	13.50
CIGSe/Zn(O,Se)	XPS	52.50	36.00	11.50

Measurement uncertainty of EDS is $\pm 1.0\%$ and XPS is $\pm 10.0\%$.

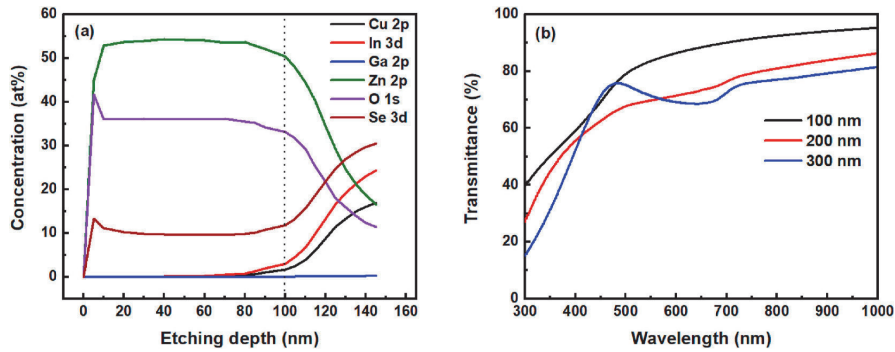


Fig. 2. (a) XPS depth profile analysis for a typical CIGSe/Zn(O,Se) structure showing the composition gradient of the Zn(O,Se) layer and CIGSe/Zn(O,Se) interface and (b) UV-Vis transmittance spectra of Zn(O,Se) buffer layers deposited on SLG substrate at RT with different thickness of 100–300 nm.

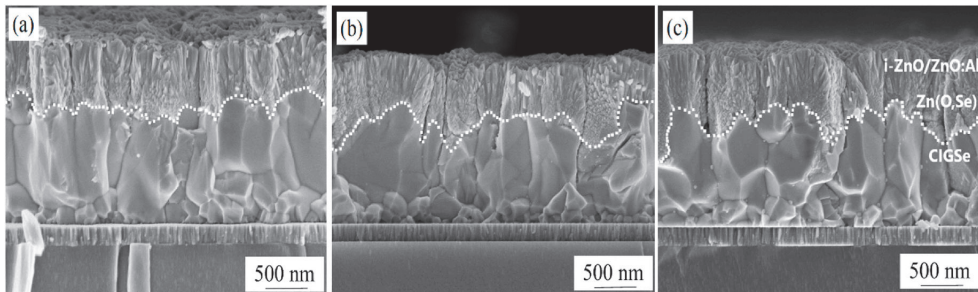


Fig. 3. Cross-sectional HR-SEM images of the complete CIGSe solar cell devices with different thickness of Zn(O,Se) buffer layer of (a) 100 nm, (b) 200 nm, (c) 300 nm.

3. Results and discussion

3.1. Optical, morphological and elemental analysis of Zn(O,Se) layers

Fig. 1a–c, show the cross-sectional HR-SEM micrograph of Zn(O,Se) buffer layers on glass substrate with different thicknesses (100, 200 and 300 nm). Compact and good adherent layers to glass substrate have been grown. Moreover, the elemental ratios of a-Zn(O,Se) layers were 50.00, 36.50 and 13.50 at% for Zn, O and Se respectively based on EDS analysis (see Table 1), for all three different thickness and did not change with the change in layer thickness. Thus, the selenium-to-oxygen composition ratio $[Se]/([O]+[Se])$ of a-Zn(O,Se) layers was constant 0.27 at%.

Fig. 2b, shows UV-Vis transmittance spectra of a-Zn(O,Se) films with different thicknesses 100–300 nm, deposited at RT by PLD in high vacuum. As can be seen, the 100 nm film thickness showed an average transparency around 85% in the visible region of the spectra, while 200 and 300 nm exhibited an average transparency around 75%. Additionally, the absorption edge shifted to longer wavelengths (red shift), from ~375 to ~485 nm, with film thickness increase from 100 to 300 nm. This is attributed to the disordered (defect) structure in the amorphous films [28–30]. The calculated optical E_g values are 3.05, 3.00 and 2.99 eV for 100, 200 and 300 nm-thick of the Zn(O,Se) buffer layers respectively. A negligible change from 3.05 to 2.99 eV in E_g is observed with an increase of the Zn(O,Se) film thickness from 100 to 300 nm.

3.2. XPS depth profile analysis of the CIGSe/Zn(O,Se) interface

Fig. 2a, shows XPS depth profile analysis of CIGSe/Zn(O,Se) structure. In the uppermost region up to 100 nm, only composition of the Zn(O,Se) layer is presented. Zn 2p, O 1s and Se 3d showed relatively

constant concentrations with an average around 52.50, 36.00, 11.50 at % respectively (see Table 1). These minor deviations in Zn, O, Se concentrations from stoichiometric ratios measured by EDS is referred to the XPS measurement accuracy and also, here Zn(O,Se) grown on the CIGSe. However, at the CIGSe/Zn(O,Se) interface the composition of Zn 2p and O 1s gradually decreased until reaching 16.50 and 11.50 at% at 140 nm. Furthermore, Cu 2p, In 3d, Ga 2p and Se 3d belonging to the CIGSe absorber started evolving steadily in the interface region. Cu 2p, In 3d and Se 3d increased gradually up to 16.50, 24.40 and 30.50 at% at 140 nm. However, the Ga 2p concentration changed in extremely narrow range from 0.07 to 0.26 at% at final etching depth reached 140 nm.

3.3. HR-SEM analysis of CIGSe/Zn(O,Se) device

Fig. 3a–c shows the cross-sectional HR-SEM images of the CIGSe/Zn(O,Se) devices coated with different thicknesses 100, 200 and 300 nm of the Zn(O,Se) buffer layer. Good coverage of the CIGSe absorber surface by the Zn(O,Se) buffer layer is observed. All deposited layers demonstrate dense and uniform morphology, with good adherence to the Mo/glass substrate and between other layers. The sputtered Mo and co-evaporated CIGSe layers had an average thickness of 0.3 ± 0.006 and 1.7 ± 0.08 μm , according to SEM cross-sectional analysis respectively, while the combined Zn(O,Se) and *i*-ZnO/ZnO:Al showed an average thickness of 900 ± 108 , the error (\pm) represent the standard deviation. The thickness of the buffer layer and the top electrode is estimated as one unit altogether using SEM cross-sectional view. The detailed thicknesses of the combined Zn(O,Se) and *i*-ZnO/ZnO:Al were 850, 800 and 1050 nm, with respect to the thickness of Zn(O,Se) buffer layer. The second layer is deviated by 150 nm from it is expected thickness with respect to 200 nm-thick Zn(O,Se) buffer layer. However, this deviation

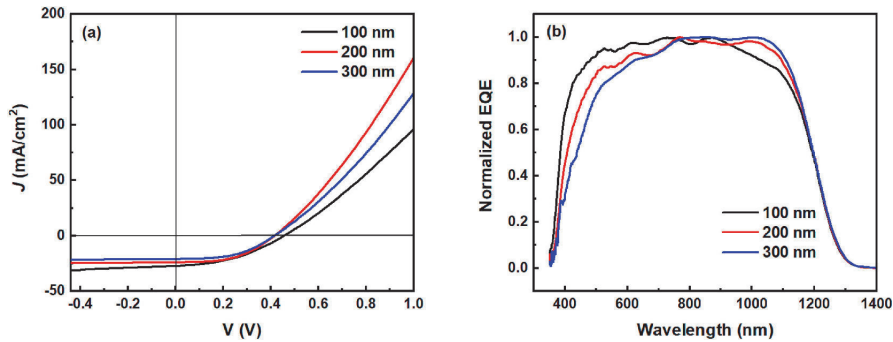


Fig. 4. (a) J - V curves and (b) EQE spectra of the CIGSe/Zn(O,Se) devices with different thickness of the buffer layer 100, 200, 300 nm.

Table 2

CIGSe solar cells parameters as a function of Zn(O,Se) buffer thickness, series and shunt resistance, saturation current, ideality factor, comparison to the reference cell with CdS buffer layer.

Thickness (nm)	100	200	300	CdS ref ^a
Cell size (cm ²)	0.06	0.06	0.06	0.05
η (%)	5.0 \pm 0.7	4.5 \pm 0.3	3.9 \pm 0.5	14.7
FF (%)	40.3 \pm 2	47.3 \pm 2	47.4 \pm 4	68.5
V_{OC} (mV)	454.0 \pm 7	395.0 \pm 1	395.0 \pm 4	560.0
J_{SC} (mA/cm ²)	27.1 \pm 5	23.9 \pm 3	20.9 \pm 1	38.2
R_s (Ω -cm ²)	6.0 \pm 1	3.1 \pm 0.04	3.5 \pm 2	0.2
R_{SH} (Ω -cm ²)	81.0 \pm 7	139.0 \pm 4	242.0 \pm 1	1.0 \times 10 ³
J_0 (mA/cm ²)	1.8 \pm 0.3 \times 10 ⁻⁴	2.4 \pm 0.5 \times 10 ⁻⁴	2.0 \pm 0.7 \times 10 ⁻⁴	2.0 \times 10 ⁻⁶
n	3.7 \pm 0.5	3.3 \pm 0.4	3.2 \pm 0.6	2.2

^a Prepared and measured at Uppsala University, Error (\pm) represent standard deviation.

correspond to the i-ZnO/ZnO:Al deposition because the thickness of the i-ZnO/ZnO:Al layer vary based on the location of the structure inside the sputtering chamber.

3.4. Effect of the Zn(O,Se) buffer thickness on the solar cells performance

Fig. 4a shows the J - V curve of the CIGSe solar cells with different thickness of Zn(O,Se) buffer layer 100–300 nm. Table 2 summarizes how solar cell parameters are affected by variation in thickness of Zn(O,Se) buffer layers deposited by PLD. As can be seen in Table 2, the highest efficiency of approximately 5.0% was obtained for the device with the lowest thickness 100 nm of Zn(O,Se) buffer layer. The general trend in J_{SC} values showed a reduction from 27.1 to 20.9 mA/cm² with increasing Zn(O,Se) buffer layer thickness from 100 to 300 nm. This gradual decrease in J_{SC} may be related to the fact that “PLD ablated materials contains macroscopic globules of molten material, up to \sim 10 μ m diameter” [31]. Thus, the arrival of these particulates at the substrate is clearly harmful to the properties of the already-deposited layer, as 200 and 300 nm-thick layers took longer time of deposition in the PLD chamber, the amount of damage (defects) is relatively high compared to the 100 nm-thick layer. This may, in turn, reduce carrier collection by impeding the photogenerated electrons [32,33]. Moreover, the CIGSe/Zn(O,Se) device with a 100 nm-thick buffer layer showed an enhanced spectral response over the wide wavelength range (300–760 nm) compared to the devices with 200 and 300 nm-thick buffer layers, which is directly reflected in the J_{SC} values.

The V_{OC} values were significantly decreased with increasing Zn(O,Se) buffer layer thickness, from 454 to 395 mV. The significant low V_{OC} values are caused by the recombination losses at absorber/buffer interface, which resulted from an increased thickness of a-Zn(O,Se)

buffer layer [32,34]. In the thicker buffer layer, E_F at the absorber/buffer interface move further away from the conduction band edge, causing a high potential drop in the buffer layer with increasing thickness of the Zn(O,Se) buffer layer [32,34]. At the same time, the potential will decrease in the whole heterostructure by the same amount as in the buffer layer, and the hole barrier will not change. In other words, the electron concentration will decrease [35], while the hole concentration will remain constant with increasing buffer layer thickness; as a result, inversion in the top-most part of the absorber layer will decrease. Consequently, the recombination rate will increase through the CIGSe/Zn(O,Se) interface resulting in low V_{OC} [18,28,35].

Furthermore, the properties of the junction were determined by fitting the saturation current density (J_0) and ideality factor (n) to the J - V curves of the individual cells using one diode model and presented in Table 2. The theoretical approach predicts diode ideality factors in a range $1 \leq n \leq 2$ dependent on the energy of the recombination center and the respective capture cross sections for electrons and holes. The explanation of $n > 2$ is not possible by considering recombination via a single recombination center. A multiple step recombination process via a series of trap states distributed in space and energy would explain such large ideality factors for a recombination process situated in the space-charge region [36].

The preceding discussion made clear that the ideality factor is strongly influenced by the recombination mechanism. The ideality factor is close to but slightly higher than 2 in case of the reference cell, which means that the recombination is dominated by the space-charge region in the absorber [32]. The higher fitted ideality factor values of cells fabricated using Zn(O,Se) buffer layer suggested that the deposition of such layer using PLD led to additional recombination centers in the space-charge region and recombination at absorber/buffer interface.

The saturation current, is an estimation of the “leakage” of carriers across the p-n junction in reverse bias. This leakage is a result of carrier recombination in the neutral regions. Thus, this mean the saturation current is a measure of the recombination in a device. A diode with a larger recombination will have a larger J_0 . The saturation current strongly influence the V_{OC} with a good agreement with the V_{OC} values in Table 2. The higher the J_0 , correspond to the lower V_{OC} .

The EQE spectra show an enhanced spectral response of the CIGSe/Zn(O,Se) devices in wavelengths region (350–760 nm) for the thinnest Zn(O,Se) buffer layer 100 nm see Fig. 4b. This may be due to the relatively high transparency and high E_g of the Zn(O,Se) buffer layer with 100 nm thickness, compared to the other thickness 200 and 300 nm, as reported in optical properties of the Zn(O,Se) buffer layer section 3.1. However, in a very narrow wavelength range (1000–1113 nm), enhanced spectral responses are observed for the CIGSe/Zn(O,Se) devices fabricated with higher-thickness 200 and 300 nm buffer layers see Fig. 4b. In general, the decrease of EQE in IR region in TFSCs is referred to different reasons such as rear surface recombination, insufficient light

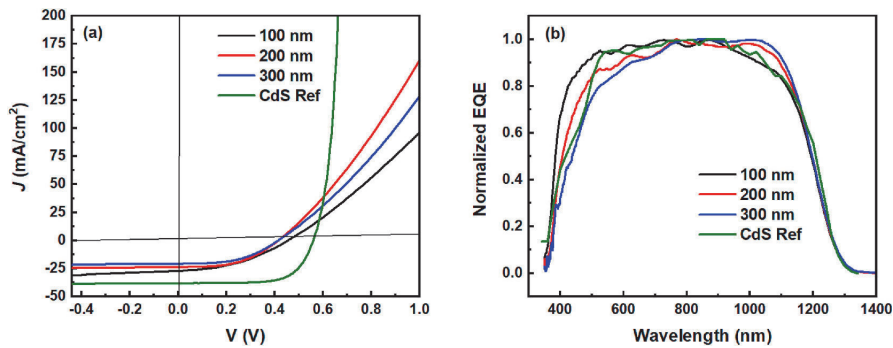


Fig. 5. Comparison of (a) J - V curves and (b) EQE spectra of the CIGSe/Zn(O,Se) cells with CIGSe/CdS reference cell.

absorption close to CIGSe band gap, and incomplete collection of the photogenerated carriers [37,38]. However, these affects are equal in all three cells, but due to high R_S of 100 nm device their affect became more pronounced and reduced the EQE in IR region for that specific cell.

The solar cell parameters of the highest-performing device, based on CIGSe/Zn(O,Se) with 100 nm thickness, was compared to the CIGSe/CdS reference cell (prepared and measured at Ångström Solar Center, Uppsala University) see Fig. 5a. The J_{SC} value of the CIGSe/Zn(O,Se) device is relatively low compared to the reference cell. However, a noticeable difference in V_{OC} and FF values were observed, confirming the presence of recombination losses as discussed previously, in addition to the parasitic resistance such as high R_S and low R_{SH} . Moreover, the short period of unavoidable air exposure of the CIGSe surface during transfer to the PLD deposition chamber results in oxidation of Cu, In, Ga and Se [35,39,40]. However, the ammonia in the CBD process etches the oxides, leaving a chemically clean CIGSe surface [35,39,40]. As the ammonia etching effect is absent in dry buffer layer deposition process, such as PLD, all residual aging products left on the CIGSe surface during the PLD deposition process stay at the interface. Therefore, reducing the quality of the CIGSe/Zn(O,Se) interface consequently presents opportunities for recombination losses at the interface [35]. The combination of a PLD system with a glove box is a promising approach, and may be can prevent CIGSe surface from oxidation and deterioration.

The EQE spectra of the highest-performing device fabricated with 100 nm-thick Zn(O,Se) buffer layer was compared to the EQE spectra of reference cell with CdS buffer layer Fig. 5b. The CIGSe/Zn(O,Se) device shows a high spectral response in the short wavelength region (360–550 nm) than CIGSe/CdS reference cell. Thus, this may be attributed to the high $E_g \geq 3.00$ eV of the Zn(O,Se) buffer layer compared to that of the CdS around 2.45 eV. For the rest of the wavelengths, the spectral responses of the CIGSe devices fabricated with both buffers (Zn(O,Se) or CdS) are quite similar.

4. Conclusion

This study reports how CIGSe/Zn(O,Se) solar cell performance is affected by thickness variation of the PLD-grown a-Zn(O,Se) buffer layers, and its performance compared with a CIGSe/CdS reference cell. The study confirmed that the complete solar cell structure, based on a CIGSe photoabsorber and the a-Zn(O,Se) buffer layer, is workable, and promising. The effect of changing film thickness of the a-Zn(O,Se) buffer layer on the J - V characteristic of the solar cells showed an increasing trend of an overall device performance, V_{OC} and J_{SC} to 5.0%, 454 mV and 27.1 mA/cm² respectively with the decrease of the a-Zn(O,Se) buffer layer thickness. An application of this Cd-free buffer layer overcome the drawbacks of the CdS. Thus, the Zn(O,Se) is less toxic than CdS and the EQE showed an enhanced spectral response in the short wavelength region 350–550 nm compared to the reference cell with CdS

buffer layer.

Author contribution

Akram Abdalla, and Sergei Bereznev planned and designed the study. A. Abdalla conducted all experimental work with major role in writing and processed all figures and tables. M. Danilson performed the EQE spectra measurement. S. Oueslati contributed in data interpretation and results analysis. M. Pilvet conducted the deposition of i-ZnO/ZnO:Al layers. All the experiments are thoroughly supervised by S. Bereznev and provided his assistant where required. All authors reviewed the manuscript and agreed about the contents.

Data availability

All data generated or analyzed during this study are provided in this manuscript.

Declaration of competing interest

The authors declare that they have no known competing financial interests or personal relationships that could have appeared to influence the work reported in this paper.

Acknowledgements

This research was supported by the European Union through the European Regional Development Fund project "Center of Excellence" TK141, and partially supported by ASTRA "TUT Institutional Development Programme for 2016–2022" Graduate school of Functional Materials and Technologies (2014-2020.4.01.16-0032), Estonia. Authors are gratefully thankful to Dr. Jan Keller for providing the p-type CIGSe absorber layer samples, and information about the reference cell with CdS layers. Also, to Dr. Valdek Mikli for SEM cross-section characterization.

References

- [1] Kihwan Kim, Liudmila Larina, Jae Ho Yun, Kyung Hoon Yoon, HyukSang Kwon, Byung Tae Ahn, Cd-free CIGS solar cells with buffer layer based on the In_2S_3 derivatives, Phys. Chem. Chem. Phys. 15 (2013) 9239, <https://doi.org/10.1039/c3cp50324k>.
- [2] Martin A. Green, Ewan D. Dunlop, Jochen Hohl-Ebinger, Masahiro Yoshita, Nikos Kopidakis, Anita W.Y. Ho-Baillie, Solar cell efficiency tables (version 55), Prog. Photovoltaics Res. Appl. 28 (2020) 3–15, <https://doi.org/10.1002/pip.3228>.
- [3] Martin A. Green, Ewan D. Dunlop, Dean H. Levi, Jochen Hohl-Ebinger, Masahiro Yoshita, Anita W.Y. Ho-Baillie, Solar cell efficiency tables (version 54), Prog. Photovoltaics Res. Appl. 27 (2019) 565–575, <https://doi.org/10.1002/pip.3171>.

- [4] Jayakumar Ramanujam, Udai P. Singh, Copper indium gallium selenide based solar cells – a review, *Energy Environ. Sci.* 10 (2017) 1306–1319, <https://doi.org/10.1039/c7ee00826k>.
- [5] Wolfram Witte, Stefanie Spiering, Dimitrios Harikos, Substitution of the CdS buffer layer in CIGS thin-film solar cells, *vip-journal* 26 (2014) 23–27, <https://doi.org/10.1002/vipr.201400546>.
- [6] N. Naghavi, D. Abou-Ras, N. Allsop, N. Barreau, S. Bücheler, A. Ennaoui, C.-H. Fischer, C. Guillen, D. Harikos, J. Herrero, R. Klenk, K. Kushiya, D. Lincot, R. Menner, T. Nakada, C. Platzer-Björkman, S. Spiering, A.N. Tiwari, T. Törndahl, Buffer layers and transparent conducting oxides for chalcopyrite Cu(In,Ga)(S,Se)₂ based thin film photovoltaics: present status and current developments, *Prog. Photovoltaics Res. Appl.* 18 (2010) 411–433, <https://doi.org/10.1002/pip.955>.
- [7] M. Turcu, O. Pakma, U. Rau, Interdependence of absorber composition and recombination mechanism in Cu(In,Ga)(Se,S)₂ heterojunction solar cells, *Appl. Phys. Lett.* 80 (2002) 2598–2600, <https://doi.org/10.1063/1.1467621>.
- [8] A. Chirila, P. Reinhard, F. Pianezzi, P. Bloesch, A.R. Uhl, C. Fella, L. Kranz, D. Keller, C. Gretener, H. Hagendorfer, D. Jaeger, R. Erni, S. Nishiwaki, S. Buecheler, A.N. Tiwari, Potassium-induced surface modification of Cu(In,Ga)Se₂ thin films for high-efficiency solar cells, *Nat. Mater.* 12 (2013) 1107–1111, <https://doi.org/10.1038/NMAT3789>.
- [9] P. Jackson, D. Harikos, E. Lotter, S. Paetel, R. Wuerz, R. Menner, W. Wischmann, M. Powalla, New world record efficiency for Cu(In,Ga)Se₂ thin-film solar cells beyond 20%, *Prog. Photovoltaics Res. Appl.* 19 (2011) 894–897, <https://doi.org/10.1002/pip.1078>.
- [10] I. Repins, M.A. Contreras, B. Egaas, C. DeHart, J. Scharf, C.L. Perkins, B. To, R. Noufi, 19.9%-efficient ZnO/CdS/CuInGaSe₂ solar cell with 81.2% fill factor, *Prog. Photovoltaics Res. Appl.* 16 (2008) 235–239, <https://doi.org/10.1002/pip.822>.
- [11] Nicolae Spalatu, Jaan Hiie, Reelika Kaupmees, Olga Volobujeva, Juri Krustok, Ilona Oja Acik, Malle Krunk, Postdeposition processing of SnS thin films and solar cells: prospective strategy to obtain large, sintered, and doped SnS grains by recrystallization in the presence of a metal halide flux, *ACS Appl. Mater. Interfaces* 11 (2019) 17539–17554, <https://doi.org/10.1021/acsaami.9b03213>.
- [12] M. Nakamura, K. Yamaguchi, Y. Kimoto, Y. Yasaki, T. Kato, H. Sugimoto, Cd-free Cu(In,Ga)(Se,S)₂ thin-film solar cell with record efficiency of 23.35%, *IEEE, J. Photovoltaics* 9 (2019) 1863–1867, <https://doi.org/10.1109/JPHOTOV.2019.2937218>.
- [13] Solar Frontier Achieves World Record Thin-Film Solar Cell Efficiency of 23.35%, 2019, http://www.solar-frontier.com/eng/news/2019/0117_press.html. (Accessed 20 October 2019). accessed.
- [14] D. Harikos, S. Spiering, Powalla, Buffer layers in Cu(In,Ga)Se₂ solar cells and modules, *Thin Solid Films* 480–481 (2005) 99–109, <https://doi.org/10.1016/j.tsf.2004.11.118>.
- [15] N. Barreau, A. Mokrani, F. Couzinié-Devy, J. Kessler, Bandgap properties of the indium sulfide thin-films grown by co-evaporation, *Thin Solid Films* 517 (2009) 2316–2319, <https://doi.org/10.1016/j.tsf.2008.11.001>.
- [16] A. Politano, D. Campi, M. Cattelano, I. Ben Amara, S. Jaziri, A. Mazzotti, A. Barinov, B. Gürbulak, S. Duman, S. Agnoli, L.S. Caputi, G. Granozzi, A. Cupolillo, Indium selenide: an insight into electronic band structure and surface excitations, *Scientific Report. Nature*. 7 (2017) 3445, <https://doi.org/10.1038/s41598-017-03186-x>.
- [17] Takayuki Negami, Taikan Aoyagi, Takuya Satoh, Shin-ichi Shimakawa, Shigeo Hayashi, Yasuhiro Hashimoto, Cd free CIGS solar cells fabricated by dry processes, *IEEE* (2002) 656–659, <https://ieeexplore.ieee.org/stamp/stamp.jsp?tp=&number=1196650>.
- [18] Y.M. Guo, L.P. Zhu, J. Jiang, Y.G. Li, L. Hu, H.B. Xu, Z.Z. Ye, Highly conducting and wide-band transparent F-doped Zn_{1-x}Mg_xO thin films for optoelectronic applications, *J. Alloys Compd.* 602 (2014) 294–299, <https://doi.org/10.1016/j.jallcom.2014.02.181>.
- [19] Katsumi Kushiya, N.I.I. Tetsuro, Ichiro Sugiyama, Yasuhiko Sato, Yoshitugu Inamori, Hiroshi Takeshita, Application of Zn-compound buffer layer for polycrystalline CuInSe₂-based thin film solar cells, *Jpn. J. Appl. Phys.* 35 (1996) 4383–4388, <https://iopscience.iop.org/article/10.1143/JJAP.35.4383/pdf>.
- [20] Susanne Siebentritt, Alternative buffers for chalcopyrite solar cells, *Sol. Energy* 77 (2004) 767–775, <https://doi.org/10.1016/j.solener.2004.06.018>.
- [21] Svetlana Polivtseva, Nicolae Spalatu, Akram Abdalla, Olga Volobujeva, Jaan Hiie, Sergei Bereznev, Pulsed laser deposition of Zn(O,Se) layers for optoelectronic application, *ACS Appl. Energy Mater.* 1 (2018) 6505–6512, <https://doi.org/10.1021/acsaem.8b01431>.
- [22] R. Klenk, Characterisation and modelling of chalcopyrite solar cells, *Thin Solid Films* 387 (2001) 135–140, [https://doi.org/10.1016/S0040-6090\(00\)01736-3](https://doi.org/10.1016/S0040-6090(00)01736-3).
- [23] K. Timmo, M. Kauk-Kuusik, M. Pilvet, M. Altoasar, M. Grossberg, M. Danilson, R. Kaupmees, V. Mikli, J. Raudoja, T. Varema, Cu(In,Ga)Se₂ monograin powders with different Ga content for solar cells, *Sol. Energy* 176 (2018) 648–655, <https://doi.org/10.1016/j.solener.2018.10.078>.
- [24] J. Tauc, R. Grigorovic, A. Vancu, Optical properties and electronic structure of amorphous germanium, *phys. stat. sol.* 15 (1966) 627, <https://doi.org/10.1002/pssb.19660150224>.
- [25] J. Tauc, Optical properties and electronic structure of amorphous Ge and Si, *Mater. Res. Bull.* 3 (1968) 37–46, [https://doi.org/10.1016/0025-5408\(68\)90023-8](https://doi.org/10.1016/0025-5408(68)90023-8).
- [26] V. Mikli, J. Hiie, V. Valdna, M. Viljus, R. Traksmaa, Kallavus, Formation of structure of the CdTe film, recrystallized on Mo/glass substrate under high temperature and mechanical pressure, *Thin Solid Films* 517 (2009) 2252–2255, <https://doi.org/10.1016/j.tsf.2008.10.102>.
- [27] Mati Danilson, Temperature Dependent Electrical Properties of Kesterite Monograin Layer Solar Cells, PhD thesis, TalTech, 2016, <https://digikogu.taltech.ee/et/Item/a294dce1-9731-40f8-8048-195234e956d5>.
- [28] Xianwu Xiu, Zhiyong Pang, Maoshui Lv, Ying Dai, Lina Ye, Shenghao Han, Transparent conducting molybdenum-doped zinc oxide films deposited by RF magnetron sputtering, *Appl. Surf. Sci.* 253 (2007) 3345–3348, <https://doi.org/10.1016/j.apsusc.2006.07.024>.
- [29] N. Khedmi, M. Ben Rabea, M. Kanzari, Thickness dependent structural and optical properties of vacuum evaporated CuInS₃ thin films, *Energy Procedia* 44 (2014) 61–68, <https://doi.org/10.1016/j.egypro.2013.12.010>.
- [30] M.G. Varnamkhandi, H.R. Fallah, M. Mostajaboddavati, A. Hassanzadeh, Influence of Ag thickness on electrical, optical and structural properties of nanocrystalline MoO₃/Ag/ITO multilayer for optoelectronic applications, *Vacuum* 86 (2012) 1318–1322, <https://doi.org/10.1016/j.vacuum.2011.12.002>.
- [31] Geoff Martin, Mottola Al, Intensified CCDs Investigate Oplasma Plumes, 2000, <https://www.laserfocusworld.com/detectors-imaging/article/16555580/intensified-ccd-investigate-oplasma-plumes>. (Accessed 24 November 2020). accessed.
- [32] Helena Wilhelm, Hans-Werner Schock, Scheer Roland, Interface recombination in heterojunction solar cells: influence of buffer layer thickness, *J. Appl. Phys.* 109 (2011), 084514, <https://doi.org/10.1063/1.3554409>.
- [33] Chang-Soo Lee, Suncheul Kim, Young-Min Shin, Byung Guk Park, Byung Tae Ahn, HyukSang Kwon, Performance improvement in Cd-free Cu(In,Ga)Se₂ solar cells by modifying the electronic structure of the ZnMgO buffer layer, *RSC Adv.* 4 (2014) 36784, <https://doi.org/10.1039/c4ra07776h>.
- [34] M. Turcu, U. Rau, Fermi level pinning at CdS/Cu(In,Ga)(Se,S)₂ interfaces: effect of chalcopyrite alloy composition, *J. Phys. Chem. Solid.* 64 (2003) 1591–1595, [https://doi.org/10.1016/S0022-3697\(03\)00137-9](https://doi.org/10.1016/S0022-3697(03)00137-9).
- [35] J. Lindahl, J.T. Wätjen, A. Hultqvist, T. Ericson, M. Edoff, T. Törndahl, The effect of Zn_{1-x}Sn_xO_y buffer layer thickness in 18.0% efficient Cd-free Cu(In,Ga)Se₂ solar cells, *Prog. Photovoltaics Res. Appl.* 21 (2013) 1588–1597, <https://doi.org/10.1002/pip.2239>.
- [36] M. Nardone, V.G. Karpov, D. Shvydka, M.L.C. Attygale, Theory of electronic transport in noncrystalline junctions, *J. Appl. Phys.* 106 (2009), 074503, <https://doi.org/10.1063/1.3213336>.
- [37] Steven S. Hegedus, William N. Shafarman, Thin-film solar cells: device measurements and analysis, *Prog. Photovoltaics Res. Appl.* 12 (2004) 155–176, <https://doi.org/10.1002/pip.518>.
- [38] Christiana Honsberg, Stuart Bowden, Quantum efficiency. PVEducation, <https://www.pveducation.org/pvcdrom/solar-cell-operation/quantum-efficiency>. (Accessed 14 March 2021). accessed.
- [39] J. Kessler, K.O. Velthaus, M. Ruckh, R. Laichinger, H. Schock, D. Lincot, R. Ortega, J. Vedel, Chemical bath deposition of CdS on CuInSe₂, etching effects and growth kinetics, in: *Proceedings of the 6th International Photovoltaic Science and Engineering Conference*, New Delhi, Feb, 1992, pp. 1005–1010.
- [40] D. Lincot, et al., Chemical bath deposition of CdS on CuInSe₂: combining dry and wet processes for high efficiency thin film solar cells. *Proceedings of the 11th European Photovoltaics Solar Energy Conference*, Montreux, 1992, pp. 870–873.

Appendix 2

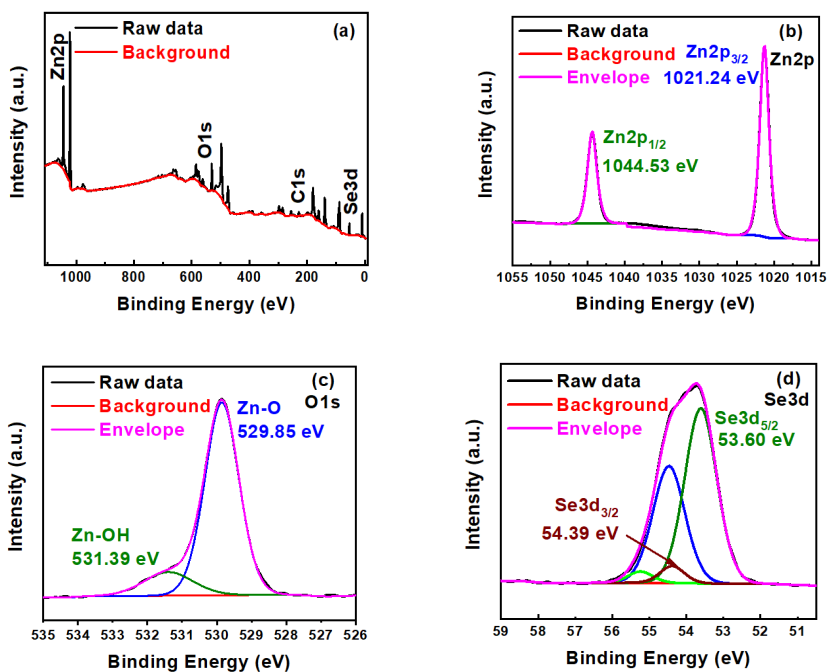


Figure S.1. XPS spectra of Zn(O,Se) layers deposited onto SLG substrate at 550°C (a) wide survey, (b) Zn 2p, (c) O 1s, and (d) Se 3d.

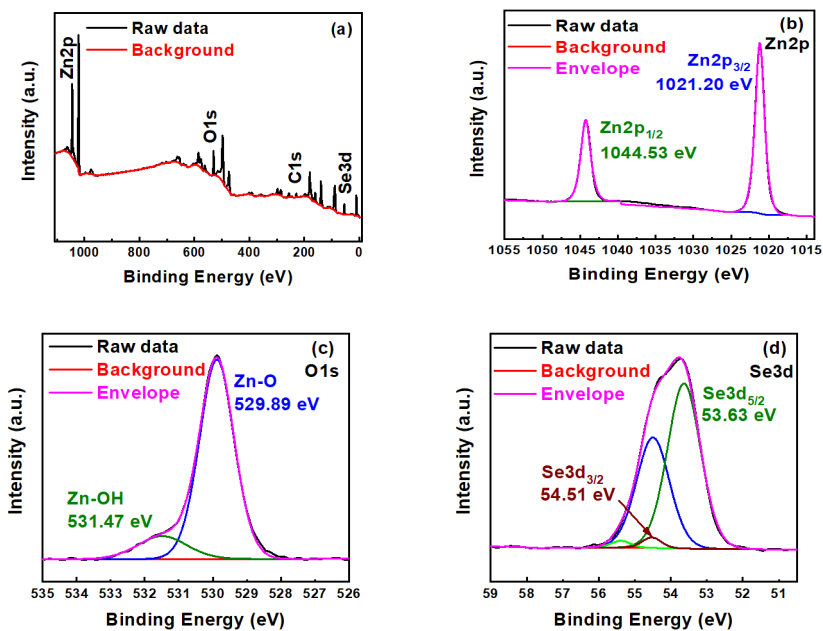


Figure S.2. XPS spectra of Zn(O,Se) layers deposited onto SLG substrate at 600°C (a) wide survey, (b) Zn 2p, (c) O 1s, and (d) Se 3d.

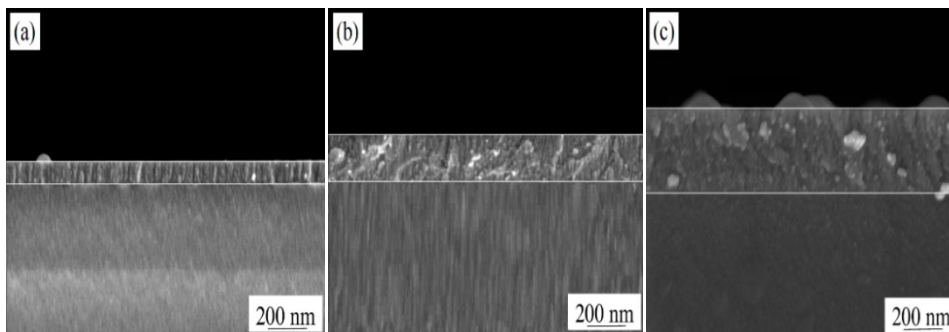


Figure S.3. HR-SEM cross-section images of Zn(O,Se) buffer layers deposited at RT with different thickness of (a) 100, (b) 200 nm and (c) 300 nm.

Curriculum vitae

Personal data

Name: Akram Abdalla Mohammed Ibrahim
Date of birth: 03.07.1986
Place of birth: Kerma, Sudan
Citizenship: Sudanese

Contact data

E-mail: akrami.abdalla@gmail.com

Education

2017–2021 Tallinn University of Technology, PhD in Chemical and Materials Technology
2013–2016 King Fahd University of Petroleum and Minerals, Master of Science (Chemistry)
2006–2010 Sudan University of Science and Technology, Bachelor of Science (Chemistry)
2002–2005 Dongola Secondary school

Language competence

Nubian Native
Arabic Native
English Advanced
Estonian Beginner

Professional employment

2017–2021 Early Stage Researcher, Tallinn University of Technology, Estonia
2015–2016 Research Assistant at Center for Environment and water, King Fahd University of Petroleum and Minerals, Saudi Arabia
2014–2015 Administrative Assistant at Chemistry Department, King Fahd University of Petroleum and Minerals, Saudi Arabia
2013–2013 Teaching Assistant at Chemistry Department, Sudan University of Science and Technology, Sudan

Conferences

2018–2020 Graduate school of functional materials and technologies (GSFMT) scientific conference, Tallinn/Tartu, Estonia
2019 European Materials Research Society, Spring meeting 2019, Nice, France
2019 Modern Materials and Manufacturing 2019, Tallinn, Estonia

Projects

09.2019–11.2021 TAR16016 (TK141) Advanced materials and high–technology devices for sustainable energetics
11.2017–12.2020 PUT1495 SnS and SnSe thin films for Photovoltaic Application
11.2017–12.2019 IUT19-28 New materials and technologies for solar energetics
11.2017–12.2018 B54 SnS thin films for solar cells

Supervised dissertations

Anouar Bouchaara, Master's Degree, 2020, (sup) Dr. Sergei Bereznev, **Akram Abdalla**. Study of thickness effect on properties of Zn(O,S) layers prepared by pulsed laser deposition. Department of Materials and Environmental Technology, School of Engineering, Tallinn University of Technology

List of publications

1. **Akram Abdalla**, Mati Danilson, Souhaib Oueslati Maris Pilvet, Sergei Bereznev. Amorphous Zn(O,Se) buffer layer for Cu(In,Ga)Se₂ thin film solar cells. *Materials Science in Semiconductor Processing*. 132 (2021) 105862. DOI: 10.1016/j.mssp.2021.105862.
2. **Akram Abdalla**, Erki Kärber, Valdek Mikli, Sergei Bereznev. The effect of laser fluences on the structural and optoelectronic properties of Zn(O,Se) films. *Materials Science in Semiconductor Processing*. 121 (2021) 105429. DOI: 10.1016/j.mssp.2020.105429.
3. **Akram Abdalla**, Ibrahim Khan, Manzar Sohail, Ahsanulhaq Quarshi. Au/Ga₂O₃/ZnO heterostructure nanorods arrays for effective photoelectrochemical water splitting. *Solar Energy*, 181 (2019) 333–338. DOI: 10.1016/j.solener.2019.01.065.
4. **Akram Abdalla**, Sergei Bereznev, Nicolae Spalatu, Olga Volobujeva, Natalja Sleptsuk, Mati Danilson. Pulsed laser deposition of Zn(O,Se) layers in nitrogen background pressure. *Scientific Reports*. 17443 (2019) 1–10. DOI: 10.1038/s41598-019-54008-1.
5. Svetlana Polivtseva, Nicolae Spalatu, **Akram Abdalla**, Olga Volobujeva, Jaan Hiie, Sergei Bereznev. Pulsed laser deposition of Zn(O,Se) layers for optoelectronic application. *ACS Applied Energy Materials*. 1 (2018) 6505–6512. DOI: 10.1021/acsaem.8b01431.
6. Ibrahim Khan, **Akram Abdalla**, Manzar Sohail, Ahsanulhaq Qurashi. Sonochemical assisted synthesis of RGO/ZnO nanowire arrays for photoelectrochemical water splitting. *Ultrasonics Sonochemistry*. 37 (2017) 669–675. DOI: 10.1016/j.ultsonch.2017.02.029.
7. **Akram Ibrahim**, Ibrahim Khan, Naseer Iqbal, Ahsanulhaq Qurashi. Facile synthesis of tungsten oxide–Bismuth vanadate nanoflakes as photoanode material for solar water splitting. *International Journal of Hydrogen Energy*. 42 (2017) 3423–3430. DOI: 10.1016/j.ijhydene.2016.09.095.
8. Ibrahim Khan, **Akram Abdalla**, Ahsanulhaq Qurashi. (2017). Synthesis of hierarchical WO₃ and Bi₂O₃/WO₃ nanocomposite for solar-driven water splitting applications. *International Journal of Hydrogen Energy*, 42 (2017) 3431–3439. DOI: 10.1016/j.ijhydene.2016.11.105.

Elulookirjeldus

Isikuandmed

Nimi: Akram Abdalla Mohammed Ibrahim
Sünniaeg: 03.07.1986
Sünnikoht: Kerma, Sudaan
Kodakondsus: Sudaan

Kontaktandmed

E-post: akrami.abdalla@gmail.com

Hariduskäik

2017–2021 Tallinna Tehnikaülikool, PhD Keemia-ja Materjalitehnoloogia
2013–2016 King Fahdi Nafta-ja Mineraalide Ülikool, MSc (Keemia)
2006–2010 Sudaan Teaduse ja Tehnoloogia Ülikool, BSc (Keemia)
2002–2005 Dongola Keskkool

Keelteoskus

Nubian Emakeel
Araabia Emakeel
Inglise Kõrgtase
Eesti keel Algtase

Teenistuskäik

2017–2021 doktorant-nooremteadur, Inseneriteaduskond, Materjali- ja keskkonnatehnoloogia instituut, Tallinna Tehnikaülikool
2015–2016 Keskkonna- ja veekeskuse teadusassistent, King Fahdi Nafta- ja Mineraalide Ülikool, Saudi Araabia
2014–2015 Keemiaosakonna Haldusassistent, King Fahdi Nafta- ja Mineraalide Ülikool, Saudi Araabia
2013–2013 Keemiaosakonna õppejõud, Sudaan Teaduse ja Tehnoloogia Ülikool, Sudaan

Konverentsid

2018–2020 Funktsionaalsete materjalide ja tehnoloogiate kõrgkooli teaduskonverents, Tallinn/Tartu, EESTI
2019 Euroopa Materjaliuuringute Selts, kevadine koosolek 2019, Nice, Prantsusmaa
2019 Kaasaegsed materjalid ja tootmine 2019, Tallinn, EESTI

Projektid

09.2019–11.2021 TAR16016 (TK141) Uudsed materjalid ja kõrgtehnoloogilised seadmed energia salvestamise ja muundamise süsteemidele
11.2017–12.2020 PUT1495 SnS ja SnSe õhuked kiled päikeseenergeetikale
11.2017–12.2019 IUT19-28 Uued materjalid ja tehnoloogiad päikeseenergeetikale
11.2017–12.2018 B54 SnS thin films for solar cells

Juhendatud väitekirjad

Anouar Bouchaara, Magistrikraad, 2020, (juhendajad) Dr. Sergei Bereznev, **Akram Abdalla**. Paksuse Mõju Uurimine Impulslaser-Sadestus Meetodil Valmistatud Zn(O,S) Kihtide Omadustele, Inseneriteaduskond, Materjali- ja keskkonnatehnoloogia instituut, Tallinna Tehnikaülikool

Publikatsioonid

1. **Akram Abdalla**, Mati Danilson, Souhaib Oueslati Maris Pilvet, Sergei Bereznev. Amorphous Zn(O,Se) buffer layer for Cu(In,Ga)Se₂ thin film solar cells. *Materials Science in Semiconductor Processing*. 132 (2021) 105862. DOI: 10.1016/j.mssp.2021.105862.
2. **Akram Abdalla**, Erki Kärber, Valdek Mikli, Sergei Bereznev. The effect of laser fluences on the structural and optoelectronic properties of Zn(O,Se) films. *Materials Science in Semiconductor Processing*. 121 (2021) 105429. DOI: 10.1016/j.mssp.2020.105429.
3. **Akram Abdalla**, Ibrahim Khan, Manzar Sohail, Ahsanulhaq Quarshi. Au/Ga₂O₃/ZnO heterostructure nanorods arrays for effective photoelectrochemical water splitting. *Solar Energy*, 181 (2019) 333–338. DOI: 10.1016/j.solener.2019.01.065.
4. **Akram Abdalla**, Sergei Bereznev, Nicolae Spalatu, Olga Volobujeva, Natalja Sleptsuk, Mati Danilson. Pulsed laser deposition of Zn(O,Se) layers in nitrogen background pressure. *Scientific Reports*. 17443 (2019) 1–10. DOI: 10.1038/s41598-019-54008-1.
5. Svetlana Polivtseva, Nicolae Spalatu, **Akram Abdalla**, Olga Volobujeva, Jaan Hiie, Sergei Bereznev. Pulsed laser deposition of Zn(O,Se) layers for optoelectronic application. *ACS Applied Energy Materials*. 1 (2018) 6505–6512. DOI: 10.1021/acsaem.8b01431.
6. Ibrahim Khan, **Akram Abdalla**, Manzar Sohail, Ahsanulhaq Qurashi. Sonochemical assisted synthesis of RGO/ZnO nanowire arrays for photoelectrochemical water splitting. *Ultrasonics Sonochemistry*. 37 (2017) 669–675. DOI: 10.1016/j.ultsonch.2017.02.029.
7. **Akram Ibrahim**, Ibrahim Khan, Naseer Iqbal, Ahsanulhaq Qurashi. Facile synthesis of tungsten oxide–Bismuth vanadate nanoflakes as photoanode material for solar water splitting. *International Journal of Hydrogen Energy*. 42 (2017) 3423–3430. DOI: 10.1016/j.ijhydene.2016.09.095.
8. Ibrahim Khan, **Akram Abdalla**, Ahsanulhaq Qurashi. (2017). Synthesis of hierarchical WO₃ and Bi₂O₃/WO₃ nanocomposite for solar-driven water splitting applications. *International Journal of Hydrogen Energy*, 42 (2017) 3431–3439. DOI: 10.1016/j.ijhydene.2016.11.105.

ISSN 2585-6901 (PDF)
ISBN 978-9949-83-760-1 (PDF)